DETERMINATION OF THE HEAD LOSS COEFFICIENT OF CLOSELY SPACED PIPE BENDS

by

THOKOZANI JUSTIN KUNENE

Thesis submitted in fulfilment of the requirements for the degree

Master Technology: Mechanical Engineering

in the Faculty of Engineering

at the Cape Peninsula University of Technology

Supervisor: Professor Greame Oliver

Co-supervisor: Professor Jasper Steyn

Bellville

May 2017

DECLARATION

I, Thokozani Justin Kunene, declare that the contents of this dissertation/thesis represent my own unaided work, and that the dissertation/thesis has not previously been submitted for academic examination towards any qualification. Furthermore, it represents my own opinions and not necessarily those of the Cape Peninsula University of Technology.

Signed **Date**

ABSTRACT

Space limitation in ships and the complex pipe layouts in chemical, mineral and food processing plants lead to the employment of closely spaced bends. The limited information regarding the head loss coefficient of pipe bends orientated as bend-spacer-bend has led pipeline designers to treat them as isolated bends with the same loss coefficient. Thus, to calculate the head loss in the piping system would simply involve summing the head loss coefficient of bends and neglecting their configuration. This practice causes inaccurate computation of head losses in the system.

In this study a computational model is developed for the head loss coefficient of closely spaced pipe bends. This is then supported by experimental verification. A more accurate but still simple and easy to use empirical correlation is derived. The empirical correlation is established and the data presented under isothermal conditions for turbulent flows in a range $7.3x10^4 \leq Re \leq 5.8x10^5$ and a spacing ratio of $1D \leq L/d \leq 10D$and curvature ratio of $3 \leq r_c/d \leq 5$. Using ANSYS® CFX® 11, a commercial computational fluid dynamics (CFD) package, the fluid domain representing two 90^0 smooth pipe bends separated by a short pipe was solved and the mechanisms causing the head loss coefficient were explored by using the CFD results to visualise the fluid flow structure/pattern. The computational model was validated by comparing the head loss coefficient of a single bend and the model was found to be sound. The experiments conducted in the built test facility using smooth pipes showed similarities in the trends between the CFD work and the published data and they were to be found have a similar trend. The experiment had shown results that agree to the findings from literature.

ACKNOWLEDGEMENTS

I wish to thank:

God Almighty for enable me to reach this point in my life and career.

- My supervisors for not only believing in my ability but enhancing it and introducing me to the world of research.
- My family for their support in all forms.
- Colleagues, peer reviewers and Cape Peninsular University of Technology & University of Pretoria's mechanical workshop technicians and all of you.
- Mr Mark Kilfoil, Prof. V. Fester, Dr. F. Iudicello and Dr D. Philpott from EDSU
- Prof. J. Steyn from Automotive Industry Development Centre & University of Pretoria

The financial assistance of the National Research Foundation towards this research is acknowledged. Opinions expressed in this thesis and the conclusions arrived at, are those of the author, and are not necessarily to be attributed to the National Research Foundation.

DEDICATION

This is for you

- Fusi Priscilla Nkomo, late grandma: *The pillar!*
- Bongani “Shaba” Shabangu, late friend: *It is about engineering baba!*
- Bongani “TaMxi” Mxi, late friend: *We wanted to be in the same graduation ceremony*
- Boitumelo “iNkunzi emnyama” Telekoa , late friend: *hey ma!*

“Abraham Flexner firmly believed that men could shape their own affairs, direct their lives toward a desirable future, and that research and education were major instruments of that endeavor.”, Harry Woolf, Director-Community Of Scholars, The Institute of Advanced study.

TABLE OF CONTENTS

LIST OF FIGURES

LIST OF TABLES

LIST OF SYMBOLS

A	Area (m^2)
a	Constant
CW	Colebrook-White
C_{1-2}	Correction factor for closely spaced pipe bends
d, D	Inside diameter of the pipe (m)
Exp	Experiment
f	Friction factor
f'	Empirical friction factor
g	gravitational acceleration (m/s^2)
K	Head loss coefficient
k*	Head loss coefficient of closely spaced pipe bends
k'	Empirical head loss coefficient for smooth pipes
L	Length of the pipe (m)
m_w	Mass of the water (kg)
P	Pressure (Pa)
P_2	Pressure drop due to skin friction (Pa)

P_3 Pressure drop due to wake friction (Pa)

Q Volumetric flow rate (m^3/s)

R Radius of pipe (m)

r_c Radius of curvature (m)

Re Reynolds number, Re $=\rho Dv/\mu$

r_w Distance to the nearest to the wall (m)

u Average axial velocity (m/s)

u_f Friction velocity, $u_f = \sqrt{\frac{\tau_w}{\rho}}$

v Average radial velocity (m/s)

V Mean velocity (m/s)

w Average tangential velocity (m/s)

y^+ Dimensionless wall distance, $y^+ = \frac{u_f r_w}{\nu}$

Greek letters

θ Angle of a bend (^{0})

γ Orientation angle of the bends (^{0})

Δ Variable difference

ε Roughness of a pipe (mm)

Φ Scalar variables

ν Kinetic viscosity (Pa.s), ρ/μ

μ Dynamic viscosity (Pa.s)

ρ Density (kg/m^3)

τ_w Wall shear stress, $\mu\left(\frac{\partial u}{\partial r_w}\right)_{r_w=0}$

Subscripts

1-2 First and second bend

c Curvature

d Downstream the bends

in inlet

local Local velocity

out Outlet

s Spacer

tot Total pressure drop

u Upstream of the bends

W	Water
x, y, z	Orthogonal coordinates

ABBREVIATIONS

CFD	computational fluid dynamics
N-S	Navier-Stokes
RANS	Reynolds-Averaged Navier-Stokes
RNG	Re-Normalisation Group
SST	Shear Stress Transport

CHAPTER 1

INTRODUCTION TO THE RESEARCH TOPIC

This chapter briefly introduces the research topic. It outlines the need for the research, the aims and the methodology that will be followed.

1.1 Background

Space limitations in ships and the complex pipe layouts in chemical, mineral and food processing plants lead to the use of pipe bends that are closely spaced (Papworth & Miller, 1974:27) and (Ito 1987:548). The limited information with regard to the head loss coefficient of pipe bends arranged as bend-spacer-bend, (see Fig. 1.1), has led pipeline designers to treat pipe bends configured in such a manner as isolated bends. Thus, calculating the head loss in the piping system would simply involve summing the head loss coefficient of bends and neglecting their configuration (Daugherty, 1977:228). This practice may cause errors in the calculation of the head losses in the system. Therefore, it is essential to have enough information for the design and performance prediction of equipment in pipe and duct systems. The efficiency of industrial plants depends on the accurate prediction of internal flows (Flowmaster, 2010:1).

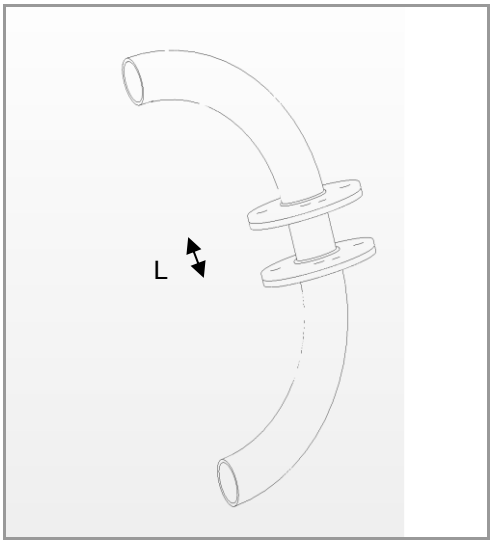

Figure 1.1: Configuration of two closely spaced bends in the same plane

For a piping system, costs are both capital and running. Designs that do not take into account features that cause energy loss adequately result in high expenditures. Reliable design data for the prediction of friction losses in isolated bends is readily available. Although closely spaced bends find many applications there is minimal published design data on closely spaced bends. Hence it is important to investigate and publish such information.

Experimental work and numerical computations were used in the investigation. The pressure difference between the upstream and downstream sides of the pipe bends was determined by using computational fluid dynamics (CFD). Experiments were conducted using a custom built test apparatus to record pressure and flow rate outputs for comparison with the CFD results.

1.2 Statement of research problem

The flow characteristics in a single pipe bend for Newtonian fluids are well understood and have been investigated in many experiments and numerical simulations. The resulting data for the prediction of friction losses and the calculation of a loss coefficient in a single pipe bend is well established and reliable. However, despite being common in many applications, there is relatively little data for closely spaced pipe bends. Therefore, the research problem is: What is the relationship between head loss coefficient and the geometry of a pair of closely spaced bends?

1.3 Research objectives

The aim of this research is to establish an empirical correlation (or correlations) for the head loss coefficient of closely spaced 90^0 bends by taking into account the curvature ratios, flow regimes and the spacing ratio. In order to achieve this, the following objectives were meet, i.e.

- To develop a CFD model to calculate pressure values and loss coefficients for closely spaced pipe bends.
- To obtain pressure losses experimentally and compute the head loss coefficients of closely spaced pipe bends to check the validity of the CFD model.
- To derive a correlation for smooth pipe bends using the CFD model.

1.4 Scope

The research was limited to incompressible, single-phase Newtonian fluids flowing through two 90^0 pipe bends. The investigation covered the following ranges:

- Curvature ratios of centre line radius (r_c) to inside diameter of the pipe (d), r_c/d = 3, 4 & 5.
- Newtonian fluid (water).
- Turbulent flow, $7.3x10^4 \leq Re \leq 5.8x10^5$.
- Length of the straight pipe between the bends from 1d to 10d (spacing ratio (L/d) from 1 to 10).
- Two 90^0 bends in the same plane separated by a short straight pipe.

1.5 Methodology

CFD was performed over the full scale of parameter values listed above. The experiments to verify the CFD results were conducted at a curvature ratio of r_c/d = 3, three Reynolds numbers ($7.3x10^4$, $3.2x10^5$ & $5.8x10^5$) and three spacer lengths (0d, 5d & 10d). The numerical data was gathered was of pressure and velocity profiles of the flow upstream and downstream of the bends, as well as in the spacer between bends. The data for the head loss coefficient was combined to form an empirical correlation. The methods used to conduct this study were as indicated below.

1.5.1 Computational Modelling

The ANSYS® CFX® 11 computational fluid software uses finite volume techniques to solve a wide range of turbulence models that model fluid flow in any domain. It provides a quantitative and qualitative approach to enable analyses on solved fluid flow scenarios. Amongst the turbulence models that were available from the software, the Shear Stress Transport Model (SST) was used for this study because it is robust, and it accurately implements the flow in the near-wall region (the viscous sub-layers in the boundary layer are modelled accurately). The SST model excels with flow separation prediction as opposed to the k-ε model, ANSYS (2006:2). Even though the k-ε model is robust, economical and generally an accepted turbulence model, it under predicts separation which results in an optimistic prediction of pressure drop for curvatures.

1.5.2 Experimental Investigation

The test rig that was used for experiments was set up in a mechanical engineering fluids laboratory. Pressure readings were obtained from transducers upstream and downstream of the test bends. Flow rate was obtained from an ultrasonic flowmeter. The test section was comprised of two 90^0 pipe bends separated by a short straight pipe. The pressure drop across the test section was used to compute the value of the head loss coefficient.

The experiments conducted for this study were as follows:

- For each straight length and curvature, readings of pressure at three flow rates (Reynolds numbers) were taken.
- The flow rate was varied using a gate valve.

Readings on a curvature ratio ($r_c/d = 3$) with each spacer ratio (L/d = 0, 5 & 10) were taken at each Reynolds number ($7.3x10^4$, $3.2x10^5$ & $5.8x10^5$).

1.5.3 Data analysis methods

Flow behaviour was studied through CFD visualisation and the graphics that depict pressure distribution inside the bends and the spacer. Calculations were carried out to derive an empirical formula that can be used to compute a loss coefficient of closely spaced pipe bends. The formula was derived using multiple linear regression models through a stepwise procedure: The logarithmic of the dimensionless groups were transformed and the data from the groups was transferred to the statistical packages to determine the coefficients of the power functions. The correlation for the friction factor was calculated using the statistical analysis program StataQuest while the Microsoft Excel Data Analysis package (applying multi-linear regression) was used for the head loss coefficient.

1.6 Importance and benefits

The importance of this study arises from the need to more accurately calculate the pressure drop in the system to find a suitable device (e.g. a pump) to overcome the friction. The study provides loss coefficient data for closely spaced bends determined by CFD analysis and verified by experiment as well flow visualisation from ANSYS® CFX® 11. From the CFD analysis correlations for predicting

the head loss coefficient of closely spaced pipe bends were calculated. Neglecting the effects of close spacing can result in selection of the wrong size of pump or fan.

CHAPTER 2

THEORY

2.1 Introduction

This chapter deals with the theoretical aspects of CFD that includes theories of the Navier-Stokes (N-S) and the Reynolds-Average Navier-Stokes (RANS) equations. These are equations that describe the flow of any fluid. The boundary layer theorem is also illustrated and is essential in providing understanding on the viscous resistance of fluids. The subject was approached from the perspective of certain geometrical effects that cause flow separation. This chapter also provides a theoretical analysis of the head loss coefficient, i.e. for single and closely spaced bends, and of the experimental methods of determining the head loss coefficient.

2.2 Navier-Stokes equations

The N-S equations describe the motion of a fluid in three dimensions. The equations are used to represent the motion of an incompressible fluid. As the relevant flow domain is turbulent flow, a turbulence model was used (see sections 2.3 and 2.4) (Sekavčnik *et al*, 2006:139).

Generally, the N-S equations are presented in mathematical statements that describe the laws of physics, applicable to fluid flow. The N-S equations are non-linear partial differential equations that often display different mathematical forms that are parabolic, hyperbolic or elliptic and sometimes a combination of them (Iudecello, 2008:44). Hence, they are complicated to solve analytically even for very a simple configuration (solving friction flow through a straight pipe) and require numerical solutions (Tryggeson, (2007:1).

2.2.1 Governing equations of fluid dynamics

The Navier-Stokes equations for compressible viscous flow can be presented as follows (Anon, 2008:8), (Iudecello, 2008:33) and (Tryggeson, 2007:4-5):

Continuity equation:

$$\frac{\partial \rho}{\partial t} + div(\rho u) = 0 \qquad \textbf{2.1}$$

Momentum equations:

x component: $$\frac{\partial(\rho u)}{\partial t} + div(\rho u \mathbf{V}) = -\frac{\partial p}{\partial x} + div(\mu\ grad\ u) + S_{Mx}$$

y component: $$\frac{\partial(\rho v)}{\partial t} + div(\rho v \mathbf{V}) = -\frac{\partial p}{\partial y} + div(\mu\ grad\ v) + S_{My}$$

z component: $$\frac{\partial(\rho w)}{\partial t} + div(\rho w \mathbf{V}) = -\frac{\partial p}{\partial z} + div(\mu\ grad\ w) + S_{Mz}$$

2.2

Where:

ρ = fluid density

$U(u, v, w)$ = fluid velocity

p = pressure experienced by a fluid

μ = dynamic viscosity

$S_{Mx} = S_{My} = S_{Mz} = \rho g$ = body forces to gravity

The above equations are four transport equations with five unknowns. In order to balance the equations, one algebraic equation (Eq. 2.3) that relates density to pressure must be added

$$\rho = \rho(p) \qquad \textbf{2.3}$$

If the viscosity of a Newtonian fluid does not change and flow is incompressible, the N-S equations can be simplified. The continuity equation is:

$$\nabla . u = 0 \qquad \textbf{2.4}$$

The momentum equations become:

x component: $$\frac{\partial u}{\partial t} + div(u \mathbf{V}) = -\frac{1}{\rho}\frac{\partial p}{\partial x} + \upsilon \nabla^2 \mathbf{V} + S_{Mx} \qquad \textbf{2.5a}$$

y component: $$\frac{\partial v}{\partial t} + div(v\mathbf{V}) = -\frac{1}{\rho}\frac{\partial p}{\partial y} + \upsilon\nabla^2\mathbf{V} + S_{My}$$ **2.5b**

z component: $$\frac{\partial w}{\partial t} + div(w\mathbf{V}) = -\frac{1}{\rho}\frac{\partial p}{\partial z} + \upsilon\nabla^2\mathbf{V} + S_{Mz}$$ **2.5c**

Where:

$\upsilon = \frac{\mu}{\rho}$ = kinematic viscosity

These transport equations can be expressed in a general form. In this manner any scalar variable, i.e., pressure, force, velocity, etc, can be incorporated and investigated.

$$\frac{\partial(\rho\phi)}{\partial t} + div(\rho\phi\mathbf{V}) = div(\Gamma grad\phi) + S_\phi$$ **2.6**

Where:

ϕ = scalar variable

Γ = diffusion coefficient

S_ϕ = source term, can be B_ϕ (Body force), F_ϕ (Distributed resistance) or V_ϕ (other viscous forces) etc.

The terms in Eq. 2.6 represent the rate of change, the convection, the diffusive and the source term.

2.2.2 Reynolds-Averaging Navier-Stokes (RANS) equations

Most of the fluid flow in industrial applications is turbulent (Iudecello, 2008:42). In order to predict from turbulent flow using the N-S equations, the scalar variables must be averaged. The Reynolds averaging method is introduced in the N-S equations in order to account for unsteady disturbances in the form of fluctuating variables, i.e., velocities and pressures which are found in turbulent flows.

Turbulent flows are three-dimensional and time-dependent. They contain fluctuations in their variables that are bounded in terms of frequency, amplitude and space (Anon, 2008:10). The stated

characteristics of a turbulent fluid can be analysed using statistical tools such as an ensemble averaging of time-dependent variables (Cebeci *et al*, 2005:55). The procedure is to replace the instantaneous values in the N-S equations by the sum of their mean and fluctuating parts.

$$u = \bar{u} + u' , v = \bar{v} + v' , \; w = \bar{w} + w' , p = \bar{p} + p' \qquad \textbf{2.7}$$

The combination of the Reynolds-Averaging Navier-Stokes and the turbulence models (the core of CFD) produce Reynolds stresses. The Reynolds stresses (Reynolds stress tensor) appear because of the averaging of the velocities (scalars variables) in the momentum equations in order to address turbulent fluctuations in a fluid. Further explanation is provided in section 2.3 and 2.4:

2.3 Background to computational fluid dynamics

Computational Fluid Dynamics (CFD) as an engineering tool has its origins in the aerospace industry in the 1960s and 1970s. The availability of high-speed computers promoted the development of numerical algorithms. Thus, numerical methods (computer simulation) became an addition to the two conventional approaches of solving fluid dynamics problems, namely theory and experiments (Iudecello, 2008:4). If CFD users do not apply fundamentals of fluid mechanics principles then the CFD tool would be futile. It is important to adhere to the following requirements to obtain most out of a CFD approach: The CFD users must:

- Anticipate flow characteristics, i.e. the physics of flow
- Select an appropriate modelling technology, i.e. turbulence model and boundary conditions.
- Construct an appropriate grid for the domain
- Ensure that the solution is converged in all senses.

CFD, however, still remains subject to validation. Therefore, the results obtained after the CFD modelling and the grid dependence computation must be compared to experimental data (Levchenya *et al,* 2007:1).

CFD solves the Navier-Stokes equations within a given geometry using numerical methods. CFD's numerical solutions are based on discretisized grids of the domain using one of three numerical methods, namely, the Finite Difference Method (FDM), the Finite Element Method (FEM), or the Finite Volume Method (FVD).

Three steps that are followed to solve fluid flow problems. These steps comprise use of the Pre-processor, the Solver and the Post-processor (Iudecello, 2008:5). These processes are described as follows:

2.3.1 Pre-Processor

- The computational domain, which is the geometry or the region of interest (where the fluid flow of interest occurs), is defined.
- A grid is generated.
- The properties of the fluid are defined.
- The boundary conditions are defined.
- The parameters of the numerical solution are specified.

2.3.2 Solver

The solver is used to produce results which contain flow parameters such as the velocity and pressure. It achieves this by using the following numerical techniques:

- Approximation of unknown flow variables by simple functions.
- Discretisation by substitution of the approximations into the governing flow equations.
- Solution of the resulting algebraic equations.

2.3.3 Post-Processor

In the post-processor, the results passed on from the solver are visualised in terms of graphs, plots and animations. It eases understanding of the flow patterns and the associated physical phenomena.

2.4 Introduction to turbulence modelling

Almost all flows of Newtonian fluids are turbulent. Turbulent flow is identified by means of a Reynolds number which is a dimensionless number that is the ratio between inertial forces acting on the fluid and the viscous forces on the fluid. When inertia forces predominate the flow exhibits a turbulent structure. The Reynolds number can be used to classify the flow of a fluid can be

classified as either laminar of turbulent. Turbulent flow will have a Reynolds number of above 4000 and its characteristics include irregularity, diffusivity and dissipation. These characteristics are in the nature of turbulent flows because turbulence is a complex, random state of motion of continual velocity and pressure changes with time (Iudecello, 2008:60). While turbulent flow is three-dimensional, when its equation of motion is averaged, the flow can be treated as two-dimensional (Davidson, 2003:5).

Turbulence can be modelled in CFD. However, some of the length scales in turbulence are much smaller than the size of practical CFD meshes. It is close to impossible presently to model precisely all the important effects in turbulence due to limitations in computational power.

A full description of the available turbulence models is beyond the scope of this study. Instead the general features and limitations of different classes of models will be discussed. These turbulence models have been investigated to the extent to aid in the final choice of the appropriate model in the CFD analysis. Furthermore, in light of the purpose of this research only eddy-viscosity (two-equation) models will be presented. Some models in a branch of the eddy-viscosity are the non-linear eddy-viscosity model and Reynolds-stress transport models.

The equations used in industrial CFD to model flows are based on the Navier-Stokes equations. These equations are time-dependent and describe both laminar and turbulent flows. However, Reynolds-Averaged Navier-Stokes (RANS) models are based on averaging the Navier-Stokes equations in both time and space. In essence, it is more economical on computational effort to simulate RANS than Direct Numerical Simulations (DNS) (Iudecello, 2008:63). The available simulating methods will be discussed further in the following sections of this chapter. A brief explanation of RANS is as follows:

If the time-mean and fluctuations of velocity and pressure E.q 2.7 are substituted into Navier-Stokes equations (2.8), the RANS equations (2.9) are formed.

$$\frac{\partial \rho u_i u_j}{\partial x_j} = -\frac{\partial p}{\partial x_j} + \frac{\partial}{\partial x_j}\left(\mu \frac{\partial u_i}{\partial x_j}\right) \qquad \textbf{2.8}$$

$$\frac{\partial \overline{u_j}}{\partial x_j} = 0$$

$$\frac{\partial \rho \overline{u_i u_j}}{\partial x_j} = -\frac{\partial \overline{p}}{\partial x_j} + \frac{\partial}{\partial x_j}\left(\mu \frac{\partial \overline{u_i}}{\partial x_j}\right) - \frac{\partial \rho\left(\overline{u_i' u_j'}\right)}{\partial x_j} \quad \textbf{2.9}$$

The last term in Eq.2.9 is an additional term in the RANS to indicate the effects of turbulence. It contains the Reynolds stresses. These stresses are difficult to determine directly, but can be modelled by additional closure models (Lasher & Sonnenmeier, 2007:49). Thus, the different methods of solving these stresses result in various types of turbulence models (Iudecello, 2008:64).

Modern turbulence models approximate three-dimensional turbulent flow and employ additional partial differential equations. These equations model turbulence kinetic energy, turbulence dissipation and the six Reynolds stresses.

2.4.1 Eddy viscosity models (EVM)

Prandtl (1945) introduced the concept of the turbulent viscosity to be a function of a turbulent kinetic energy, which led to the development of one-equation models (Sodja, 2007:11). The two-equation model of eddy viscosity which is the Boussinesq assumption followed. The Boussinesq assumption states that the Reynolds stress tensor, the velocity gradients and the eddy viscosity are related (Davidson, 2008:15). The EVM is a source of two-equation models and is one of the *closure problem* equations (Menter, 1994:2). In essence, the EVM assumes the turbulent stress to be proportional to the mean rate of strain. It is derived from the turbulent transport equation as a framework kinetic equation and one other quantity (Sodja, 2007:5).

The eddy viscosity in the sub-layer must be reduced by means of damping functions. These damping functions are needed to numerically stabilise the model and reduce the requirement of excessive grid resolution near the wall Menter (1994:5) and Suga (1998:4). An important factor, and arguably a major reason for damping functions, is their ability to produce the mean velocity field. Therefore, the relationship between the eddy viscosity model and the damping function is vital for a proper representation of near the wall behaviour of the fluid.

The isotropic turbulent eddy viscosity is defined as (Chan, 2000:2):

$$\nu_T = C_\mu f_\mu \frac{k^2}{\varepsilon} \quad \textbf{2.10}$$

Where C_μ a turbulent viscosity parameter is equal to 0.09 and f_μ is a wall damping function.

2.4.2 Overview: The standard k-ε model

The standard k-ε model is a linear eddy viscosity model. The kinetic energy equation (k) and the rate of dissipation of turbulent kinetic energy (ε) assume that the turbulent viscosity μ_t is isotropic. This means that the ratio between Reynolds stress and mean rate of deformation is the same in all directions. However, turbulence is always non-isotropic in a turbulent boundary layer. Hence, there are flow regimes where non-isotropic effects are important. These include flows with strong curvature, swirling flows flows with strong acceleration or retardation (Davidson, 2003:40). Such flows are predominant inside a pipe bend, e.g. flows under centrifugal forces, secondary flows and separation. Thus, if a turbulent model fails to address these effects, it leads to inaccurate flow predictions.

2.4.2.1 The standard k-ε equations

In general, the standard k-ε model is good for plane and radial jet problems. It does not perform well for strong adverse pressure gradients such as those that occur along the inner wall of a bend. Although the standard k-ε model was developed for simulating highly turbulent flows it provides limited accuracy in computational fluid dynamics (CFD) when flows have low velocities, dead zones, and flow separation and reattachment areas (Raven *et al*, 2007:558). It is therefore not recommended for separated flows. The standard k-ε model tends to predict the onset of separation too late as well as to under-predict the extent of separation (Rigas *et al*, 2007:171). Due to the model's poor performance in regions near the wall, it has been found that direct numerical simulation (DNS) is a better option in the region close to the wall, while the k-ε model can be used for regions further away from the wall (Zamora *et al*, 2006:2).

The standard k-ε model by Launder and Spalding (1974) is composed of a set of equations that have additional non-linear partial differential equations to the set of transport equations (Versteeg & Malalasekera, 1995:70). These equations are solved simultaneously to obtain solutions to turbulent flows. The equations are written in terms of the turbulent kinetic energy (k) and turbulent dissipation rate (ε), which are as follows:

$$\frac{\partial(\rho k)}{\partial t} + div(\rho k \mathbf{U}) = div\left[\frac{\mu_t}{\sigma_k} grad\ k\right] + 2\mu_t E_{ij} \cdot E_{ij} - \rho\varepsilon \qquad \textbf{2.11}$$

$$\frac{\partial(\rho\varepsilon)}{\partial t} + div(\rho\varepsilon \mathbf{U}) = div\left[\frac{\mu_t}{\sigma_\varepsilon} grad\ \varepsilon\right] + C_{1\varepsilon}\frac{\varepsilon}{k} 2\mu_t E_{ij} \cdot E_{ij} - C_{2\varepsilon}\rho\frac{\varepsilon^2}{k} \qquad \textbf{2.12}$$

Where:

$$\mu_t = C\rho\Gamma\ell = \rho C_\mu \frac{k^2}{\varepsilon} \qquad \textbf{2.13}$$

$$\Gamma = k^{1/2} \qquad \ell = \frac{k^{3/2}}{\varepsilon} \qquad \textbf{2.14}$$

The turbulence equations that have damping functions contain closure coefficients which are used to close equations. These coefficients are found experimentally through computer optimisation (trial and error). The coefficients of the k-ε model are as follows:

C_μ = 0.09; σ_k = 1.00; σ_ε = 1.30; $C_{1\varepsilon}$ = 1.44; $C_{2\varepsilon}$ = 1.92

2.4.3 Overview: The RNG (Re-Normalisation Group) k-ε model

A need arose to improve the standard k-ε turbulence model because does not accurately predict the re-circulating flows and complex shear layers found in flows subject to curvature. The main flaw of the standard k-ε model was its dissipative nature. An investigation by Papagergakis & Assanis (1999:1) found that the linear RNG k-ε model gave much improved results over the standard k-ε for recirculation flows due to its less dissipative nature. The different forms of the k-ε models are differentiated by the way the closure conditions are defined and the manner of computing constants. Hence, the fundamental nature of the RNG k-ε model is via the constants that have been explicitly calculated. Thus, the renormalization group is described as follows:

2.4.3.1 The RNG k-ε equations

$$\frac{\partial \rho k}{\partial t} + div(\rho k \mathbf{U}) = div\left[\alpha_k \mu_{eff}\, grad\, k\right] + 2\mu_t E_{ij} \cdot E_{ij} - \rho\varepsilon \qquad \textbf{2.15}$$

$$\frac{\partial \rho \varepsilon}{\partial t} + div(\rho \varepsilon \mathbf{U}) = div\left[\alpha_\varepsilon \mu_{eff}\, grad\, \varepsilon\right] + C_{1\varepsilon}^{*} \frac{\varepsilon}{k} 2\mu_t E_{ij} \cdot E_{ij} - C_{2\varepsilon}\rho \frac{\varepsilon^2}{k} \qquad \textbf{2.16}$$

Where:

$$\mu_{eff} = \mu + \mu_t \qquad \textbf{2.17}$$

$$\mu_{eff} = \rho C_\mu \frac{k^2}{\varepsilon} \qquad \textbf{2.18}$$

The closure coefficients in the RNG k-ε model are:

$C_\mu = 0.0845$; $\alpha_k = \alpha_\varepsilon = 1.39$; $C_{1\varepsilon} = 1.42$; $C_{2\varepsilon} = 1.68$

And $C_{1\varepsilon}^{*} = C_{1\varepsilon} - \dfrac{\eta\left(1 - \eta/\eta_o\right)}{1 + \beta\eta^3}$; $\eta = \left(2E_{ij} \cdot E_{ij}\right)^{1/2} \dfrac{k}{\varepsilon}$; $\eta_o = 4.377$; $\beta = 0.012$

2.4.4 Overview: The Wilcox k-ω model

The turbulence models, i.e. k-ε and RNG k-ε do not to accurately predict flow separation in adverse pressure gradients. They fail to address important parts in internal and external flow applications by not accounting for the physics concerning flow separation.

Therefore, an improvement on k-ε and RNG k-ε models was needed. The Wilcox k-ω model developed in 1994 replaces ε by an equation ω which is a dissipation rate per unit turbulent energy. The ω is easier to integrate and therefore it becomes more robust and can be integrated in the sub-layer without the need for an addition of non-linear damping functions (Zamora *et al,* 2006:4). As a result, it addresses the near wall treatment for Low-Reynolds number computations. Low-Reynolds number here refers to the sub-layer region where low y^+ values exist and have a resolution of $y^+ < 2$.

2.4.4.1 The Wilcox k-ω equations

$$\frac{\partial \rho k}{\partial t} + div(\rho k \mathbf{U}) = div\left[\left(\mu + \frac{\mu_t}{\sigma_k}\right) grad\ k\right] + P_k - \beta^* \rho k \omega \qquad \textbf{2.19}$$

$$\frac{\partial \rho \omega}{\partial t} + div(\rho \omega \mathbf{U}) = div\left[\left(\mu + \frac{\mu_t}{\sigma_\omega}\right) grad\ \omega\right] + \alpha \frac{\omega}{k} P_k - \beta \rho \omega^2 \qquad \textbf{2.20}$$

The closure coefficients in the Wilcox k-ω model are:

$$\beta^* = 0.09; \quad \alpha = 5/9; \ \beta = 0.075; \ \sigma_k = 2; \ \sigma_\omega = 2$$

The unknown Reynolds stress tensor, τ, is calculated from:

$$\tau = \mu_t 2s - \rho \frac{2}{3} \delta k$$

2.4.5 Overview: The Shear Stress Transport (SST) model

Menter (1994) proposed combining two turbulence models, namely the k-ε and k-ω. The originator of this model applied a blending function to ensure a smooth transition between the k-ε and k-ω models (Iudecello, 2008:66). The k-ω model is effective in the viscous sub-layer while the k-ε model, on the other hand, is effective for free-stream flow. In essence, the k-ε model compensates for the lack the k-ω model has on free-stream modelling and *vice versa*. The SST as a combination of the two models provides best solution to flow separation as an important phenomenon in internal and external flows. Overall, the SST model has the ability to demonstrate the particle behaviour and the reattachment length after separation (Siriboonluckul *et al,* 2005:6).

The SST model is superior to the previously discussed turbulence models. It manages to perform better because it takes into account the transport of the turbulent shear stress and the inclusion of transform effects into the formulation of the eddy-viscosity.

2.4.5.1 The Shear Stress Transport (SST) equations (Siriboonluckul *et al,* 2005:4):

$$\frac{\partial \rho k}{\partial t} + div(\rho k \mathbf{U}) = div\left[\left(\mu + \frac{\mu_t}{\sigma_k}\right) grad\, k\right] + \overline{P} - \beta^* \rho k \omega \quad \textbf{2.21}$$

$$\frac{\partial \rho \omega}{\partial t} + div(\rho \omega \mathbf{U}) = div\left[\mu + \frac{\mu_t}{\sigma_\omega}\, grad\, \omega\right] + \frac{\gamma}{\nu_t}\overline{P} - \beta \rho \omega^2 + (1 - F_1) 2\rho\sigma_{\omega 2} \frac{1}{\omega}\, grad\, k * grad\, \omega \quad \textbf{2.22}$$

Terms in E.q 2.21 and 2.22 are explained as follows:

- $\beta^* \rho k \omega$ and $\beta \rho \omega^2$ represents the dissipation of k and ω due to turbulence
- $\mu + \frac{\mu_t}{\sigma_k}$ and $\mu + \frac{\mu_t}{\sigma_\omega}$ represents diffusivity k and ω due to turbulence
- $(1 - F_1) 2\rho\sigma_{\omega 2} \frac{1}{\omega}\, grad\, k * grad\, \omega$ represents the cross-diffusion term

Where:

$$\overline{P} = -\rho \overline{u_i u_j} \frac{\partial U_j}{\partial x_j}\ , \beta^* = 0.09$$

The constants are expressed in terms of the blending function " F_1 "are: $\beta = F_1 \beta_1 + (1 - F_1)\beta_2$

Where, β_1 and β_2 stand for coefficients of the $k - \omega$ and $k - \varepsilon$ model respectively, for which the following values are recommended:

$$\sigma_{k1} = 2\,; \sigma_{k2} = 1\ ; \sigma_{\omega 1} = 2\,;\ \sigma_\omega = 1.168\,; \beta_1 = 0.075\,; \beta_2 = 0.0828$$

With the blending function F_1 defined as

$$F_1 = \tanh\left(\arg_1^4\right)\ , \arg_1 = \min\left(\max\left(\frac{\sqrt{k}}{\beta^* \omega y}; \frac{500\nu}{y^2 \omega}\right); \frac{4\rho\sigma_{\omega 2} k}{CD_{k\omega} y^2}\right), CD_{k\omega} = \max\left(2\sigma_{\omega 2} \frac{1}{\omega} \frac{\partial k}{\partial x_j} \frac{\partial \omega}{\partial x_j} : 10^{-20}\right)$$

A limiter, similar to the introducer by Durbin (1996), is included to prevent the excessive growth of the turbulent shear stress.

$$\mu_t = \frac{\rho a_1 k}{\max\left(a_1\omega : \sqrt{2SF_2}\right)} \qquad \text{where:} \qquad F_2 = \tanh\left(\arg_2^2\right),\ \arg_2 = \max\left(\frac{\sqrt{k}}{2\omega y}; \frac{500\nu}{y^2\omega}\right), \quad a = 0.31$$

Where:

y is the distance to the next surface

2.5 The boundary layer theorem

2.5.1 Introduction to the boundary layer theorem

Euler who gave a description of a fluid flow by using a three-dimensional model for pressure and velocity fields in a form of infinitesimally small fluid elements was no doubt a pioneer in theoretical fluid dynamics. However, he ignored viscosity. He did not think friction could be acting on the motion of fluid elements (Anderson, 2005:42). In 1904, Ludwig Prandtl demonstrated that the Navier-Stokes equations which describe the motion of a fluid can be simplified to give solutions for flows at high Reynolds numbers. Additionally, these equations were the bases for his boundary layer theory (McMahon, 2003:1).

Prandtl's hypothesis was that the velocity on the surface was zero (no-slip condition because of the existence of friction). The frictional effects were experienced only in a boundary layer, which is a thin region near the wall surface. However, as it has been understood two centuries before his theory, inviscid flow existed outside the boundary layer but not inside the boundary layer (Anderson, 2005:43). With Prandtl's boundary layer theory there was a mathematically based quantitative way of computing friction on a surface that is submerged in a fluid. There was also a mechanism that gives an understanding of how separation is generated on a surface (Anderson, 2005:45).

2.5.1.1 Description of the boundary layer theory

In an attempt to describe the boundary layer theory, a flat plate of sufficient length and a large width has been used to demonstrate the behaviour of the fluid when it travels along it, see Fig 2.1. The main focus is the fluid flow beginning from the plate's surface leading edge to the free stream

above the surface. Here, a non-moving surface will have a zero-velocity component relative to the free stream velocity. This situation, whereby the surface of the plate brings the fluid in contact to rest (u = 0), corresponds to the primary condition of boundary layer theory which is the no-slip condition (Sayers, 1992:282).

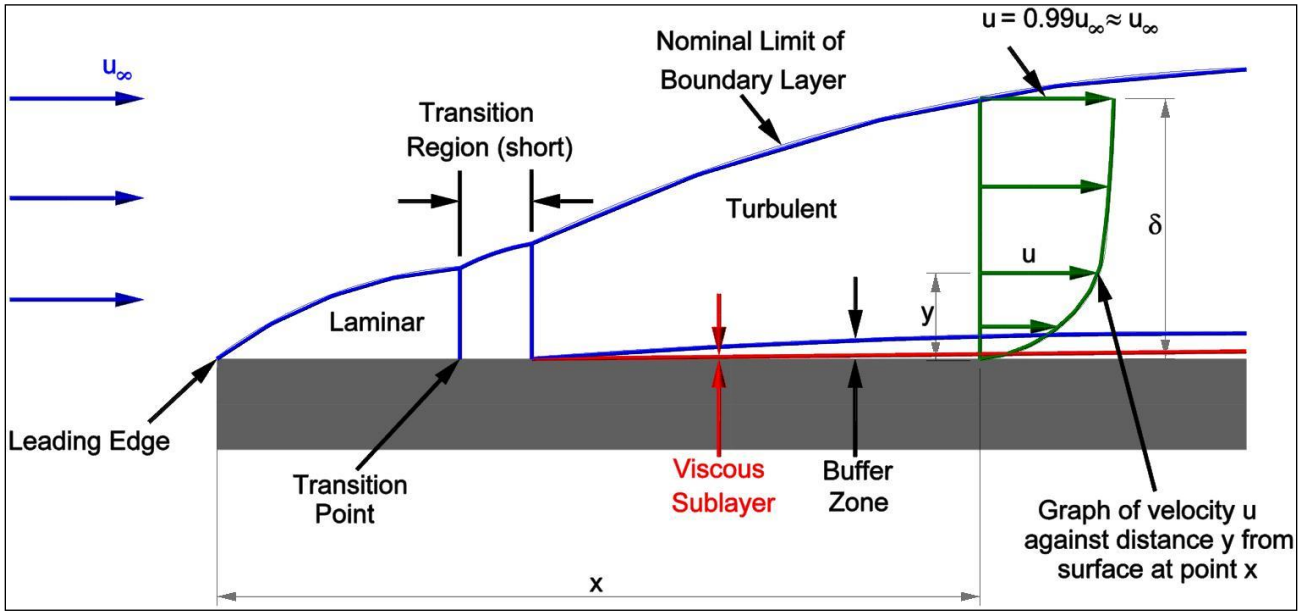

Figure 2.1: Boundary Layer on a Flat Plate, www.cortana.com/Drag_Description.htm

Boundary layer theory demarcates the start and the end of the boundary layer. In order words there is a level described by Tilton (1999:5) at which the fluid returns to the irrotational state. This state allows the fluid to be regarded as inviscid. Thus, according to Munson *et al* (1994:561) the vorticity at this region is zero and thus perfectly complements the irrotationality of the fluid. There is a feature called the boundary layer thickness "δ". Sayers (1992:282) describes it as the height above the plate's surface whereby the fluid moving parallel to the plate reaches a velocity of 99 per cent of the free stream velocity, i.e. u = 0.99 U_∞.

The boundary layer thickness on flat surfaces increases without limit in the direction of flow. However, Douglas *et al* (1995:370) considered the maximum thickness of the boundary layer in pipes to be close to its radius. This is a state, whether the fluid is laminar or turbulent where the flow be fully developed, i.e., when the boundary layer grows to fill the whole cross-section of the pipe.

Inside the boundary layer a thin layer called the laminar sub-layer exists. Its magnitude is as high as the absolute roughness of the surface (Sayers, 1992:300). Sayers (1992:300) describes the boundary layer's (inclusive of the laminar sub-layer) shear stress to be a summation of shear stresses. The shear stress, $\tau = \mu\left(du/dy\right)$ and the eddy shear stress are called the apparent shear stress expressed as, $\tau_{app} = \mu\left(du/dy\right) + \tau_{eddy}$

2.5.1.2 The boundary layer equations (Sayers, 1992:282-284):

In order to establish the boundary layer equations, the following assumptions were made:

- The fluid is two-dimensional and with constant properties.
- The terms which are very small compared to other terms were ignored.

The velocity boundary layer equations

$u \rangle\rangle v$

$\frac{\partial u}{\partial y} \rangle\rangle \frac{\partial u}{\partial x}, \frac{\partial v}{\partial y}, \frac{\partial v}{\partial x}$

The shear stress approximations are:

- No pressure gradient perpendicular to the surface.

  $\sigma_{xx} = \sigma_{yy} = 0$

- The shear stress acting on the surface is given by

  $\tau_{xy} = \tau_{yx} = \mu\left(\frac{\partial u}{\partial y} + \frac{\partial v}{\partial x}\right) \approx \mu\left(\frac{\partial u}{\partial y}\right)$

The simplified boundary layer equations are:

- Continuity equation

  $\frac{\partial u}{\partial x} + \frac{\partial v}{\partial y} = 0$

- The momentum equation in the x direction

  $u\frac{\partial u}{\partial x} + v\frac{\partial u}{\partial y} = -\frac{1}{\rho}\frac{\partial p}{\partial x} + v\frac{\partial^2 u}{\partial y^2}$

- The momentum equation in the y direction

$$\frac{\partial p}{\partial y} = 0$$

These equations mean that:

- The boundary layer pressure varies only in the x-direction.
- The pressure inside the boundary layer is equal to the pressure outside the boundary layer.

CHAPTER 3

LITERATURE REVIEW

3.1 The boundary layer in view of flow separation.

Higher losses are found in pipe bends than the losses in straight pipes of equal length. The secondary flow and flow separation cause these losses. Additional losses are due to separation and secondary flows. Separation occurs on the inner radius of the bend which is a convex surface for the flow. It results in secondary flows in the form of vortices (Jianfu & Gabriel, 2004:207).

Separation is geometry sensitive because it follows on sections where an adverse pressure exists. Modi & Jayanti (2004:321) have found, in their CFD study of pressure losses in sharp bends with a vane that separation occurs on the outer radius where an adverse pressure gradient occurs. They found that an incipient separation, i.e., point of separation, exists just about at the beginning of the curvature. Then when the flow has been fully separated the secondary flows dominate until the start of flow re-attachment some length within a bend.

3.1.1 Separation inside the 90^0 bend convex curved surface

The separation of the boundary layer from the surface is caused by an increasing pressure in the direction opposing the flow. Figure 3.1 indicates the convex surface found in a bend (inner surface). It illustrates the motion and the separation experienced by a fluid. Brodkey (1967:138-139) describes the flow that is separated from the convex surface as follows:

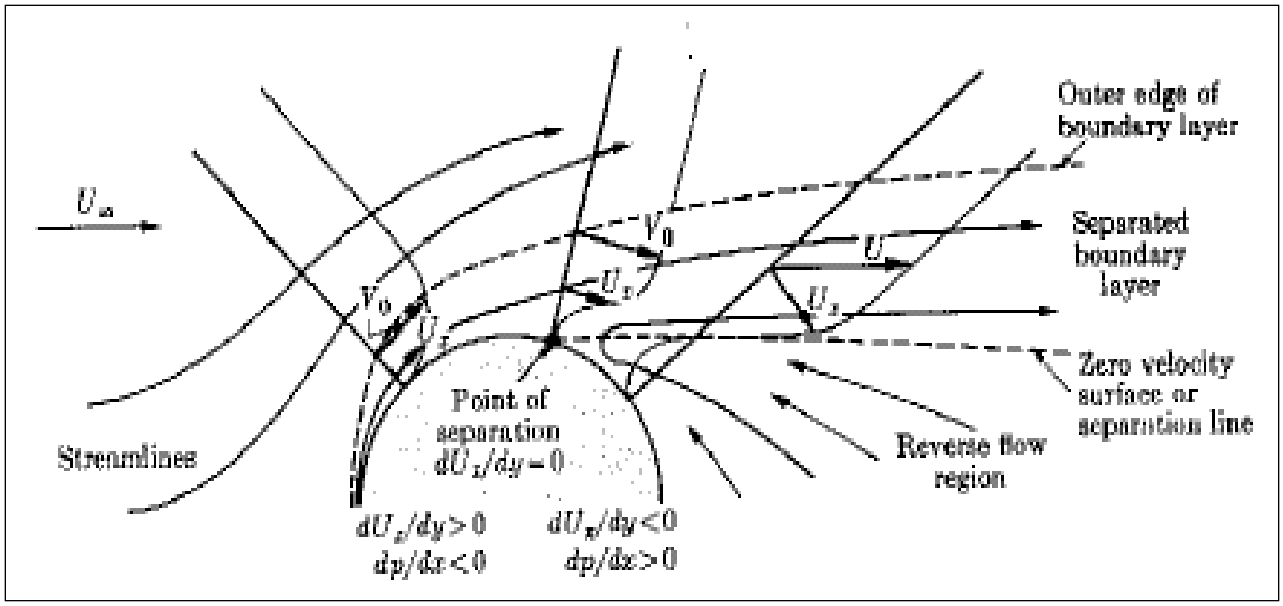

Figure 3.1: Turbulent layer over a cylindrical object, Brodkey (1967:138)

- In moving from the forward partof the curved surface the flow will experience a deceleration in moving to the rear portion. The forward portion brings about an increase in velocity $dU/dx > 0$, and a decrease in pressure $dp/dx < 0$, i.e. a favourable pressure gradient. On the rear an adverse pressure gradient exists, which is described as pressure increasing in a direction opposing the flow path $dp/dx > 0$ where velocity is decreasing $dU/dx < 0$.
- The fluid elements on the rear portion decelerate due to interactions of the pressure gradient and the shear force that exists near the wall. The viscous forces and the velocity will eventually become zero because of deceleration of the fluid elements coming to a rest.
- In the interim, the adverse pressure will continue to act and cause the fluid in that region to have a backward flow. At this point, the separation of the boundary layer from the surface starts and the flow still continues in the direction of increasing pressure.

3.2 Wake and vortex formation over a convex curved surface

A wake forms when the flow over a convex surface reaches the separation point. Its structure depends on both the Reynolds number and the detailed shape of the body. Evidence by Jawarneh and Vatistas (2006:1378) has shown that the geometrical and flow parameters have an impact on the swirl.

3.3 Head loss coefficient of an isolated bend

It is well researched that the distorted flow within a bend causes the magnitude of the head losses to be significantly higher than of an equivalent straight length of pipe. The first study of internal flow was the work of Thomson (1876). He recognised the effects of the centrifugal force in a curved geometry. Using glass tubes with different degrees of bending, Eustice (1876) conducted experiments over a wide range of Reynolds numbers, involving a large amount of flow visualisation work. Liu *et al* (1994:307) explained that the interaction between the centrifugal force and the slow motion of fluid in the boundary layer induce a secondary flow.

The flow inside the bend is three-dimensional and complex. It is due to the inertia of the fluid and the secondary motion that is generated adversely. Arada *et al* (2006) studied the inertia and viscosity effects on flow in curved pipes using the Finite Element Method. Their findings show that the complex nature of flow in curved pipes is largely due to the distortion of axial velocities and the asymmetrical wall stresses that develop in higher-shear and low pressure regions within the bend. Generally, the studies conducted so far describe the behaviour of the fluid in bend as curved streamlines in which the presence of a centrifugal force causes the pressure increase near the outer wall of the bend, starting at point A (Fig.3.2) and rise to a maximum value at B, Tony *et al* (2006:12). Therefore, in region A-B the fluid flow is opposed by an adverse pressure gradient. At the inside of the bend, the pressure decreases to point C and then rises again in the exit section. For this reason an adverse pressure gradient exists from C to D at the inside wall. The magnitude of these losses depends to a large extent on the sharpness of the curvature of the bend.

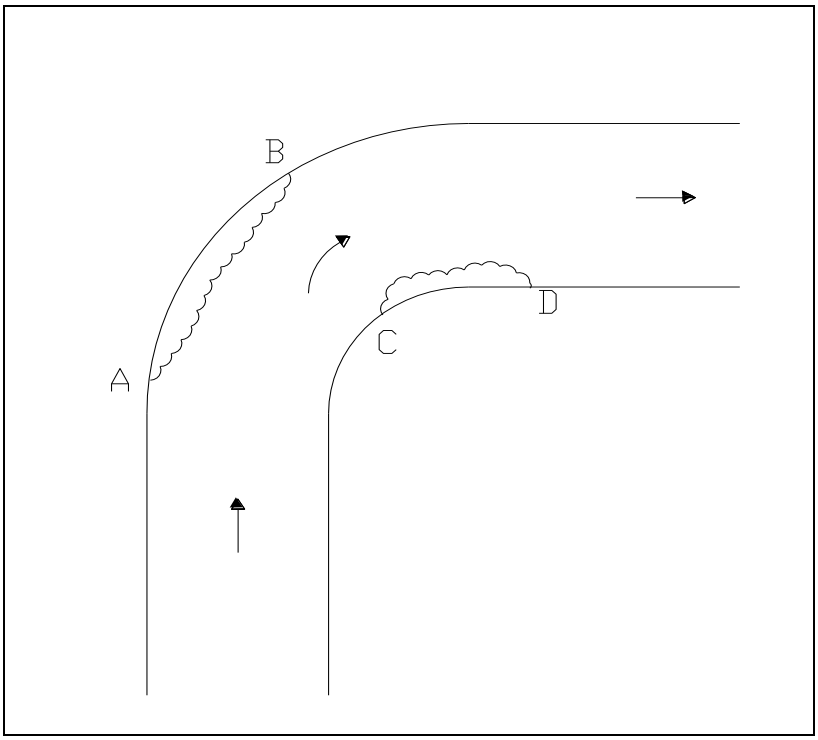

Figure 3.2: Regions of increased pressure in a pipe bend

Flow separation is a result of the geometrical elements of the bend (curvature and deflection angle). The major attributes of this increase in the pressure gradient are the centrifugal forces acting on the fluid due to a strong curvature of the bend, White (1929:661). As established by Dean (1927) in his theory of the increased resistance owing to the curvature of the bend, secondary flows perpendicular to the axial flow are formed in the bend. In the absence of the curvature, the flow near the wall travels slowly whilst in the centre it is faster. However, due to the curvature the fluid adjacent the walls moving inwardly and the centre flow moves outward because of the imbalance of the centrifugal forces on the main flow secondary flows become prevalent, Dey (2001:283). Thus, secondary flows are generated by this transverse movement of the flow across the bend, Modi & Jayant (2004:321).

The next aspect of this study is the recovery length required for the velocity profile of the fluid to reach its normal state which would resemble the $1/7^{th}$ power-law profile for turbulent flows. The insufficient recovery length found between the bends is the basis of this study. The short length ($L/d << 150$ downstream of the first bend) commonly found between bends does not give enough flow recovery length. Modi & Jayant (2004:321) deduced that the changes in the development of the velocity profile to its fully developed state becomes significant within the first ten diameters

downstream the bend. The distorted fluid carries a swirl velocity that persists for far more than 10 diameters. Ouazzaane & Benhaji's (2004:2244) findings suggest a settling length of 100 diameters.

Literature on this matter has brought understanding regarding the definition of a short length because a required downstream pipe length for flow development is set as 150D (Mukhtar *et al,* 1994:330). The effects of the downstream tangent length (as a redevelopment length to fully developed velocity profiles of either laminar or turbulent flows) affect the accurate computation of the loss coefficient of a bend (Ito, 1986:548). When computing the loss coefficient for 90^0 bends on the same plane (180^0) the sum of the two loss coefficients is multiplied by a correction factor in order to compensate for the length between the bends, Miller (1990:227). The approach taken in this study involves investigating a single loss coefficient for two bends in the same plane (bend-spacer-bend).

3.4 Experimental determination of the head loss coefficient

It is important to accurately compute the pressure drop caused by pipe bends. The curvature surfaces of pipe bends induce secondary flow which significantly affect the hydrodynamic performance of devices, viscous power loss and heat transfer (Tony *et a,l* 2006:121). The determination of the head loss coefficients of local losses (fittings) has until recently, been through experiments. Pienaar *et al* (2001:4) explains the experimental method used to obtain the loss induced due to a fitting. The overall process that the friction in the straight pipe is subtracted from the total friction loss (fittings and straight pipes) measured (Turian *et a,l* 1998:244).

A detailed procedure and an in-depth guide for determining the head loss coefficient of a fitting was provided by Marn & Primoz (2006). They state that the pressure drop that is measured consists of two components that are the pressure drop that exists in the absence of ΔP_F, and the existence of ΔP_{bend}. They formulate the composition of the total pressure drop as follows:

$$\Delta P_{tot} = \Delta P_{in} + \Delta P_{out} = \Delta P_{bend} + \Delta P_F \qquad \textbf{3.1}$$

ΔP_F accounts for the fully developed wall friction given by the Darcy-Weisbach equation for the friction loss coefficient in the turbulent region of rough or smooth pipes (*f*). The pressure drop as a result of ΔP_{bend} is presented as the sum of the pressure loss due to the wall friction ($\Delta P_{bend,F}$)and the

pressure loss (ΔP_{loss}) due to the curved flow within the bend that induces secondary flow and flow redevelopment at the exit to the bend.

$$\Delta P_{bend} = \Delta P_{bend,F} + \Delta P_{loss} \quad \textbf{3.2}$$

$\Delta P_{bend,F}$ and ΔP_F are expressed as:

$$\Delta p_{bend,F} = L_B \frac{f}{D} \frac{\rho v^2}{2} \quad \textbf{3.3}$$

$$\Delta p_F = \left(L_u + L_d\right) \frac{f}{D} \frac{\rho v^2}{2} \quad \textbf{3.4}$$

L_u and L_d are the fully developed upstream and downstream lengths of the pipe respectively

and

$$L_B = 2\pi \, r_c \big/ 4$$

L_B is the length and r_c is the curvature ratio of a 90^0 pipe bend respectively.

Thus, by combining equations (3.1-3.4) the pressure drop across the bend is expressed as:

$$\Delta P_{loss} = \Delta P_{tot} - \left(L_u + L_B + L_d\right) \frac{f}{D} \frac{\rho v^2}{2} \quad \textbf{3.5}$$

Equation 3.5 leads to the final determination of a loss coefficient for a fitting, i.e., isolated bend, as found by Ward-Smith (1980) as:

$$k = \frac{\Delta P}{1/2 \, \rho v^2} \quad \textbf{3.6}$$

3.5 Head loss coefficient of two bends with an interaction

From literature the established basis for determining the loss coefficient is comparison with the pressure loss in a fully developed flow over the same length. The head loss coefficient is a function of the tangential length (upstream and downstream of a bend) (Ito, 1987:548). Hence, the loss coefficient of any fitting (as a flow disturbance), i.e., bends, wyes, valves, etc., is best computed

when the flow entering and exiting the disturbance is fully developed. This understanding caused past researchers to identify the need to investigate how the loss coefficient would be affected if two components (disturbances) are closely spaced to each other. In such a configuration the distorted flow after exiting the first bend it enters the second bend not fully developed due to the inadequate recovery length between the bends. Therefore, there ought to be a different computing approach to the loss coefficient as it would be incorrect to treat the bends with this configuration as isolated bends (Modi & Jayant, 2004:321).

The spacing ratio is a ratio of the length of the straight pipe between bends to the inside diameter of the pipe. Therefore, by having a length range of one diameter to ten diameters would mean the length is below an acceptable flow settling length of 100 diameters (Ouazzane & Benhadji, 2002:224). This is the premise of this research which has expanded on the work done by (Papworth & Miller, 1974:27). They established an interaction factor that was applied to correct the head losses in two components with interaction (spacer). Miller (1990:228) further points out that the total loss does not only depend on the space between bends, but also on the directions of the bends and the planes of their orientation (Daugherty & Franzini, 1977:228). Initially the short length between the pipe bends was understood to have an influence on the value of the head loss coefficient but this was not quantified. Quantification was only introduced when Miller (1990:80) demonstrated that there is a direct interference between pressure and flow distributions when bends are less than two pipe diameters apart.

Gan and Riffat (1996) calculated the loss coefficients, by means of CFD, for wide angle diffusers. They coupled this investigation with the prediction of the effects on the loss coefficient of a bend preceding the diffuser at various spacer lengths. This study builds on their work through using CFD. Their findings correlated with Miller's findings. Their common base was that flow and pressure interacts between the components, i.e., diffuser and a bend. Determining the loss coefficient for such a configuration is not as simple as summing the loss coefficients of the individual components, but an interaction factor must be used to account for the interaction. The extent of the interaction is dependent on the spacer length.

Coffield *et al* (1997) proposed a generic term that is self-explanatory for the loss in components with a spacer between them and various orientations as "the irrecoverable pressure loss". Coffield *et al* (1997:6-7) found that the pressure drop of elbows with a separating distance of less than 20

diameters is less than twice the pressure drop of a single elbow. It was found that the irrecoverable loss coefficient varies based on the following conditions

- Shorter separating distances between elbows allow swirl in a form of counter rotating vortices from the first elbow to feed more directly into the second elbow.
- Then for longer separating distances, more friction pressure loss is experienced. After the second elbow the swirl intensity is more than after the first elbow.

Modi & Jayant (2004) carried out CFD simulations on successive 90^0 sharp bends connected by a short straight section for ducting systems. They computed the loss coefficients of the sharp bends joined at mutual planes in three configurations, see Fig.3.3 (180^0, 90^0 and the 0^0 angle). Modi & Jayant (2004:327) found that each case was different in terms of the magnitude of the loss coefficients but what was common that the loss coefficient (as a single value in view of two bends) increases with increase of the distance between the bends.

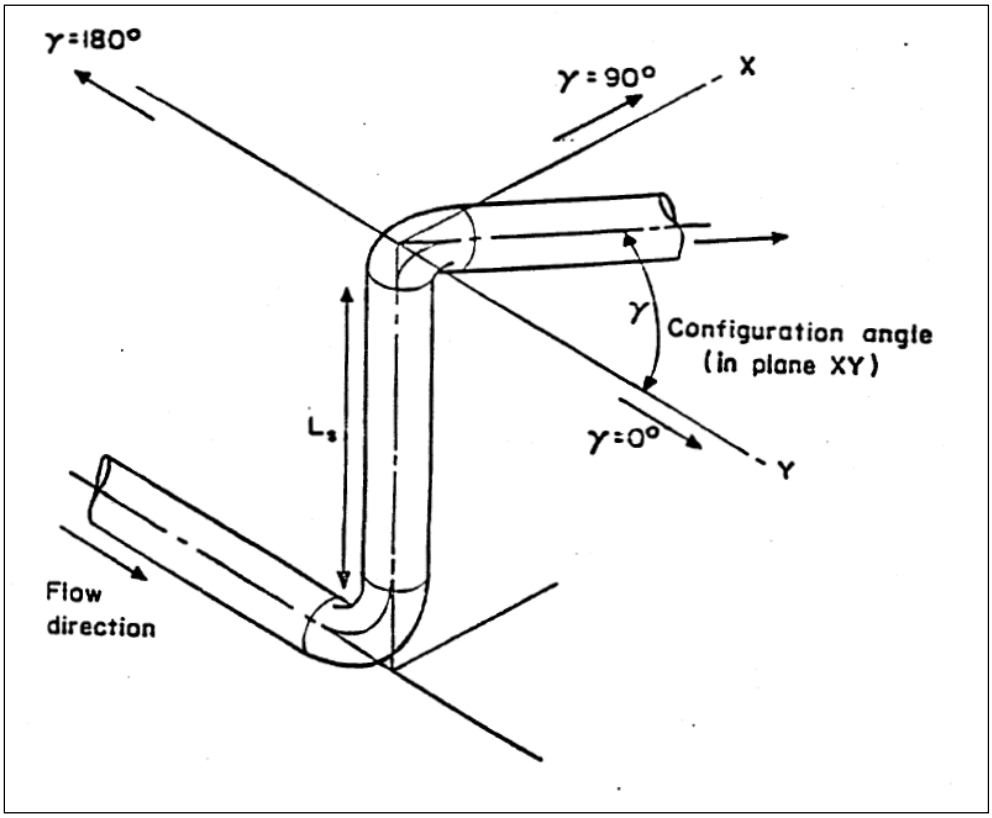

Figure 3.3: Orientation angles of bends, Cofield *et al* (1997:12)

Further contributions on this subject came from Maharudrayya *et al* (2004) when they investigated the geometric effects viz., spacer between sharp bends, on the pressure losses. These pressure losses if not minimised, increase pumping power so that the efficiency of the system will be compromised (Maharudrayya *et al*, 2004:1). Using CFD, they established three-regime correlations for excess loss coefficient as a function of the Reynolds number, aspect ratio, curvature ratios and spacer lengths between the channels. Overall, Maharudrayya *et al* (2004:5-6) came to the same conclusion as past researchers that the flow separation in the second bend is suppressed by the presence of the upstream bend. This effect becomes less when the separating distance (spacer) is increased. This, therefore, means that a loss coefficient for two bends increases as space length is increased.

In the previous chapters the theory of CFD and its N-S equation, the boundary layer theorem, the theoretical and experimental methods of computing the head loss coefficient of isolated bends and closely spaced bends have been presented. The next chapter provides findings of a CFD investigation of smooth closely spaced pipe bends.

CHAPTER 4

COMPUTATIONAL FLUID DYNAMICS

4.1 Introduction

This chapter documents the numerical investigation of the effects of the length of the straight pipe (spacer) between 90^0 circular pipe coplanar bends. The objective was to characterise this effect in terms of a head coefficient. The effects on the head loss coefficient were investigated taking into account the following attributes:

- The velocity profiles of the flow in a bend-spacer-bend configuration.
- The curvature ratio of the bends.
- The Reynolds number of the fluid flow
- The spacer L/d ratio

This resulted in a correlation for determining the loss coefficient.

The configuration that was simulated, comprised of two 90^0 bends with a spacing ratio (L/d) from one to ten at Reynolds numbers from $7.3x10^4$ to $5.8x10^5$. This range of Reynolds numbers encompassed the capabilities versions of experimental apparatus considered for the experimental part of the work.

ANSYS® CFX® 11 was used to model the configuration. The objective was to expand on previous findings that the value of the loss coefficient for closely spaced bends is less, than for a spacer with sufficiently long separation (Modi & Jayant, 2004:328), but increasing as the separation length increases. Furthermore, the findings of an increase in the pressure drop with increase in curvature of the closely spaced bends were investigated.

4.2 CFD Modelling

The finite volume method was used for CFD modelling. It numerically solves the fundamental governing equations of flow (conservation of mass and momentum equations) for incompressible isothermal flow. These equations are non-linear, second order partial differential equations. Once

discretized, each partial differential equation is converted into a set of non-linear algebraic equations. The discretization of the equations involves using a second order high resolution scheme. In order to reduce iteration errors in the solution, a convergence criterion of $1x10^{-10}$ was applied. The simulations were performed on a computer with 1GB RAM and a processing speed of 1.8GHz in a Windows XP operating system. The average time taken per simulation was approximately 6hrs 40min to converge in 200 iterations.

4.2.1 Topology

Figure 4.1 shows the fluid domain. It is meshed using tetrahedral elements. In Fig 4.1 (a), the fluid in the two bends and the spacer, as well as the upstream and downstream pipes are modelled.

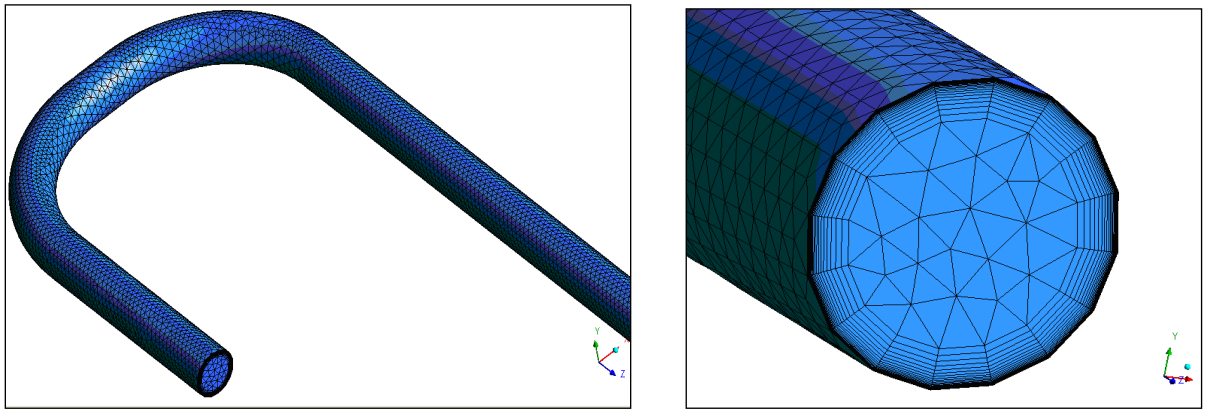

(a) (b)

Figure 4.1: (a) Topology of a tetrahedral meshed fluid for the full geometry. (b) Inlet with prismatic layers.

Fig. 4.2 shows the geometry of two 90^0 bends separated by a short straight pipe. The lengths of the tangent pipes (pipes upstream and downstream of the bends), were to ensure fully developed conditions at the inlet and at the outlet.

The inside diameter (D) of the pipe was taken as 65mm. This is an industrial scale pipe size, but of small enough diameter that laboratory testing would be feasible. The bends were 90^0 long radius bends of curvature ratios of three, four and five. The lengths of the tangent pipes for the inlet and outlet were five diameters and 50 diameters respectively. The outlet length is as guided in ESDU CFD Best Practise Guidelines for Internal Flow (2007:7), to provide for fully developed flow of a turbulent fluid.

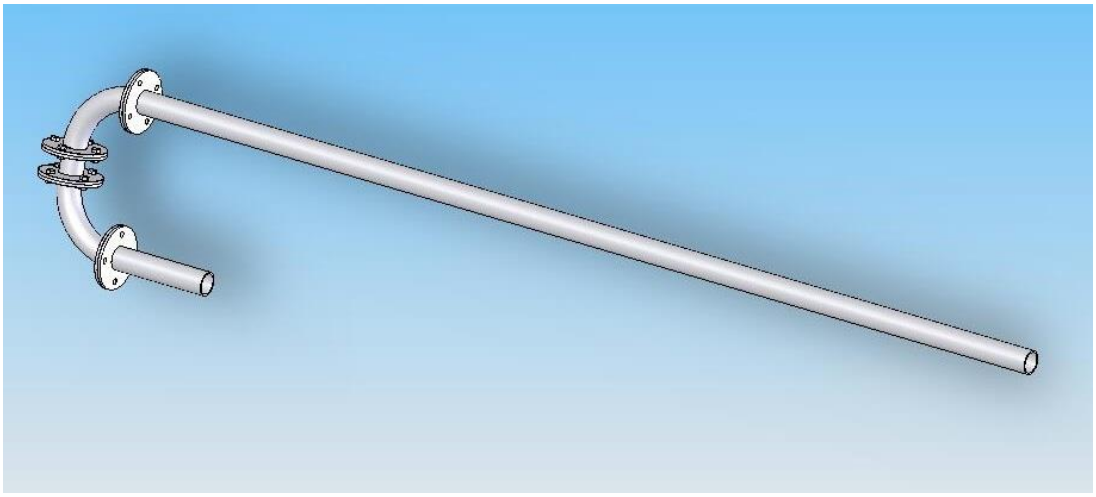

Figure 4.2: Geometry indicating the inlet tangent (5D), test section and outlet tangent (50D)

The boundary condition at the inlet of the pipe was assumed to be fully turbulent with the inlet velocity profile a fully developed one. The 1/7th power-law formula (Eq. 4.1) was chosen to represent the mean velocity of the turbulent flow in a pipe.

$$u_{inlet} = w_{local}\left(1 - r_w / R\right)^{1/7} \qquad \textbf{4.1}$$

The modelling parameters used, are given in Table. 4.1.

Table 4.1: Modelling parameters

Feature	Description	Details used/achieved
Grid	• Tetrahedral with prismatic layers • Wall functions, the viscosity-affected sub-layer • Minimum expansion factor for prismatic layers • Grid size	• 25 prismatic layers • y^+ = 0.768 • 1.04 • 9 mm
Convergence Criterion	• RMS residuals to ensure mass, pressure and velocity residuals are less than threshold of 10^{-5}.	• Asymptote of 10^{-10} Wall Scale = $6x10^{-9}$ • P-Mass = $2x10^{-9}$

	• Higher resolution scheme		• 2nd order
Boundary Conditions	• **Inlet Boundary**	• Upstream pipe length • Inlet velocity profile • Turbulence intensity at inlet of the pipe	• 5D • 1/7th power law • 5%
	• **Outlet Boundary**	• Downstream pipe length • Relative pressure	• 50D, turbulent flow • 0 Pascal
Time Dependence and Turbulence Modelling	• Transient calculations • Iteration • Shear Stress Transport (SST) model with AUTOMATIC near-wall treatment		• For flow separation • 200 • For separation in pipe bends

The modelling parameters presented in Table 4.1 were chosen with the aim of ensuring that the results were at the required level of accuracy. They are presented here in four main parameters normally considered for accurate computational modelling.

The parameters detail values or categories of the parameters were obtained:

- **Grid**: The grid near the wall needed to have a fine mesh in order to represent flow behaviour in that region. The solution therefore required 25 prismatic layers on the walls for a 9mm grid size mesh (explained in section 4.2.2) for adequate boundaries of low Reynolds number models since they require modelling in the viscous sub-layer. Thus, after iterative modelling for the most accurate near-the-wall turbulence modelling, the viscous sub-layer value was within the range of $0 \leq y^+ \geq 5$. The final number of prismatic layers (25) at the default expansion factor of the software made it possible to achieve $y^+ = 0.768$.
- **Convergence Criterion**: Since this study involves a steady state is was important to iterate in time until a steady-state is reached. Iudicello (2008:77) defines convergence as"…the property of a numerical method to produce a solution which approaches the exact solution

as the grid spacing is reduced to zero". It was found that the convergence has criterion an acceptable magnitude of 10^{-9} at 200 iterations in a 2^{nd} order high resolution scheme.

- **Boundary conditions**: The Dirichlet and Neumannn mathematical formulations were applied for the inlet and outlet respectively, for the boundary conditions. The inlet conditions of the computational domain involved a defined velocity profile ($1/7^{th}$ power law) and a turbulence intensity of 5%. This figure was chosen because it is assumed that the turbulence at the inlet is moderate. Hence, only 5D of a straight pipe was used as an upstream tangent length. The outlet conditions meant that fully developed flow was assumed at 50D downstream of the second bend. The choice of zero pressure at the outlet is a general practice in CFD because the second derivative of the velocity components and the turbulent quantities are assumed to be zero in the main flow direction.
- **Time dependence and turbulence modelling**: The advantage of the SST model in computing near wall turbulence is explained in section 2.1.5. Nevertheless, the model still required 200 time-step iterations to allow for convergence.

4.2.2 Grid Sensitivity study

In computational modelling, the accuracy of the results is dependent on the sensitivity to the domain's grid size. Figure 4.3 shows the varying grid size of tetrahedral elements of double bends that are closely spaced. Starting with the default, the grid size was a constant y^+ value ($y^+ = 0.768$). The y^+ value is as result of the number of prismatic layers placed at the wall. This was kept constant throughout the refinement of the grid size. The results for pressure difference acrpss the configuration as a function of the grid size are shown below.

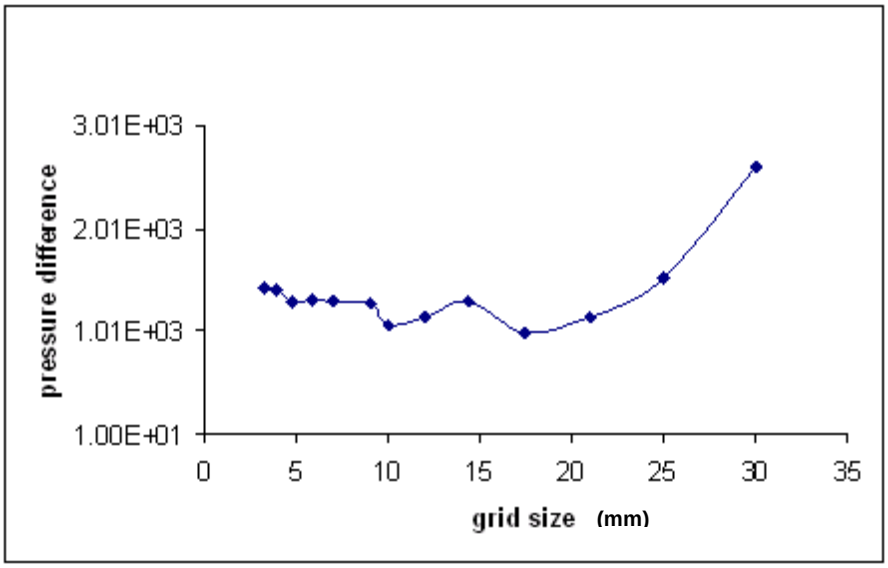

Figure 4.3: Grid sensitivity with the pressure difference as key parameter

Finer grids require more elements, using more computer memory. Due to the limitations in the academic license for ANSYS® CFX® 11.0, also only models with up to a million elements could be solved. Therefore, the next step was to select a grid size that could be accommodated by the memory available on the computer. It was found that for finer grids, the memory required to solve was more than what the operating system would allocate, see Fig. 4.3. Thus, a less fine grid size of 9mm was selected, but without compromising convergence.

To achieve an adequate level of the residuals, the number of iterations was increased from the default of iterations 100 to 200 iterations. All variables residual were less than 10^{-5}, demonstrating sufficient convergence.

4.2.3 Turbulence models (model sensitivity)

Multiple turbulence models are available in ANSYS® CFX ® 11 and they do not give the same solution. The different commercial turbulence models are built for different type of flows. It was decided to select one turbulence model, viz. the Shear Stress Transport (SST) model, as the benchmark, and to compare three other turbulence models with it. The three models selected were k-ε, RNG k-ε and k-ω.

Such comparisons are generally conducted with respect to how each model will perform against experimental work or literature studies. In this instance, the selected turbulence models were compared to Miller's (1990) findings on the corrected loss coefficient of interacting bends, i.e. bend-spacer-bend.

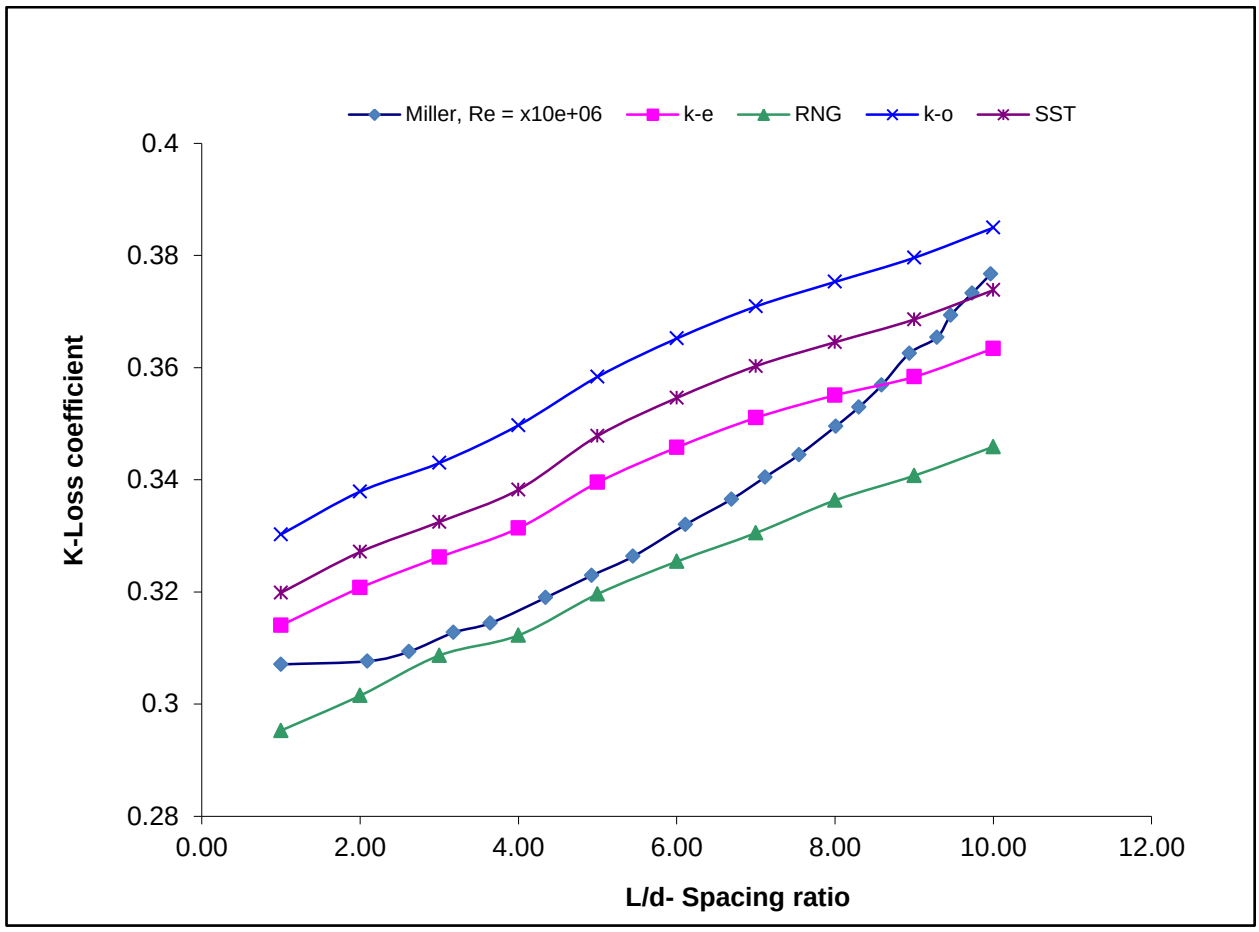

Figure 4.4: Validation of the various turbulence models

It can be seen from Fig 4.4, that the k-οω and RNG k-ε models clearly do not provide good correlations with Miller's data. Further information with respect to the other models and their comparison on eddy viscosity will be detailed in the sections that follow.

Figure 4.5 shows the range covered by each model regarding the prediction of eddy viscosity. The modelling parameters described in Table 4.1 were used per model for all the cases selected for this study. The ability of the turbulence model to predict eddy viscosity from the wall is demonstrated in Fig 4.5. For each turbulence model the maximum and minimum values of computed eddy viscosity

are shown. A model that predicts a lower of minimum eddy viscosity provides greater detail near the wall. As seen from Fig 4.5, the SST model has the smallest range of eddy viscosity predictions. These results present the SST model as better for near the wall effects, which are an important part of this study. Since separation of flow propagates from the boundary layer separation, it is important to use a turbulence model that will simulate this best.

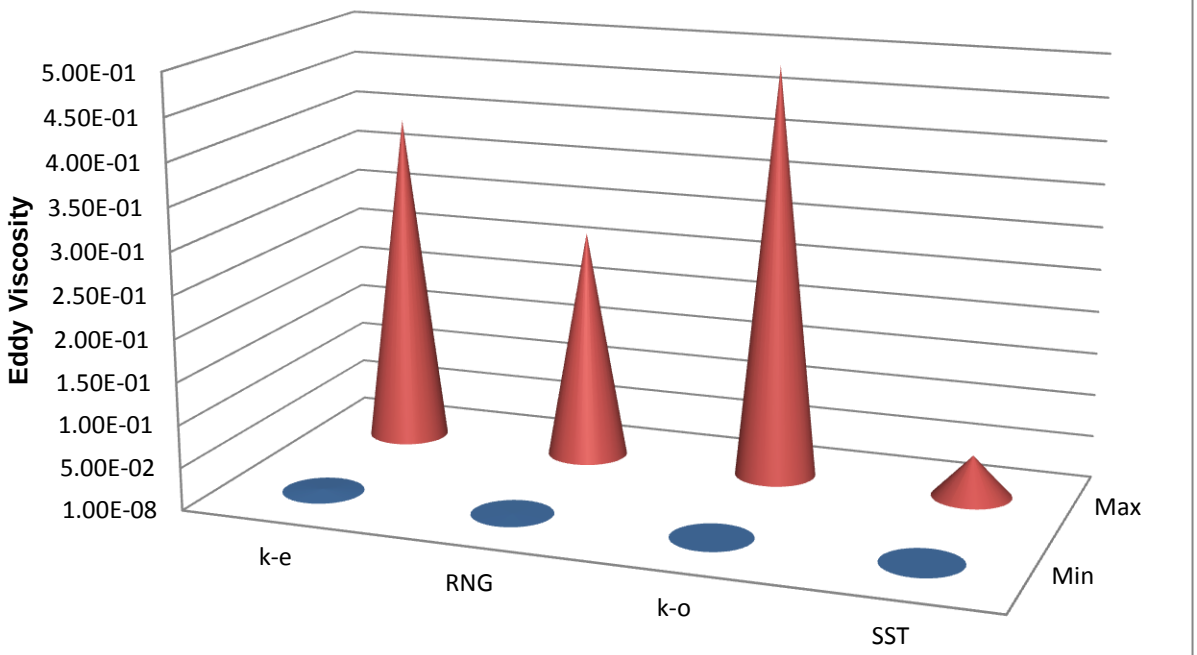

	k-e	RNG	k-o	SST
Min	2.39E-03	5.71E-04	1.29E-05	1.27E-09
Max	3.92E-01	2.72E-01	4.85E-01	4.90E-02

Figure 4.5: Changing Eddy Viscosity for the turbulence models. Constant y^+ and r/d and various Reynolds numbers

In this study, part of verification of the models involved investigating a turbulence model that would best present separation of flow on areas where is it prevalent. The velocity profiles of all four turbulence models have been plotted for areas where flow separation and the reattachment of flow are known to exist. This approach has been taken in order to see which turbulence model best addresses separation and thus, with previously mentioned modelling parameters (Table 4.1)

qualifies to be the model to be used for the rest of the CFD investigation. Figure 4.6 depicts various turbulence models where axial velocity profiles on the symmetry plane are plotted on specific positions in the geometry. Specific positions of interest are as follows:

- The inlet and the exit of the first bend.
- The entrance of the spacer (hydraulic pipe length).
- And the remainder of the spacer to the entrance of the second bend.

The axes of the graphs were made dimensionless by dividing:

- Specific velocity by the free stream velocity (Y axis)
- Specific position by the radius of the pipe (X axis)

Zero on the z/R parameter represents the inner wall of the pipe whilst the highest value, being number two represents the outer wall. All the models present, in general, the expected distorted velocity profile from the inlet's $1/7^{th}$ power law velocity profile. As flow exits the first bend, the centrifugal force owing to the curvature sends the flow to the outer wall. The same physics is shown by all the models. However, the models which in their nature do not model on the viscous sub-layers, i.e. k-ε and RNG k-ε, present this profile with a delay. The k-ε and RNG k-ε models begin the velocity profile at 0.4 of the u/V_m parameter; see Fig. 4.7, whilst the k-ω and SST begin at 0.1. It was deduced that the k-ε and the RNG k-ε models under-predict the onset of separation because their velocity profiles suggest that separation occurs at a later higher velocity.

A further important selection criterion is which model best presents the onset of re-attachment of flow. It has been found through the velocity profiles of the SST turbulence model in Fig 4.6 that flow starts to show re-attachment on the outer wall from ten diameters (10D) as though flow is taking up its normal velocity profile of a turbulent flow, i.e., the $1/7^{th}$ power law. However, there is still separation from the inner wall because there are no values in the u-direction (radial velocity) of the velocity component that suggest there is flow from the wall towards the centre. On contrary, the k-ε and the RNG k-ε with a slight exception on k-ω, suggest that there is flow from the inner wall and the beginning of the re-attachment of a turbulent velocity profile is as early as ten diameters downstream the first bend.

The SST model shows that there is still separation at entry to the second bend, while the other models (k-ω, RNG k-ε and k-ε) suggest that flow has started to re-attach. This difference in the

models' prediction confirms that these models under-predict flow separation. It does so, on a much earlier onset than the k-ε and the RNG k-ε models. It is seen from the SST model in Fig. 4.6 that the value indicating separation starts just over the 0.1 u/Vm value, whilst the k-ε, RNG k-ε and k-ω models indicate that separation stopped at a just under the 0.5 u/Vm value.

The SST model achieved a significantly more accurate representation of the flow than the after turbulence models included in this comparison. It can produce results even on the smallest range of eddy viscosities. Modelling is performed in the sub-viscous layer of the fluid (boundary layer). Therefore, the detachment of the fluid from the surface is detected accurately. By using it, the modelling results will be more reliable and much closer to the physics of motion and behaviour of the fluid

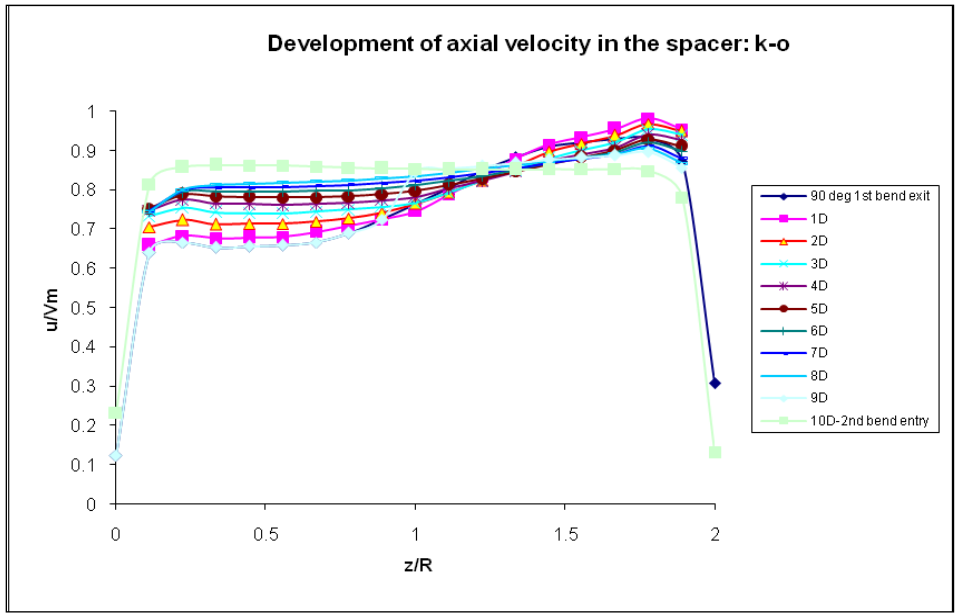

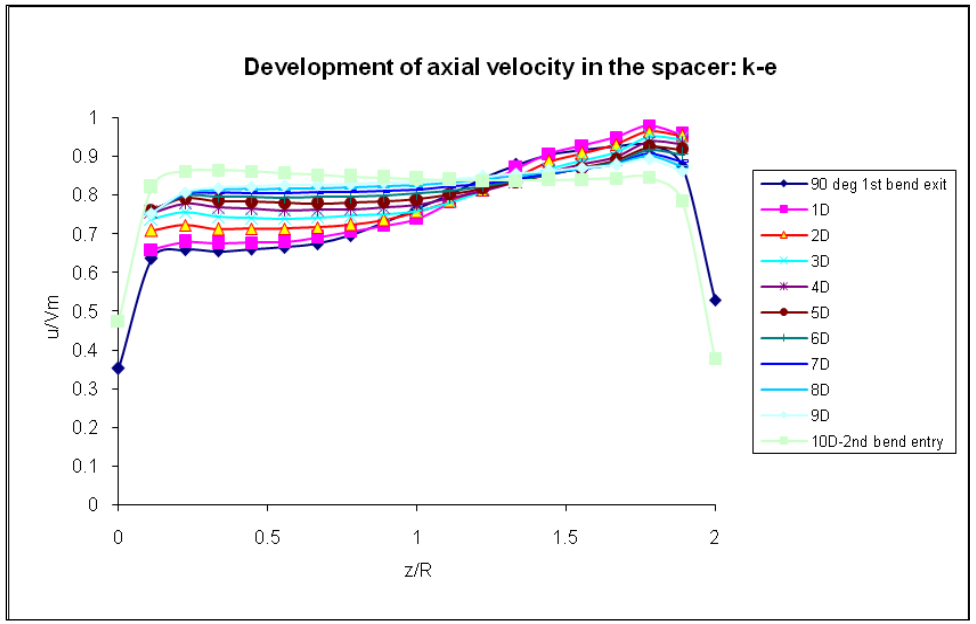

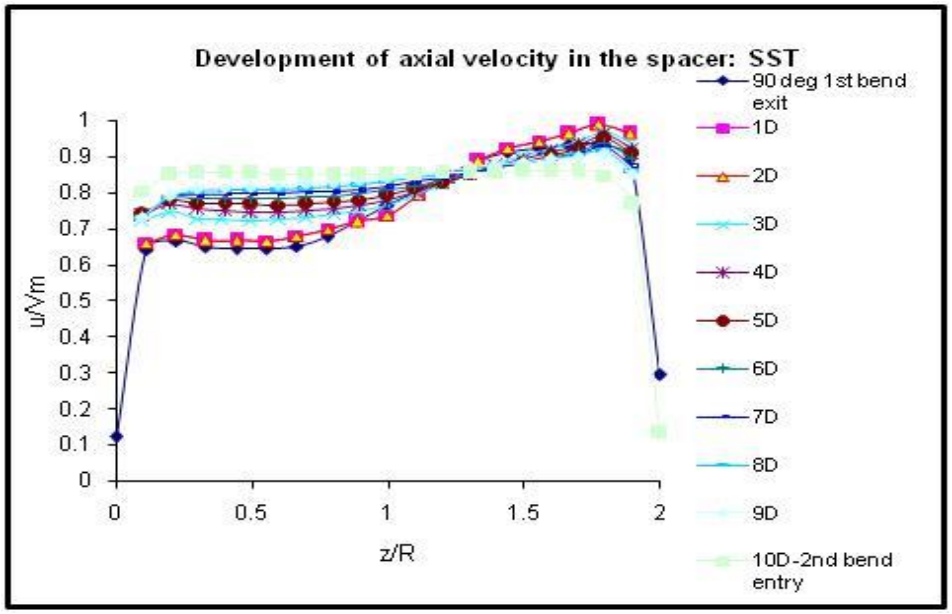

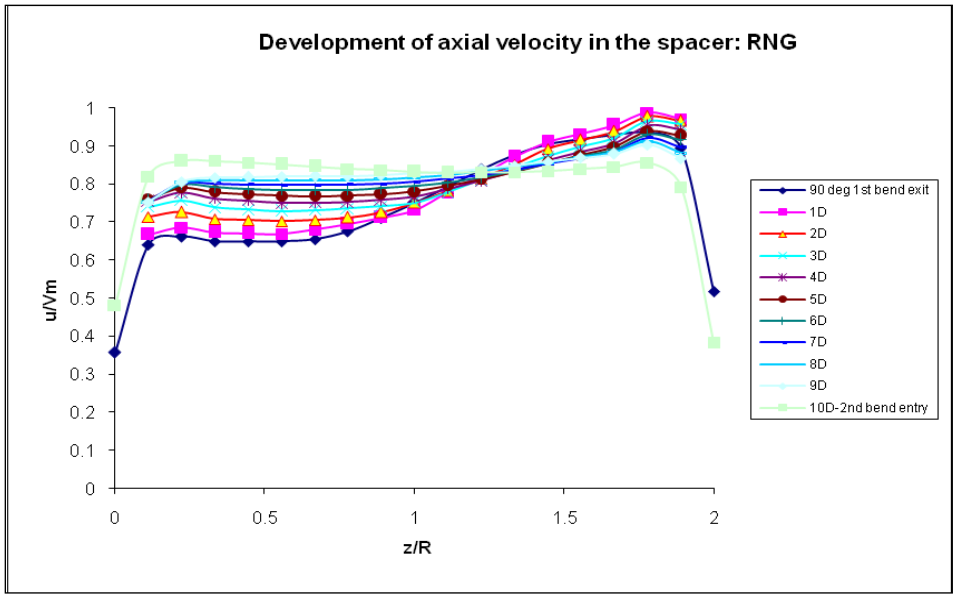

Figure 4.6: Velocity profiles on symmetry plane for various turbulence models at Re = 5.8x10^{5}and r/d = 3

4.2.4 Validation of the SST model using a single bend loss coefficient

The final validation of the SST model is with respect to its ability to predict the loss coefficient values of a single bend as reported in the literature. This validation will also help in deciding on the method of computing the head loss coefficient that will be most accurate.

The CFD results in Table 4.3 were achieved through the modelling parameters in Table 4.1. Eq. 4.2 was used to find the loss coefficient when a total pressure drop is considered together with a Blasius friction factor (f = 0.316/Re$^{0.25}$) for smooth pipes. The Blasius friction factor was used because the investigation was for the loss coefficient of smooth bends and pipes. Eq 4.2 was used to find the loss coefficient of the single 90^0 bend.

$$K = \left[\left(\frac{2g}{\mathrm{v}^2}\right)\left(\frac{\Delta P_{total}}{\rho g}\right)\right] - \left[f\,\frac{(L_u + L_d)}{d}\right] \qquad \textbf{4.2}$$

Turian *et al* (1997:248) presents an empirical correlation developed by Ito (1960) for bends with long tangents as:

$$K = 0.00241\alpha\theta\,\mathrm{Re}^{0.17}(2r_c/d)^{0.84} \quad \text{for Re } (d/2r_c)^2 \rangle 91 \qquad \textbf{4.3}$$

Where:

$$\theta = 90^0 : \alpha = 0.95 + 17.2(2r_c/\mathrm{d})^{-1.96} \text{ for } (2r_c/d) \langle 19.7$$

The value of the CFD loss coefficient was compared to Ito's (1960) empirical correlation (Eq. 4.3). It was also compared to the values from the ASHRAE Handbook (see Table 4.2). The comparison of the three results is provided in Table 4.4.

Table 4.2: ASHRAE loss coefficient for smooth bends, Crowe *et al* (2005:391)

r_c/d	K
1	0.35
2	0.19
4	0.16
6	0.21

Table 4.3: CFD results of a r/d = 3 smooth single bend

ΔP		K
inlet (Pa)	**outlet (Pa)**	**CFD-SST model**
442.960	7.361	0.184

Table 4.4: Comparison of a loss coefficient of a r/d = 3 smooth single bend

ASHRAE-Table 4.3,smooth pipes bends	**CFD-SST model**	**Ito Eq 4.3**
0.175	0.184	0.213

4.3 Findings

The loss coefficient calculated by CFD falls within the range of the empirically determined loss coefficient. Using the models and parameters as indicated above, the CFD analysis was concluded.

4.3.1 Determination of the head loss coefficient of closely spaced pipe bends (bend-spacer-bend)

4.3.1.1 Effects of the spacing ratio, K vs. L/d

The CFD analysis showed that the head loss coefficient of closely spaced pipe bends has a linear relationship with the spacing distance between the bends for various curvature ratios and Reynolds numbers (Fig. 4.8 and Fig 4.9). It increases as the spacer length between the pipe bends is increased. The results are consistent with Modi & Jayant (2004:328) who found that the loss coefficient increases with increased distance between bends. The recovery length assists the velocity profile to develop more fully and that increases pressure drop across the second bend and therefore the head loss coefficient. There appears to be mutual interaction of the flow the bends that is caused by proximity. It means that there should a single head loss coefficient for the closely spaced pipe bends. Miller (1990) found that if the distance between the bends becomes long enough, the head loss coefficient of the bends does not change. This indicates that there is no mutual interaction of the flow through the bends.

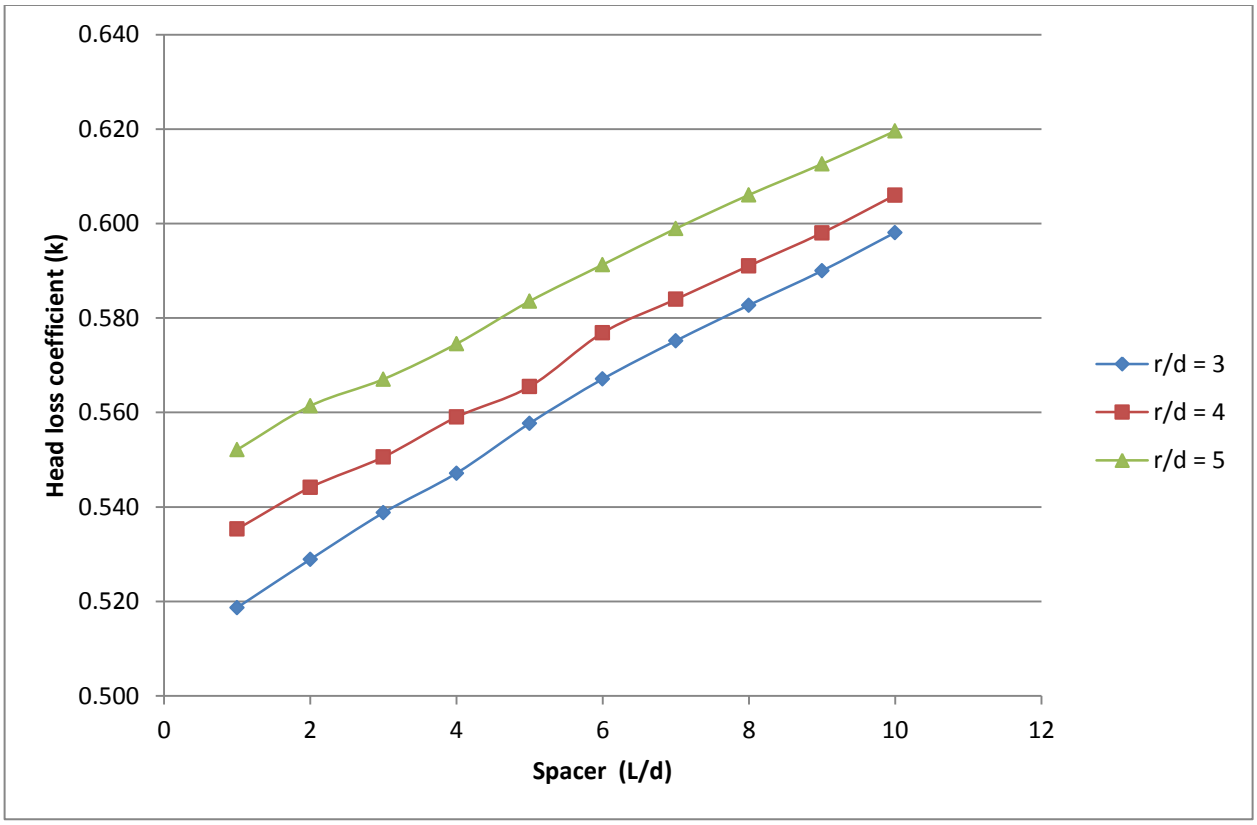

Figure 4.7: Head loss coefficient of closely spaced 90^0 bends at 180^0 configuration, Re = $7.3x10^4$

Therefore, flow between pipe bends a distance less than 160D does not have normal fully developed turbulent velocity profile (Ito, 1987:548), causing flow interaction. The CFD analysis allows calculation of the head loss coefficient that quantifies that interaction for design of piping system.

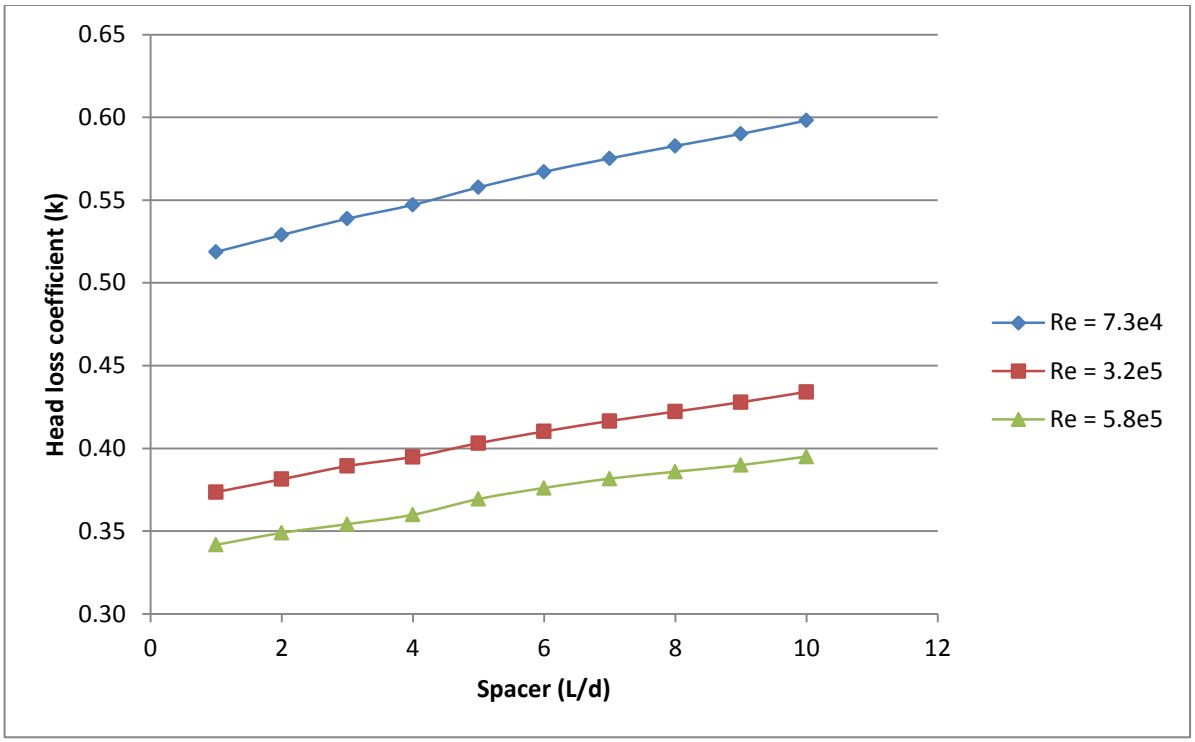

Figure 4.8a: Head loss coefficient at various Reynolds numbers at a constant curvature ratio, r/d = 3

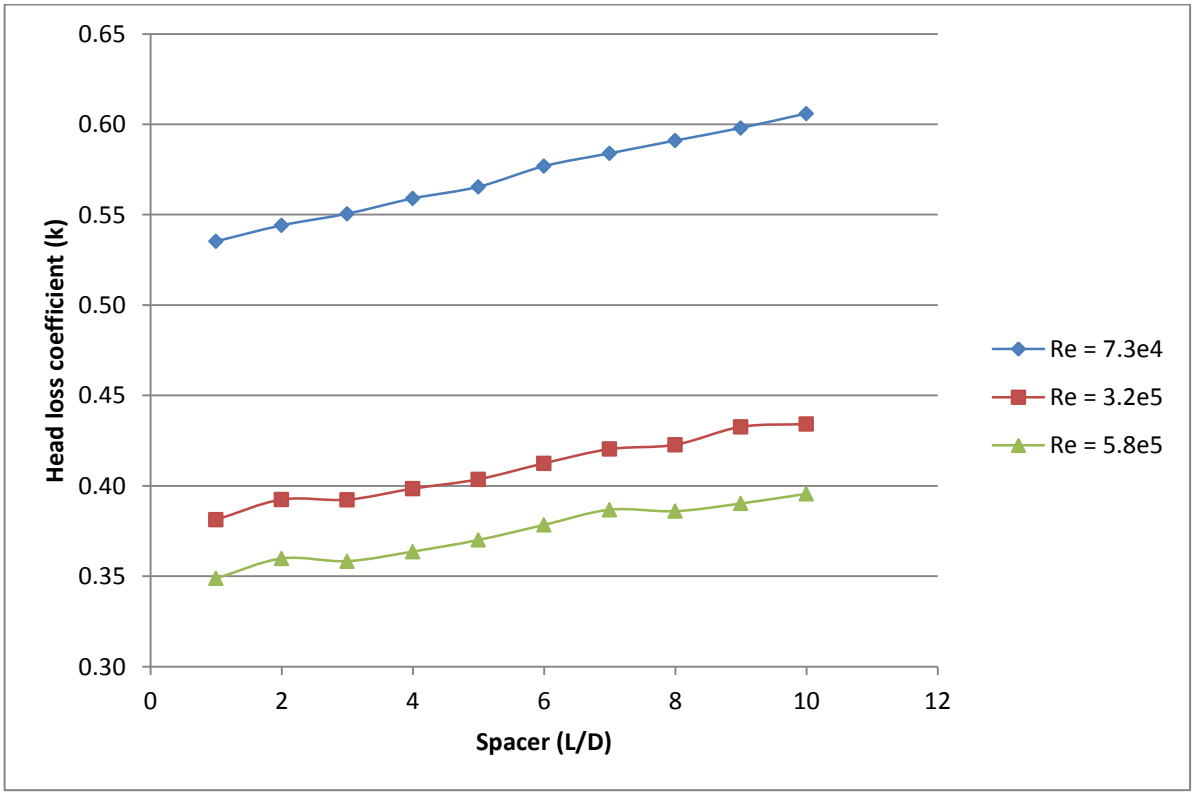

Figure 4.8a: Head loss coefficient at various Reynolds numbers at a constant curvature ratio, r/d = 4

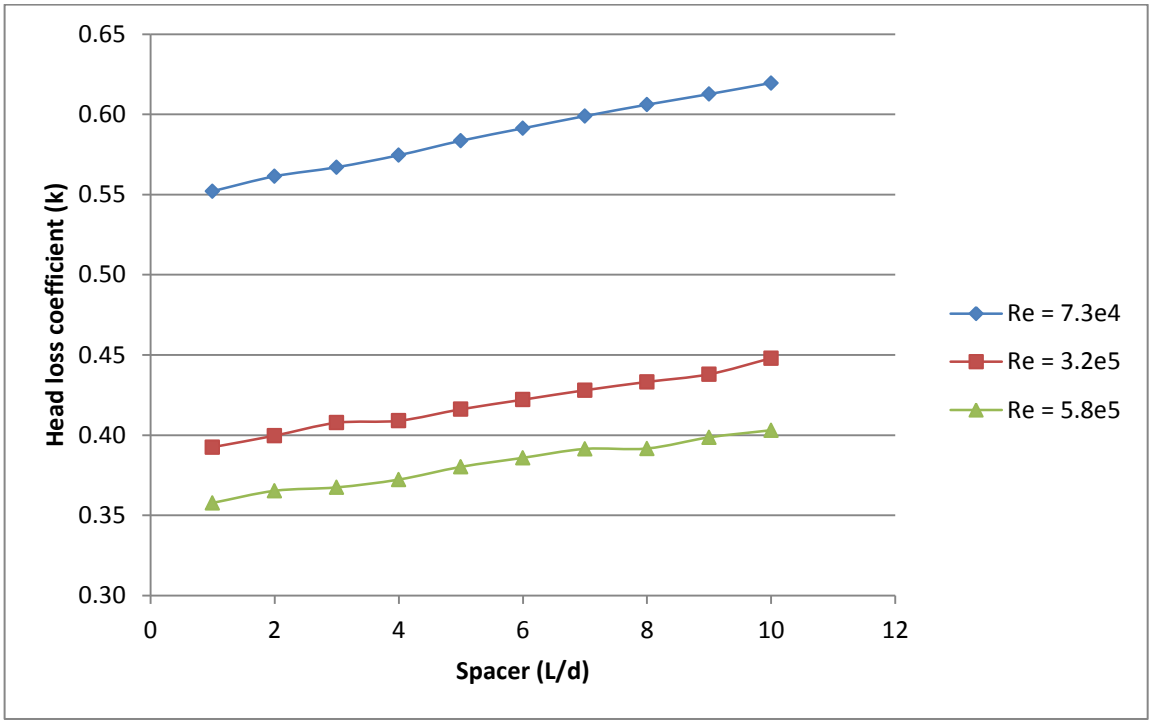

Figure 4.8: Head loss coefficient at various Reynolds numbers at a constant curvature ratio, r/d = 5

Flow development that is based on the spacing distance between the bends is indicated in Fig. 4.10. The velocity profile of a turbulent fluid is seen from Fig. 4.9 in its normal $1/7^{th}$ power law profile at entry to the first bend. Axial profiles inside the 90^0 bend show the distortion of the flow where the fluid on the outside of the bend flows at higher velocity than at the inside of the bend.

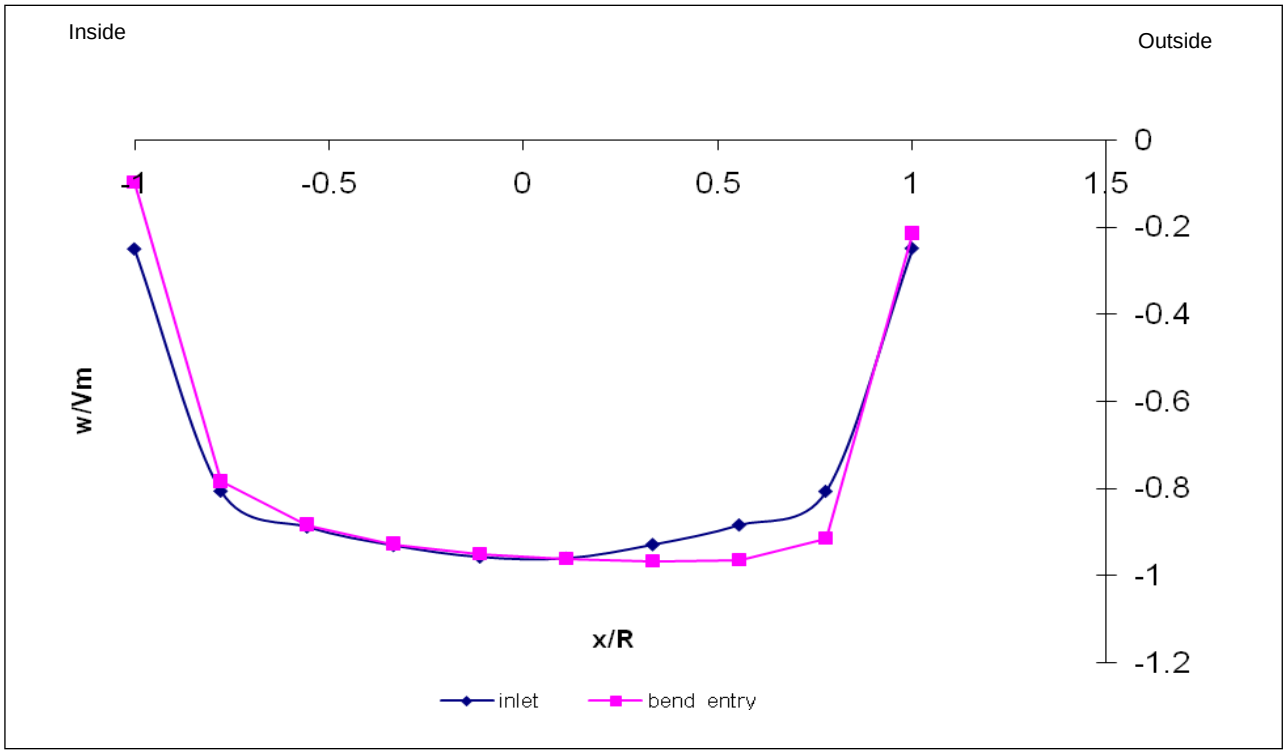

Figure 4.9: Velocity profiles on the symmetry plane at Re = 5.8x10^5, r/d = 3 at the inlet of the upstream tangent pipe

Figure 4.10 indicates this flow movement and its redevelopment as it goes through the spacer that is located between the bends. It is noticeable that on the inside surface of the spacer at 1D downstream of the upstream bend that there is no sign of the presence of flow, which can be interpreted as the start of flow separation. It continues until 10D where the flow begins to take up an almost a flat shape which indicates that it is progressing to a fully developed profile.

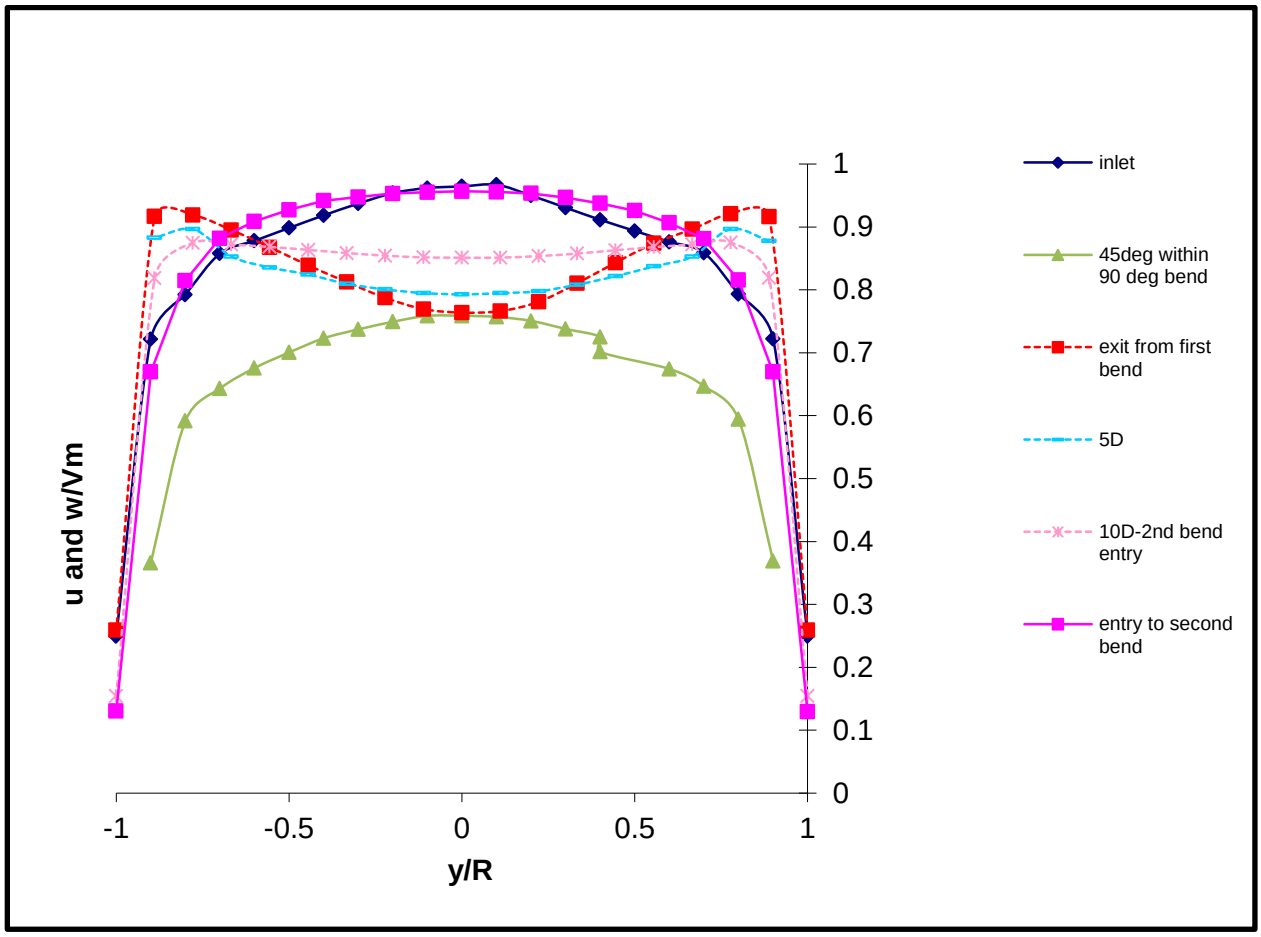

Figure 4.10: Velocity profiles in the x and z direction of the symmetry plane at Re = 5.8×10^5, r/d = 3

4.3.1.2 Effects of the Reynolds number, K vs. Re

Figure 4.11 indicates that at low Reynolds numbers the loss coefficient of closely spaced pipe bends is more than at high Reynolds numbers (as also can be seen on Fig 4.8). Higher energy wakes eddies are formed at higher Reynolds numbers than at lower Reynolds numbers. It is expected for the loss coefficient to be lower at higher Reynolds numbers because it is inversely related as Eq.4.3 suggests. It is because at higher Reynolds numbers the fluid within the bend separates from the surface with larger eddies (vortices). Thus, more mechanical energy is dissipated in the straight pipe, which leads to large relative pressure losses compared to the loss in the bend.

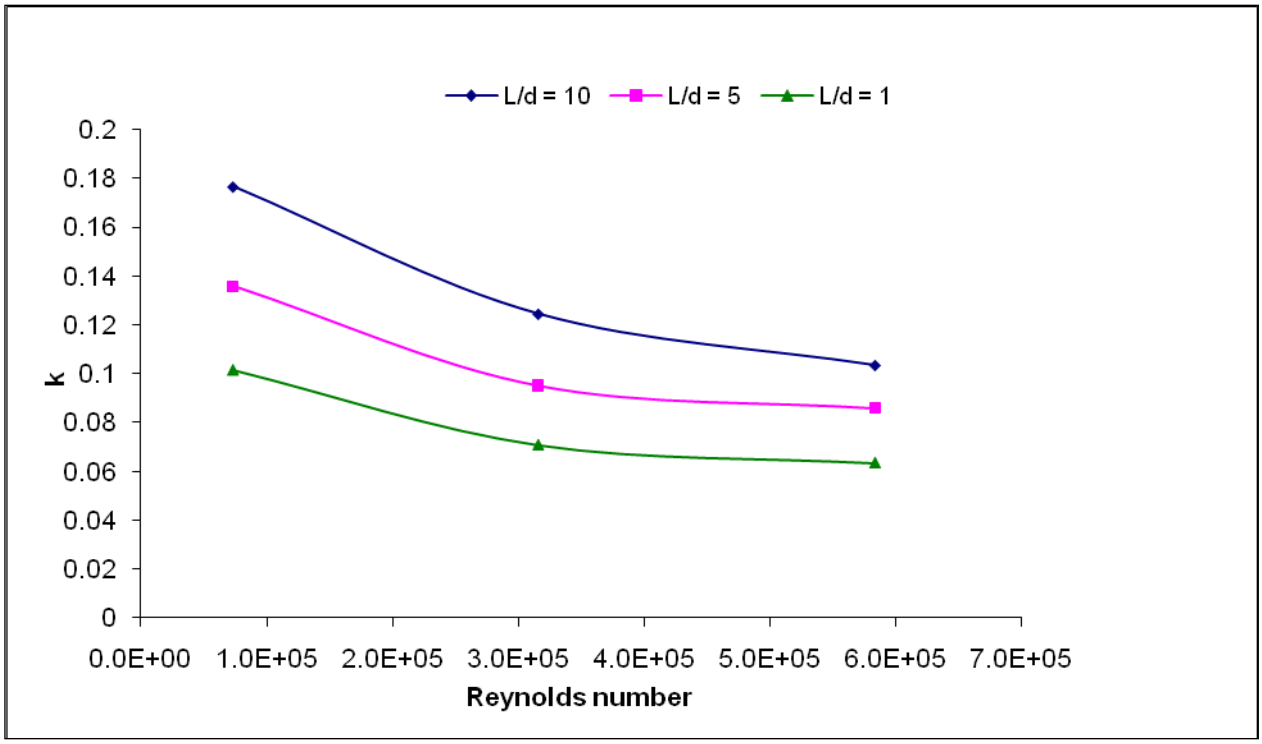

Figure 4.11: Overall loss coefficient of various spacer lengths at r/d = 3

4.3.1.2.1 CFD plots

The plots that follow present the pressure distribution, streamlines and velocity vectors within the bend-spacer-bend. They aim to aid understanding and outline the behaviour and effects of fluid in the system.

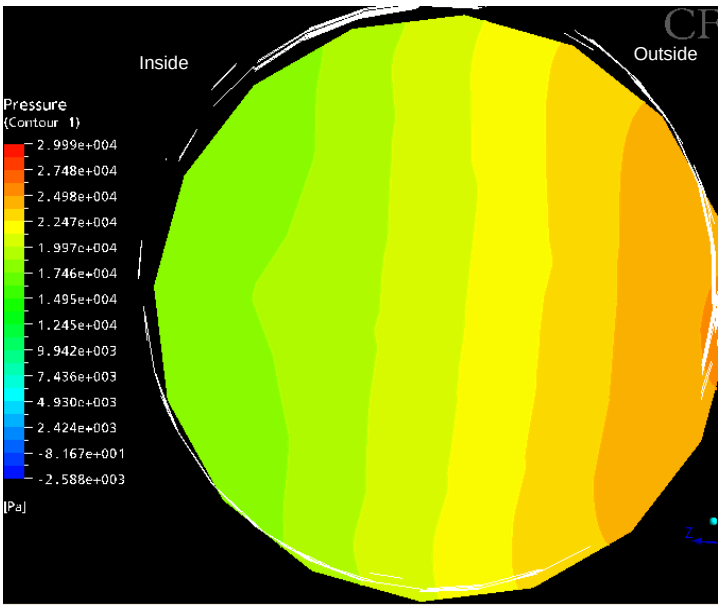

Figure 4.12a: Pressure distribution at exit of the first bend, Re = 7.3x10^4 at L/d = 10

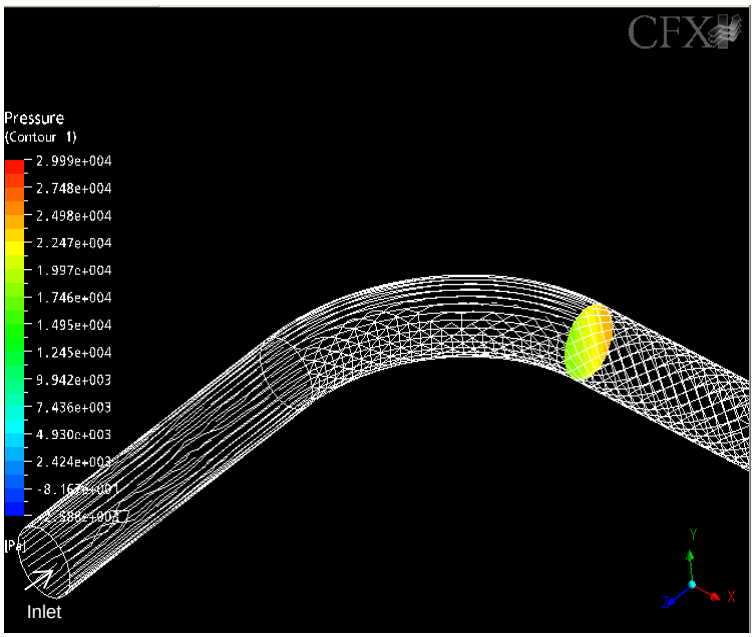

Figure 4.12b: Pressure distribution at exit of the first bend at Re = 7.3x10^4 for L/d = 10 spacer

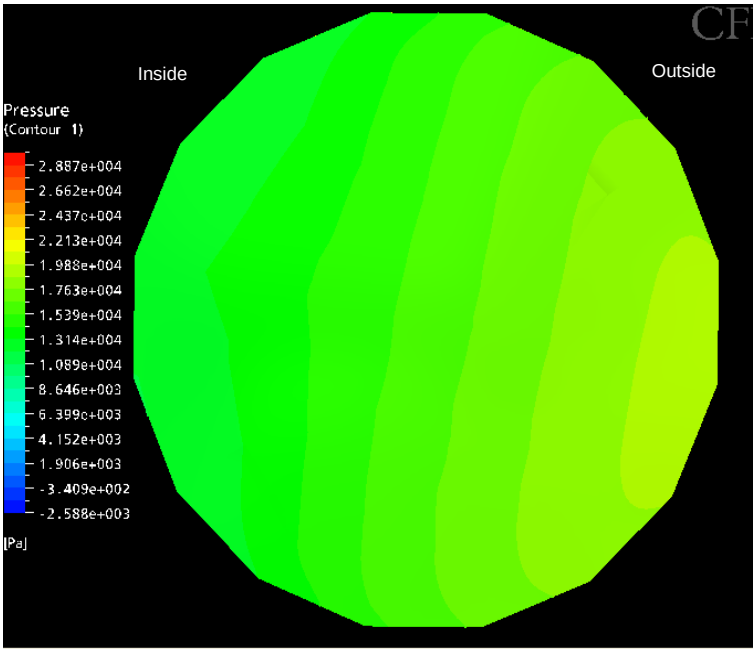

Figure 4.12c: Pressure distribution at entrance to the second bend, Re = 7.3x10^4

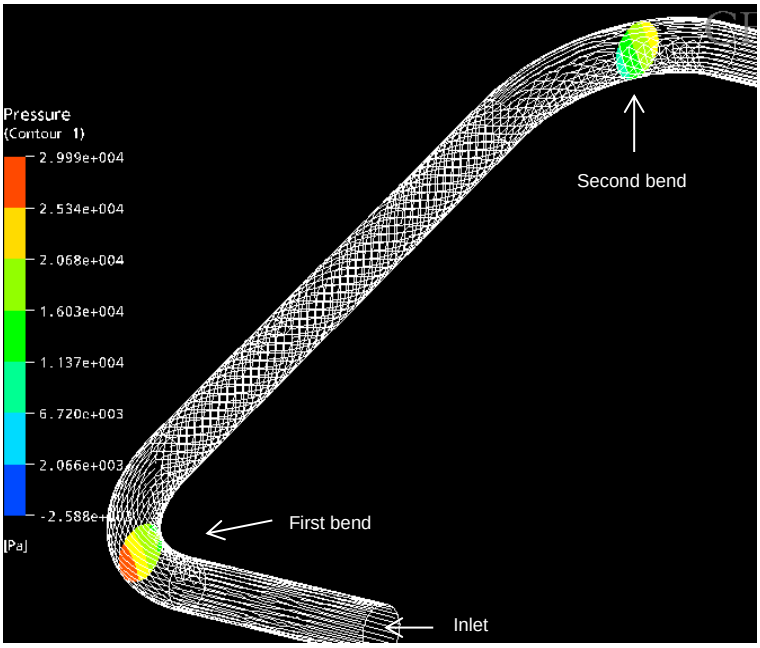

Figure 4.12d: Pressure distribution at 45^0 planes inside both bends, Re = 7.3x10^4

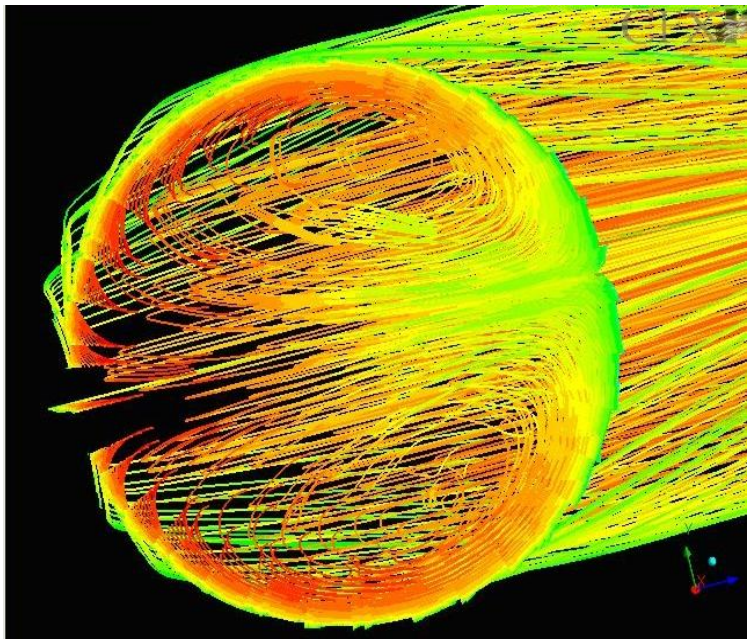

Figure 4.12e: Dean Type secondary flows, 2D downstream from the first bend

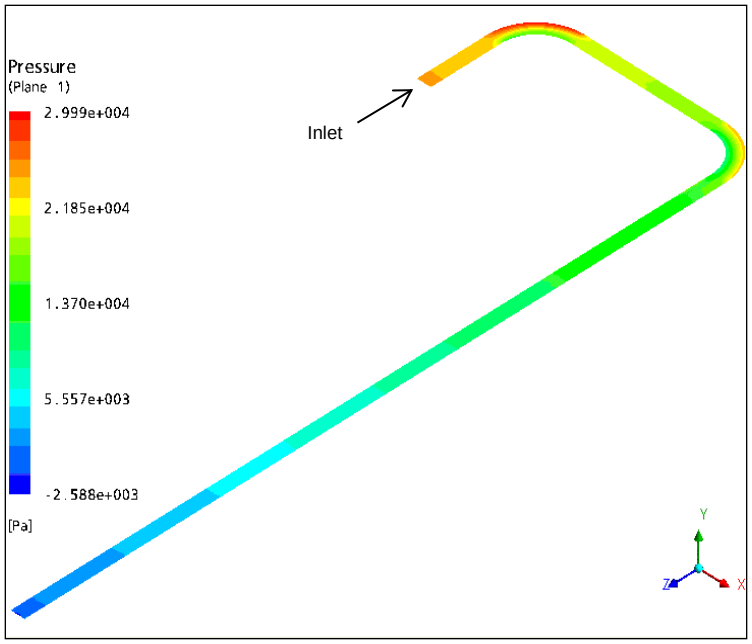

Figure 4.12f: Pressure distribution on the symmetry plane, Re = 5.8x105

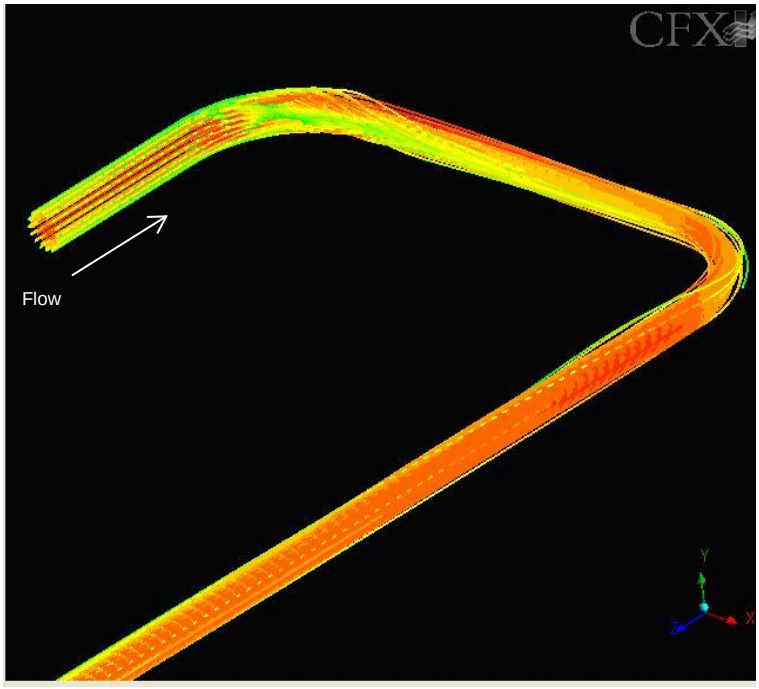

Figure 4.12g: Streamlines of the fluid, Re = 7.3×10^4

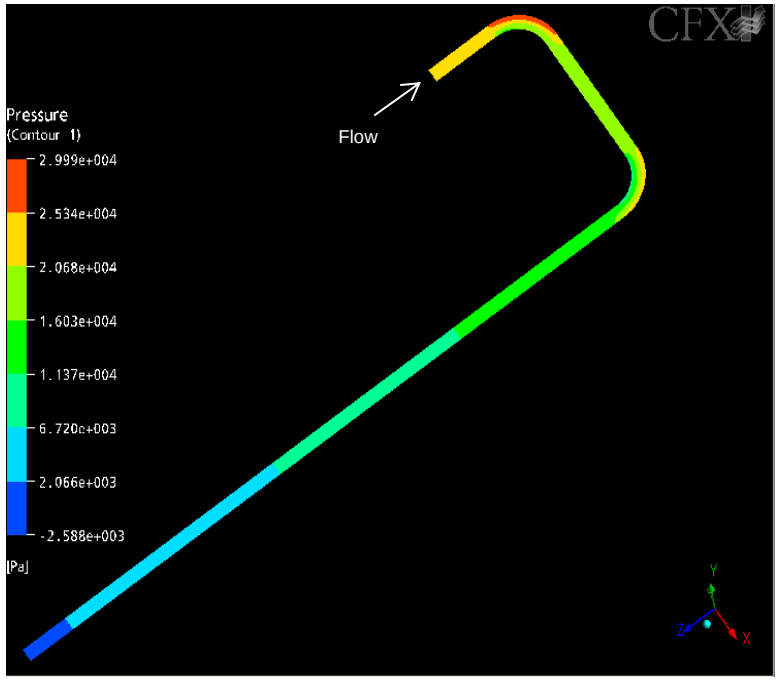

Figure 4.12h: Pressure distribution on the symmetry plane, Re = 7.3×10^4

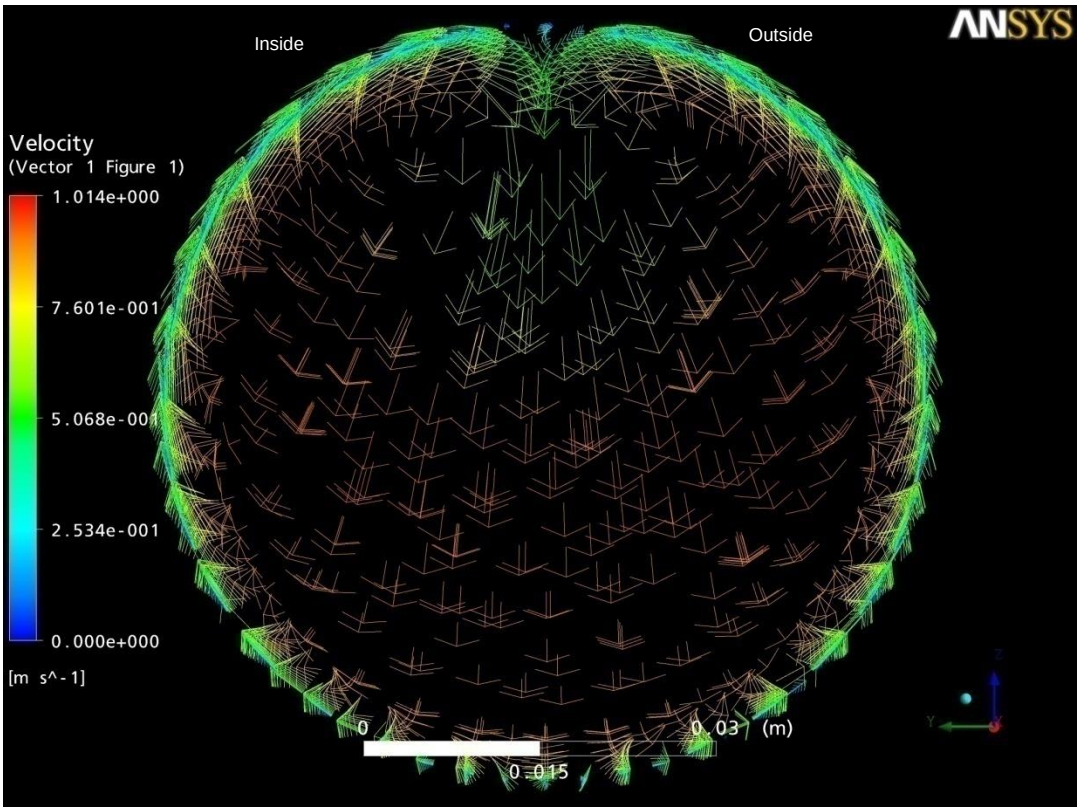

Figure 4.12i: Vector representation of the secondary flow 2D downstream the first bend

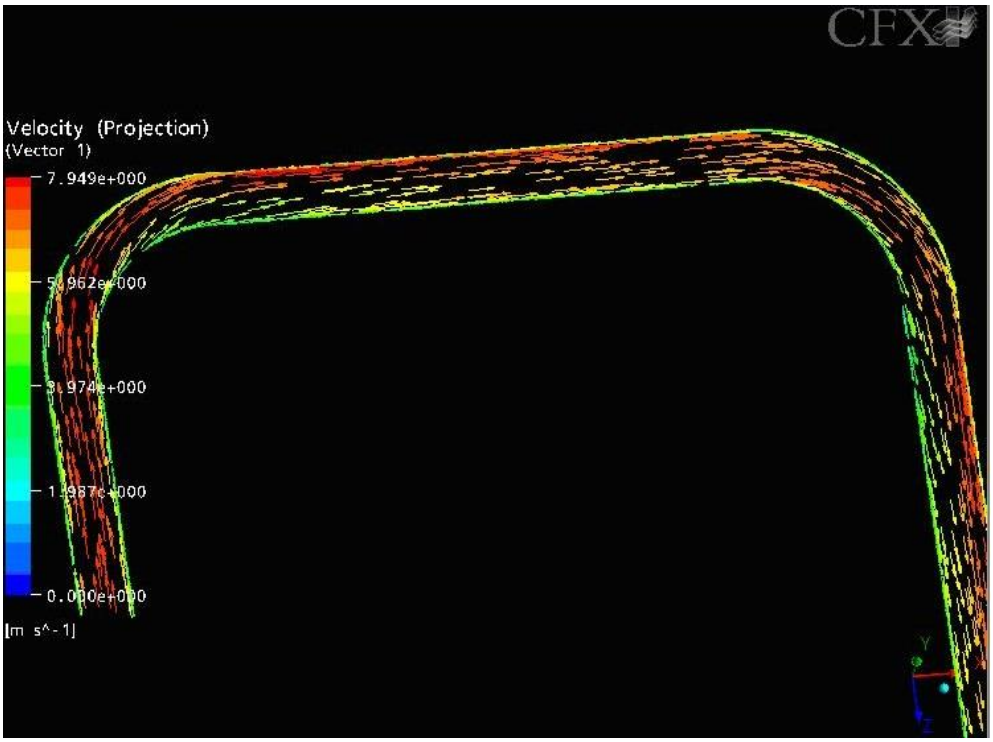

Figure 4.12j: Vector distribution on the symmetry plane, Re = 5.8x10^5

The dynamic pressure distributed inside the bend is depicted in Fig. 4.12a, b and c. The plane at the exit of Fig. 4.12a indicates the sections where the pressure varies across the bend. It is seen that the pressure is lower on the inside and higher on the outside of the bend. The variation simply confirms that the streamlines in bends are curved and centrifugal forces cause a pressure increase near the outer wall of the bend; and a pressure decrease on the inside of the bend.

It is noticeable from Fig. 4.12c, that the variation in pressure level at the entry of the second bend (length L/d = 10 from the first bend exit) is much less than at the exit from the first bend. This is owing to the distorted fluid beginning at the redevelopment stage when the outside of bend still experiences the effects of the centrifugal forces. Hence, the fluid is forced to separate from the inner wall due to the curvature of the bend. The streamlines of the flow are indicated in Fig. 4.12e demonstrate the bending effect of an internal flow. The phenomenon of the interaction between the centrifugal force and the slow motion of fluid in the boundary layer that induce secondary flows is known as the Dean-type secondary flows.

The effects of turbulent flow are further demonstrated through Fig. 4.12i, where a spacer length of L/d = 10 was used to show velocity vectors which translate to varying Reynolds numbers at a cross section plane that is 2D downstream from the second bend. It is seen from Fig. 4.12h that the pressure distribution on the symmetry plane indicates that at a higher Reynolds number (Fig 4.12f) the variation in pressure within the spacer is more than at a lower Reynolds number. It is as expected because the high speed moving fluid leaves the first bend much more distorted and its re-development would require extra spacing length than at lower Reynolds numbers. The head loss coefficient of closely spaced bends is lower at higher Reynolds number than at low Reynolds number despite the pressure within the spacer being higher.

4.4 Choosing a correlation

The dimensionless groups (Table A1) that are functions of the head loss coefficient of closely spaced pipe bends and the friction factor were presented in form of an equation. Then correlations were developed based on the Blasius type correlation which is of a power-law type. The first step in choosing the type of a correlation was to plot the data of the various variables on a log-log scale. The plots, therefore, formed straight lines which indicated that the choice of a power-law type correlation was appropriate.

The CFD friction factors for the straight pipe section for a smooth pipe at D = 0.065m and L= 3.25m (L/d = 50) downstream the second bend were computed from Eq 4. 4

$$f_{CFD} = \frac{\Delta p \pi^2 D^5}{8 L \rho Q^2} \qquad \textbf{4.4}$$

Table 4.5: CFD simulation of the friction factors at d = 0.065m and L= 3.25m (L/d = 50) downstream the second bend

P1 (Pa)	P2 (Pa)	Δ P (Pa)	Q (m^3/s)	f_{CFD}
348.107	7.844	340.263	0.003	0.014
4848.050	146.368	4701.682	0.014	0.010
15413.600	497.835	14915.765	0.027	0.009

$$k = C\left(L/d\right)^a \left(\mathrm{Re}\right)^b \left(r_c/d\right)^d \qquad \textbf{4.5}$$

Where:

a, b, d = fractional exponents

C = constant of generic shape

4.4.1 Friction factor and the head loss coefficient correlation

E.q 4.5 was linearized by a logarithmic transformation in to order to perform a least-squares regression. A linear regression analysis was then applied using a MS Excel (see Appendix A2) to find the constants *a,b, C,d*, in the resulting linear equation.

Table 4.5: Comparison of the friction factors at d = 0.065m and L= 3.25m (L/d = 50) downstream the second bend

P1 (Pa)	P2 (Pa)	Q (m^3/s)	*f*-CFD	*f*-Blasius	*f'*	*f'* vs. f-CFD	*f'* vs. f-Blasius
348.1070	7.8444	0.0033	0.0137	0.0192	0.0131	3.97%	31.81%
4848.0500	146.3680	0.0144	0.0101	0.0133	0.0099	1.33%	25.55%
15413.6000	497.8350	0.0265	0.0094	0.0114	0.0088	5.56%	22.75%

The friction factor correlation for the smooth pipe based on the CFD data is represented with Eq.4.4. Its deviation from the Blasius equation is high but decreasing with increasing Reynolds

number. However, its error from the CFD friction factor (from Darcy's equation) is lower see Table 4.5 and Fig 4.13.

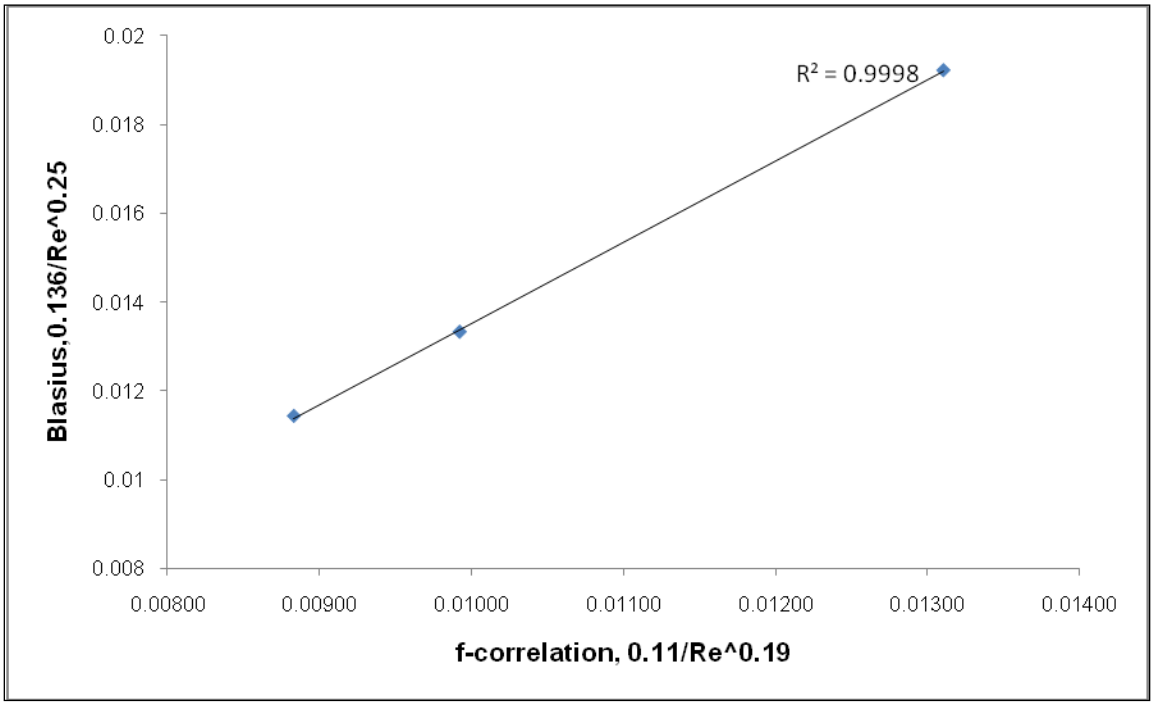

Figure 4.13: Blasius friction factor vs. the CFD friction factor found from the correlation

The head loss coefficient correlation of closely spaced pipe bends is represented by Eq.4.6.

$$\therefore k' = 4.8\frac{{}^{L}/_{d}{}^{0.06}\,{}^{r}/_{d}{}^{0.07}}{Re^{0.21}} \qquad \textbf{4.6}$$

This is valid for smooth pipes under the following conditions:

$$\mathbf{1 \leq {}^{L}/_{d} \leq 10;\ \ 7.3x10^{4} \leq Re \leq 5.84x10^{5}\ \&\ 3 \leq {}^{r_c}/_{d} \leq 5}$$

The correlation was based on the data presented in Table A. 2. It is seen that the absolute error of the correlation is 1.9%. It is in a good agreement with the data. The same is further demonstrated in Fig. 4.14, where the regression value between the data and the correlation is about 97%.

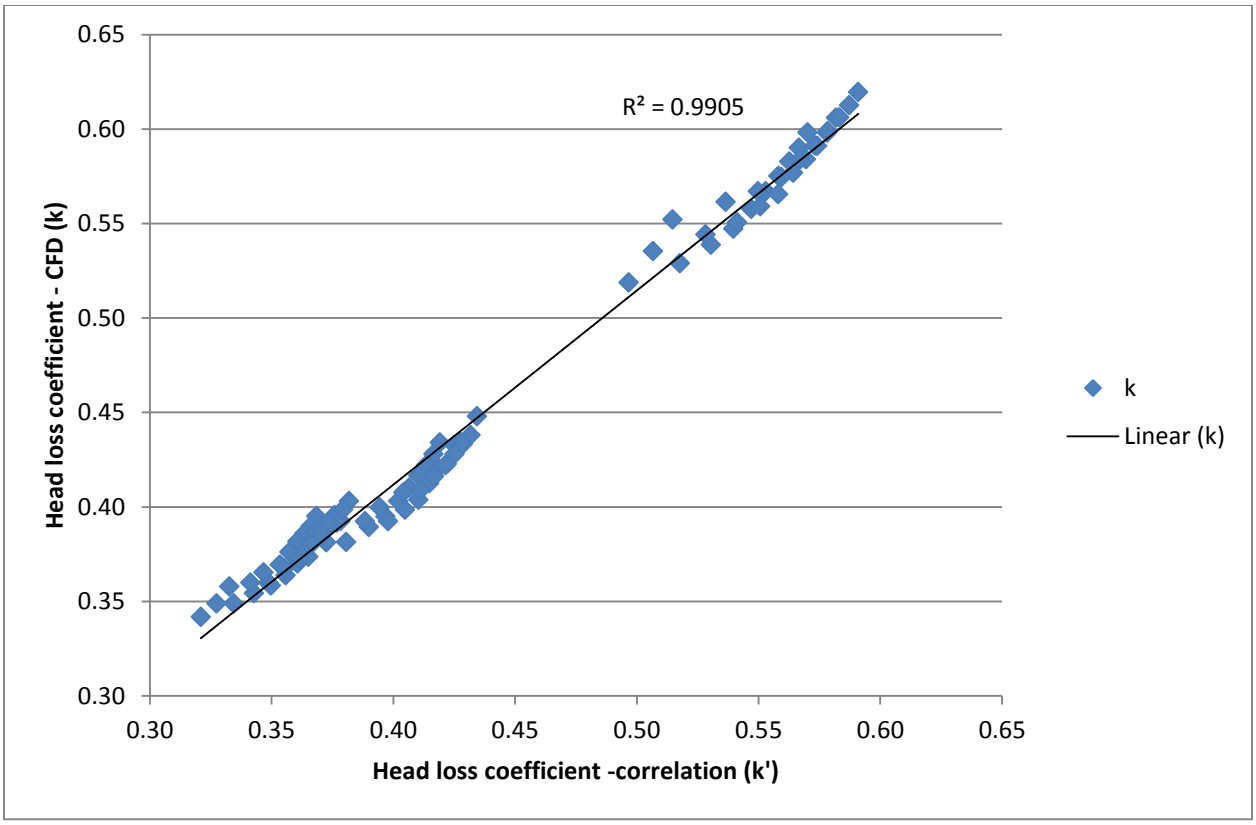

Figure 4.14: Comparison of the loss coefficients

CHAPTER 5

EXPERIMENTAL RESULTS

5.1 Overview of experiments

The aim of the experiments was to verify the numerical data (CFD). An experimental study to determine the head loss coefficient of closely spaced pipe bends was performed. Two long radius bends of a curvature ratio of $r_c/d = 3$ that were separated by a short (10D and 0D, relative to the recommended 100D for a fully developed flow) straight pipe were tested. Flow rates were varied and pressure data was recorded. The overall head loss coefficients of closely spaced pipe bends were calculated and presented through relevant graphical plots. The head loss coefficients of closely spaced pipe bends were compared to the literature values.

5.2 Experimental facility

Figure.5.1 represents a schematic diagram of the test rig that was used to determine the head loss coefficient of the closely spaced pipe bends. Water was used as a working fluid. It was supplied from the municipal water mains at a constant pressure of 450kPa. The entire rig was constructed using a 50mm UPVC pipe class 1 with an inside diameter of 46mm. Flow control came from throttling (opening and closing) a gate valve. Flow was measured using an ultrasonic flowmeter with its output obtained from the data logger (HOBO U12 Outdoor Industrial Data Logger with 4 External Channel Inputs) [(2)] see Fig 5.1 overleaf.

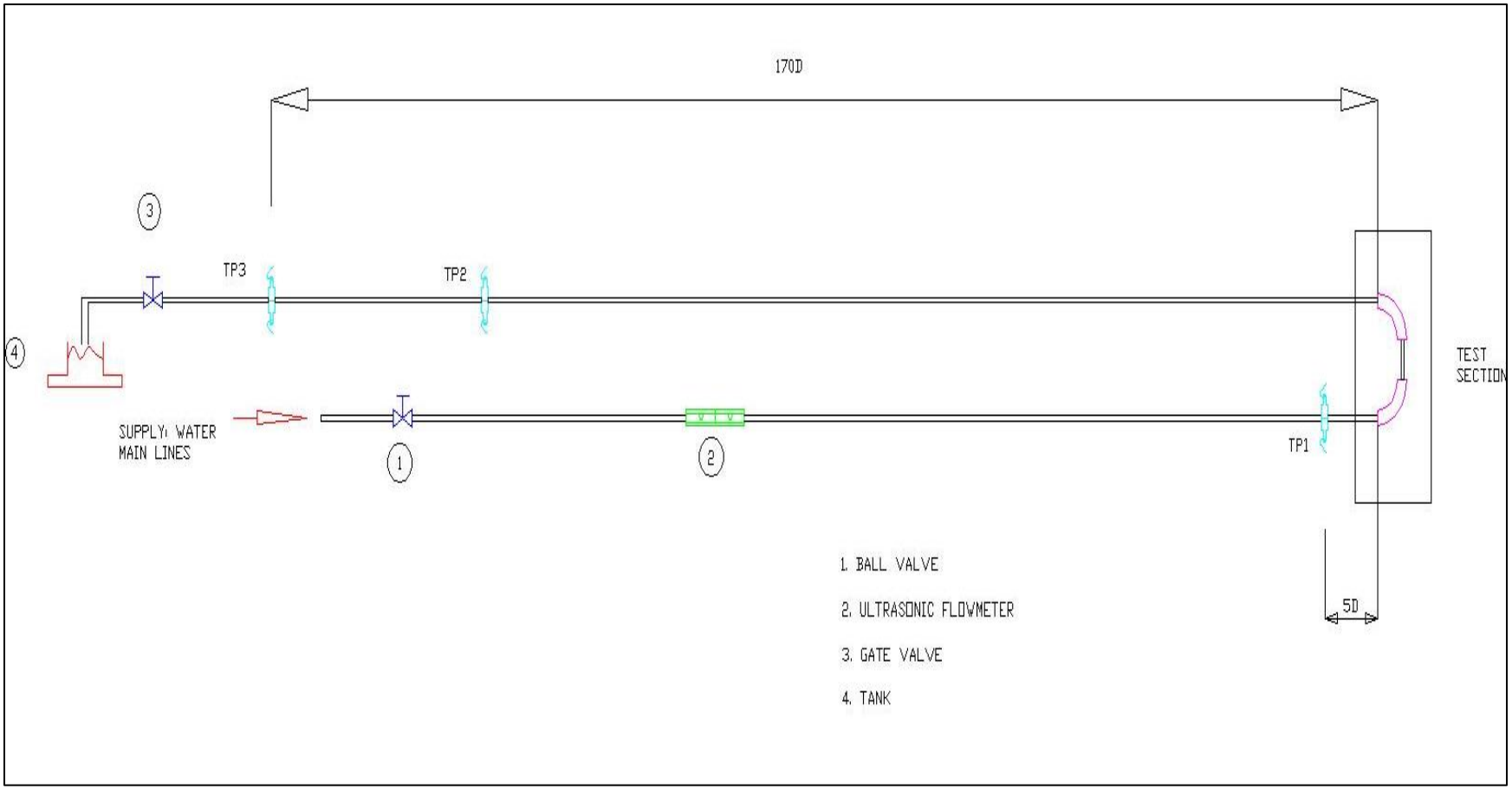

Figure 5.1: Schematic view of the test facility

The rig had three main sections which were the upstream section; the test section and the downstream section. The upstream section was supplied with water from the municipal water mains. A ball valve [(1)] was used to control the supply into the system. A maximum Reynolds number of 1.12×10^5 was obtainable from the mains pressure at a velocity of 2.5 m/s. The flow variance was from throttling (varying the flow area through the pipe) the gate valve downstream.

In total the pipe length for the upstream pipes and the fittings was 24m. A straight pipe of 6m was needed after the last disturbance generated by a reducer (upstream of the first test bend), in order to ensure that the flow was fully developed before the test section. At 50D upstream of the first bend, two pressure transducers were installed at 180^0 (opposite sided of the pipe) to have a differential reading a single point (PT1). The pressure transducer was non-linearity of ±0.5%; were installed to measure the absolute pressure upstream and downstream of the test section. All taps were 2mm inside diameter (ID) which were deburred as confirmed by visual examination.

The test section consisted of two 90^0 long constant radius bends that were connected by a short straight pipe (spacer) between them. In the test section bends having a curvature ratio $r_c/d = 3$ were fixed and two spacers with the lengths of 10D and 0D, respectively, were interchanged to investigate their influence on the head loss coefficient. The downstream section had two pressure points placed at 217D and 304D spacing from the last bend to ensure that the flow was fully developed and for computing the friction factor of the pipes. The downstream section had a total length of 18m (348D), which was enough for the flow to be fully developed and to allow for any flow separation effects to diminish to negligible levels. Mukhtar *et al* (1994:330) found that in order to ensure a fully developed flow the pipe length must be at least 150D. The water temperature was municipal supply at a temperature that remained practically constant at 20^0C for the duration of the experiments.

5.3 Experimental uncertainty analysis

It is known that scientific experiments usually have uncertainties from the acquired data and it was necessary that all contributing measurements to the results be error analysed. This was done to determine the potential effects of errors associated with all the measured quantities. These errors were anticipated and analysed because they had an effect on the desired values (loss coefficient-values). It was appreciated that measurements usually have a percentage error. Therefore, it is

necessary to ensure that experimenting time and the resources be spent productively by evaluating and limiting probable errors (Coleman & Steele, 2009:4).

The approach was to compute an uncertainty estimate that was to indicate a percentage of confidence within which the true value would fall (Coleman & Steele, 2009:14). The following paragraphs explain the steps that were taken in analysing errors and in identifying error sources.

In this analysis the error sources were first identified. These sources were potentially from the possible standards used; and the imperfect calibrating methods. However, the calibration certificates that were issued from the newly bought instruments were an acceptable measure in the accuracy of the instruments. The experiments had parameters which had repeatable measurements, e.g., pressure and flow. Then the parameters that were measured only once were the inside pipe diameter and pipe lengths (spacer length; upstream and downstream flow development lengths).

The errors found in this study, as many other experimental studies would have, were categorised in two forms, namely, systematic and random errors (White, 2008:46). The systematic error was thought of being the lack of applying precise calibrating methods of the instruments. The other type of error, the random error, was minimised through statistical methods of averaging scatter readings (moving averages and discarding points outside set limits).

The analysis began by determining the overall uncertainly level in the experiments viz., by finding the uncertainty in the pressure measurement. It then offered a confidence value for measuring the friction factor. Then, subsequently, a confidence level was determined for the loss coefficient of closely spaced pipe bends.

5.3.1 Mathematical error estimate in experiments (White, 2008:47):

The various independent variables of the friction factor and their uncertainty error estimates were identified and defined:

The uncertainty of the friction factor was given as

$$\delta P \approx \frac{\partial P}{\partial x}\delta x \quad \textbf{5.1}$$

The multiple variables of the friction factor were given as

$$f = f(d, \Delta P, Q, L) \quad \textbf{5.2}$$

Where:

d = inside diameter of the pipe (m)

∆P = pressure difference in the direction of flow (Pa)

Q = fluid flow rate (m^3/s)

L = length of the measured pipe (m)

The expression of the friction factor was found through a rearrangement of Eq. 3.4 to become:

$$f = \frac{\pi^2 \Delta P d^5}{8\rho Q^2 L} \quad \textbf{5.3}$$

The power-law exponent of the independent variables in Eq. 5.4 is presented as:

$$f = Const(d^5 \cdot \Delta P^1 \cdot Q^2 \cdot L^1 \cdot \rho^1) \quad \textbf{5.4}$$

The subsequent root-mean-square estimate of the uncertainties is given as:

$$\frac{\partial f}{f} = \left[\left(5\frac{\partial d}{d}\right)^2 + \left(1\frac{\partial \Delta P}{\Delta P}\right)^2 + \left(2\frac{\partial Q}{Q}\right)^2 + \left(1\frac{\partial L}{L}\right)^2 + \left(1\frac{\partial \rho}{\rho}\right)^2\right]^{1/2} \quad \textbf{5.5}$$

The errors associated with the aforementioned parameters are indicated in Table 5.1. Their estimated errors, which were used in computing the overall uncertainty of the experiments are rationalised as on the bases listed.

Table 5.1: Results of the error analysis

Uncertainties	Accuracy	Rationale
δd	0.3%	• There was a confidence level of 99.5% on the weighting scale's

		accuracy. • A gravimetric-volumetric calibration was performed. Where only the wetted volume of the pipe, i.e., the mass water inside, was considered. The mass of the hollow pipe was ignored by zeroing the scale before water could be poured in the pipe. • Measured against the computed. A ratio of diameter measured using a vernier calliper over the diameter determined through the balance of forces.
$\delta\Delta P$	0.5%	• The pressure transducer had an accuracy of ±0.5%. The practical set up of pressure gauge was followed through best practises. For instance, the radial hole on the pipe wall needed to be drilled perpendicular to the wall and the burrs were removed. The static pressure would have been affected and it would have had a resulting error leading to 1.1% if such was ignored.
δQ	0.5%	• Sudden losses in pressure due to the usage of large water mains in the district.
δL	0.1%	• The length of the pipe length would only have an error if the measuring tape itself had some unlikely calibration needs. The major concern was with regard to the flow developing lengths. The developing lengths were followed as per literature as those respective lengths were measured accordingly. The instruments were positioned adequately with reference of the test section for upstream and downstream pipes.
$\delta\rho$	1.2%	The temperature of water during the tests was kept constant at 20^0C. That the variance in water temperature would be at range 2^0C.

The overall uncertainty of the experiments was found to be $\partial f/f = 2.19\%$, resulting in a 97.8% confidence in the experimental data of the friction factor.

$$n \cdot (k') \cdot C_{1-2} = \frac{2\Delta P_{total}}{\rho v^2} - \frac{f}{d}(L_u + L_s + L_d) + f \cdot \frac{L_b}{d} \quad \textbf{5.6}$$

$$\frac{\partial k'}{k'} = \left[\left(1\frac{\partial d}{d}\right)^2 + \left(1\frac{\partial \Delta P}{\Delta P}\right)^2 + \left(1\frac{\partial f}{f}\right)^2 + \left(2\frac{\partial v}{v}\right)^2 + \left(1\frac{\partial L}{L}\right)^2 + \left(1\frac{\partial \rho}{\rho}\right)^2\right]^{1/2} \quad \textbf{5.7}$$

The overall uncertainty of the loss coefficient of closely spaced pipe bends was found to be $(\partial k')/k' = 2.49\%$, resulting in a 97.5% confidence.

5.4 Findings

5.4.1 Friction Factor

The head losses resulting from the flow of a fluid through a pipe are expressed by the Darcy formula (Eq. 5.2).

$$\Delta P = f \cdot \frac{L}{d} \frac{\rho v^2}{2} \qquad \textbf{5.8}$$

At high Reynolds number (complete turbulence, rough pipes) the friction factor can be obtained from the Colebrook-White (1937) equation

$$\frac{1}{\sqrt{f}} = -2log\left(\frac{\varepsilon}{3.7d} + \frac{2.51}{Re\sqrt{f}}\right) \qquad \textbf{5.9a}$$

$$1 = -2log\left(\frac{\varepsilon}{3.7d} + \frac{2.51}{Re\sqrt{f}}\right) \cdot \sqrt{f} \qquad \textbf{5.9b}$$

The procedure used to compute the friction factor was as follows:

- Two pressure tappings were set 4 m apart on a straight PVC pipe. The first tapping was placed 217D downstream of the second bend to ensure fully developed flow. The tappings were used to measure the pressure drop along the pipe at various Reynolds numbers.
- In order to ensure that the results were accurate, the pressure transducers (upstream and downstream) were positioned where the swirl had decayed and the flow was fully developed. The downstream pipe was 174D after the second bend. According to Mukhtar *et* al (1994:330), this pipe length was sufficient for a fully developed flow. Miller (1990:82) inferred that the swirl that is caused by a combination of bends could persist for more than 100D.
- The Reynolds numbers were varied by throttling a gate valve.

- The readings of the pressure differences were gathered and the Colebrook-White equation (Eq. 5.3) was used to find the friction factor. The Reynolds number which was computed from the flow rate data was inserted in Eq. 5.9a.
- An iterative method was used to solve Eq 5.3 for the friction factor. The friction factor on the Right-Hand-Side (RHS) of Eq 5.9b was iterated, while the other variables were kept constant, until the RHS came to a unit. When the RHS was equal to a unit but an accuracy of three decimals, the last iterative value was taken as the friction factor for that specific Reynolds number. The results are presented in Fig. 5.2. The iterative values of the friction factor are presented in Appendix B, Table B1.

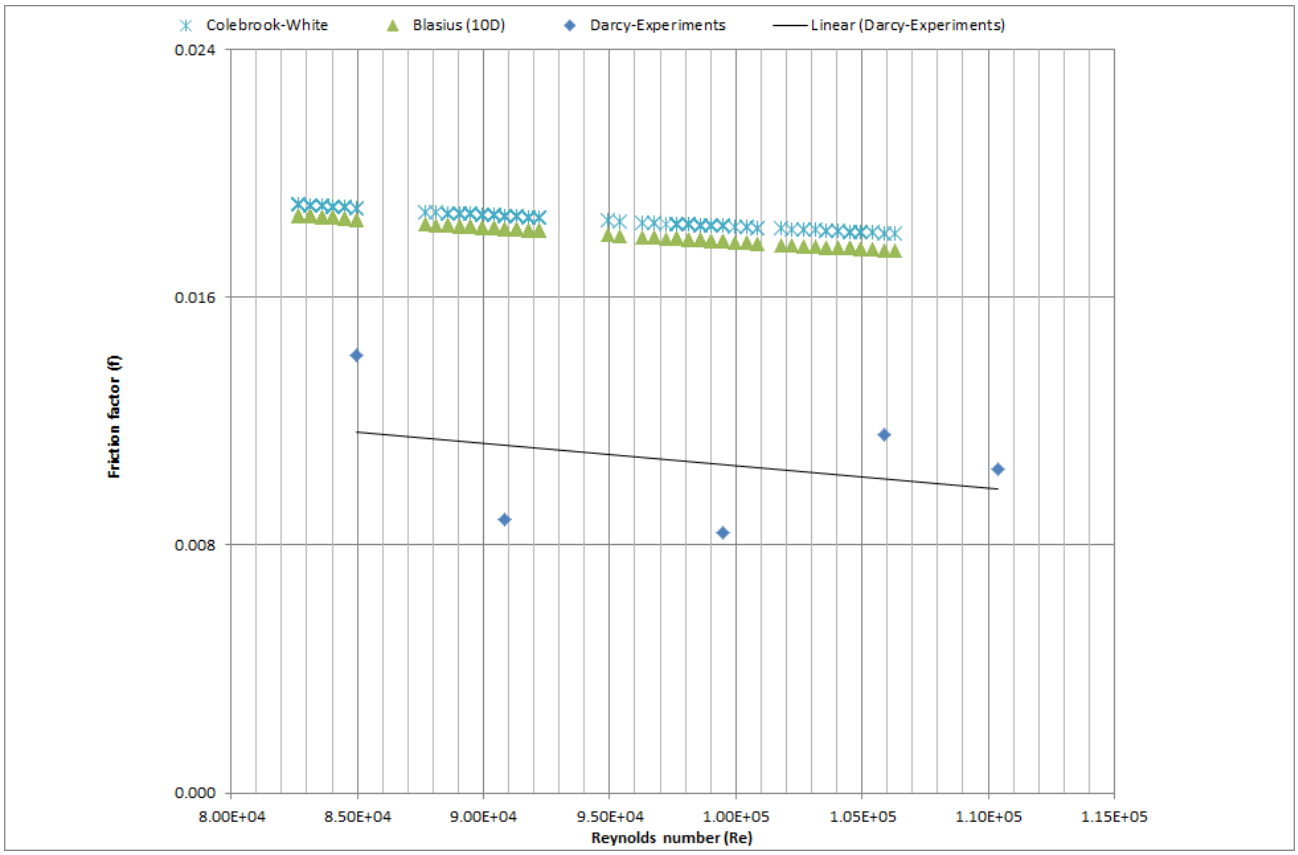

Figure 5.2: Comparison of the friction factor found through experiments against the Colebrook-White equation on the roughness of a PVC pipe

In this representation a Colebrook-White plot was compared to the experimental results, see Fig.5.3. Table B1 shows the data gathered from computing the friction factor of the pipe system.

5.4.3 The Head Loss Coefficient of closely spaced pipe bends

The formula used to compute a single head loss coefficient of closely spaced pipe bends was based on Eq.5.10a by Miller (1974). This equation is a combination of the head loss equations for straight pipe and bends. It was manipulated in order to find the head loss coefficient “k” as a variable of interest.

$$h_{tot} = f\,\frac{v^2}{2gd}\left(L_u + L_b + L_d + L_s\right) + K\,\frac{v^2}{2g}\left[C_{1-2}\right] \qquad \textbf{5.10a}$$

The principle of conservation of energy with an inclusion of a correction factor for closely spaced pipe bends, presents:

$$\Delta P_{bend}\cdot C_{1-2} = \left[\Delta P_{tot} - f\rho v^2\left(\frac{L_u + 2L_B + L_d}{d} + \frac{L_s}{d}\right)\right] + f\,\frac{L_B}{d}\cdot\frac{\rho v^2}{2} \qquad \textbf{5.10b}$$

In essence, the representation of the losses in Eq. 5.10b indicates that:

$$\Delta P_{bend} = \Delta P_{loss} + \Delta P_{bend,F} \qquad \textbf{5.10c}$$

Where:

$$\Delta P_{loss} = \Delta P_{tot} - \left(L_u + L_B + L_d + L_s\right)\frac{f}{d}\,\frac{\rho v^2}{2} \qquad \textbf{5.10d}$$

And

$$\Delta p_{bend,F} = L_B\,\frac{f}{d}\,\frac{\rho v^2}{2} \qquad \textbf{5.10e}$$

$$L_B = 2\pi\, r \big/ 4 \qquad \textbf{5.10f}$$

L_B = length of a bend

L_d = length downstream of the bends

L_u = length upstream of the bends

d = constant inside diameter of the pipeline

r_c = radius of the curvature

f = constant friction factor as a function of a Reynolds number and the relative roughness of the pipe

ΔP_{tot} = pressure difference upstream and downstream of the bends.

$C_{1\text{-}2}$ = correction factor of closely spaced pipe bends.

A loss coefficient of a bend was found by

$$K = \frac{\Delta P}{\frac{1}{2}\rho v^2} \qquad \textbf{5.10g}$$

$$K = \left[\frac{2\Delta P_{tot}}{\rho v^2} - f\left(\frac{L_u + 2L_B + L_d}{d} + \frac{L_s}{d} \right) \right] + f\,\frac{L_B}{d} \qquad \textbf{5.10h}$$

The combined loss coefficient for two closely spaced bends was regarded by Miller (1974) as the sum of single isolated bends, multiplied by a correction factor:

$$k_{Miller} = \left[k_1 + k_2 \right] \cdot C_{1-2} \qquad \textbf{5.10j}$$

Where:

k_1, k_2 = loss coefficient of isolated bends found through Ito's correlation, see Eq. 5.10k

Turian *et al* (1997:248) present an empirical correlation developed by Ito (1960) for bends with long straight pipes as:

$$k = 0.00241\alpha\theta \,\mathrm{Re}^{-0.17}(2r_C / d)^{0.84} \quad \text{for Re } (d/2r_C)^2 \rangle 91 \qquad \textbf{5.10k}$$

$$\theta = 90^0 : \alpha = 0.95 + 17.2(2r_C / d)^{-1.96} \text{ for } (2r_C / d) \langle 19.7 \qquad \textbf{5.10l}$$

Now:

$$k^* = k_{Miller}$$

Thus, the correction factor is:

$$C_{1-2} = \frac{k^*}{[k_1 + k_2]} \qquad \textbf{5.10m}$$

Table 5.2: Miller: r_c/d = 3 + spacer + r_c/d = 3, at Re = $1x10^6$

L/d	C*	k*
0	0.71	0.194
1	0.73	0.199
4	0.79	0.216
8	0.85	0.232

The trend in Fig. 5.3 shows a linear relationship between the loss coefficient and the spacer length to pipe diameter ratio, which indicates that with an increase in length between the bends, the severity of the losses of the bends increases (as found by Miller 1990). It had been predicted that with the increased length of the spacer, the loss coefficient will become constant. When this happens, the secondary flow generated by the first bend would have dissipated by the time the second bend is reached. At shorter separation lengths the bends will mutually interact, thus affecting the combined loss coefficient.

Miller's findings were based on a higher Reynolds number than that used in the experiments. The difference in the Reynolds numbers is significant because, when the Reynolds number is increased the losses due to the secondary flows induced in the bends change in comparison with the losses

associated with skin friction. Thus, at higher Reynolds numbers the loss coefficient reduces in magnitude and it would tend to behave as an isolated bend (single bend) because of the trend line becomes constant.

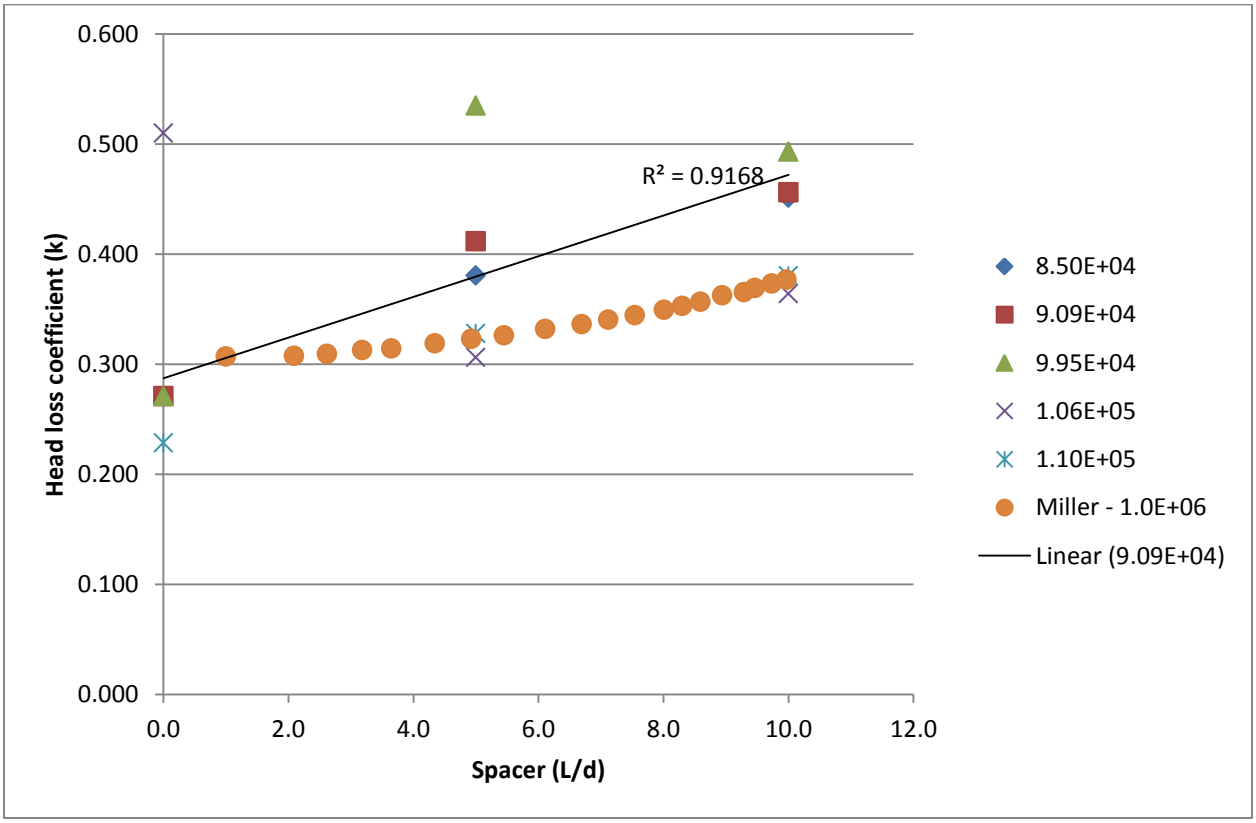

Figure 5.3: Loss coefficient vs. Spacing ratio contrasted

Nonetheless, it is encouraging to still have results that present principles known about the factors influencing the head losses in terms of added skin friction, wake friction and the magnitude of flow. It is seen from the graph that the loss coefficient decreases with the increasing Reynolds number as expected relative to the dominance, turbulence loss has over skin friction.

The correction factor found from the experiments is presented in Table 5.4 to demonstrate its variance in terms of the spacer length and the curvature ratios of the bends in the same plane. This data was computed from the manipulated equation that Miller used, Eq. 5.6m. Thus, has been used to express the correction factor for experiments conducted in this study. The trend lines in Fig. 5.4 should be linear but have steps which simply indicate experiments errors that were anticipated.

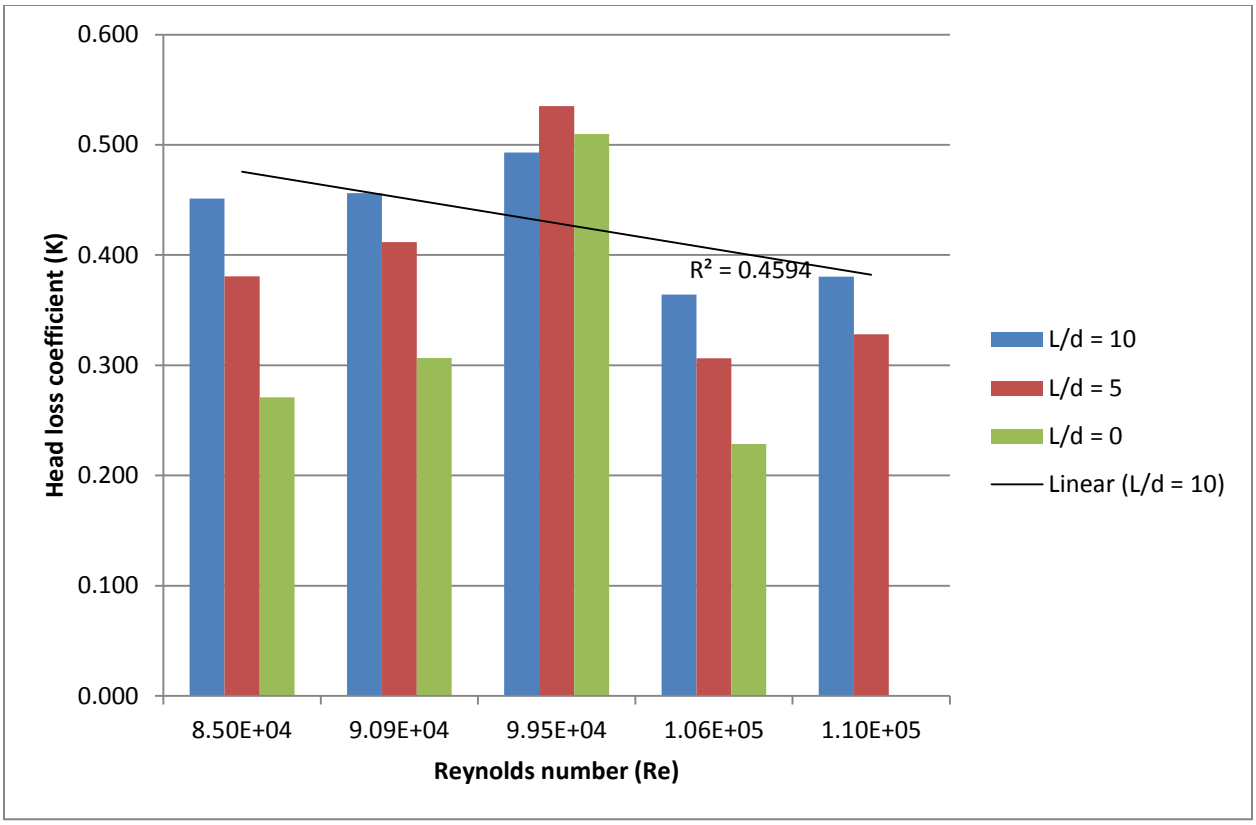

Figure 5.4a: Loss coefficient per spacer for a bend with a curvature ratio of, $r_c/d = 3$

Table 5.3: Loss coefficient of a single bend, Ito

2r/d	θ	α	Re	r_c/d	Ito, k
6	90	1.463	8.36E+04	3	0.208
6	90	1.463	8.40E+04	3	0.208
6	90	1.463	8.45E+04	3	0.208
6	90	1.463	8.54E+04	3	0.207
6	90	1.463	8.58E+04	3	0.207
6	90	1.463	8.61E+04	3	0.207
6	90	1.463	8.71E+04	3	0.207
6	90	1.463	9.26E+04	3	0.205
6	90	1.463	9.28E+04	3	0.205
6	90	1.463	9.84E+04	3	0.202
6	90	1.463	9.93E+04	3	0.202
6	90	1.463	1.00E+05	3	0.202

Table 5.4: Correction factor for closely spaced pipe bends

C1-2	L/d	Re
1.075	10	8.50E+04
1.086	10	9.09E+04

1.174	10	9.95E+04
0.867	10	1.06E+05
0.906	10	1.10E+05
0.906	5	8.50E+04
0.980	5	9.09E+04
1.274	5	9.95E+04
0.729	5	1.06E+05
0.781	5	1.10E+05
0.645	0	9.09E+04
0.730	0	9.95E+04
1.214	0	1.06E+05
0.544	0	1.10E+05

CHAPTER 6

CONCLUSIONS AND RECOMMENDATIONS

6.1 CFD summary

It is found that the loss coefficient of closely spaced pipe bends in principle shares a linear relationship with the length between the bends (spacer). However, the loss coefficient of closely spaced pipe bends is dependent on the spacer ratio (length between the bends over the inside diameter), turbulent flow (high Reynolds numbers) and the curvature ratio. The following has been found.

- The head loss increases with the spacer length.
- The correlation for calculating the head loss coefficient of closely spaced pipe bends for smooth pipe is:

$$\therefore k' = 4.8 \frac{{L}/{d}^{0.06} \, {r}/{d}^{0.07}}{Re^{0.21}}$$

Valid for:

$$\mathbf{1 \leq {L}/{d} \leq 10;\ \ 7.3x10^4 \leq Re \leq 5.84x10^5\ ;3 \leq {r_c}/{d} \leq 5}$$

Table 6.1: Deviation of experimental results from CFD results

L/d	Exp-K (Re = 9.09e4)	CFD-k' (Re = 7.3e4)	error
10	0.456	0.598	-24%
5	0.412	0.558	-26%
1	-	0.519	-
0	0.271	-	-

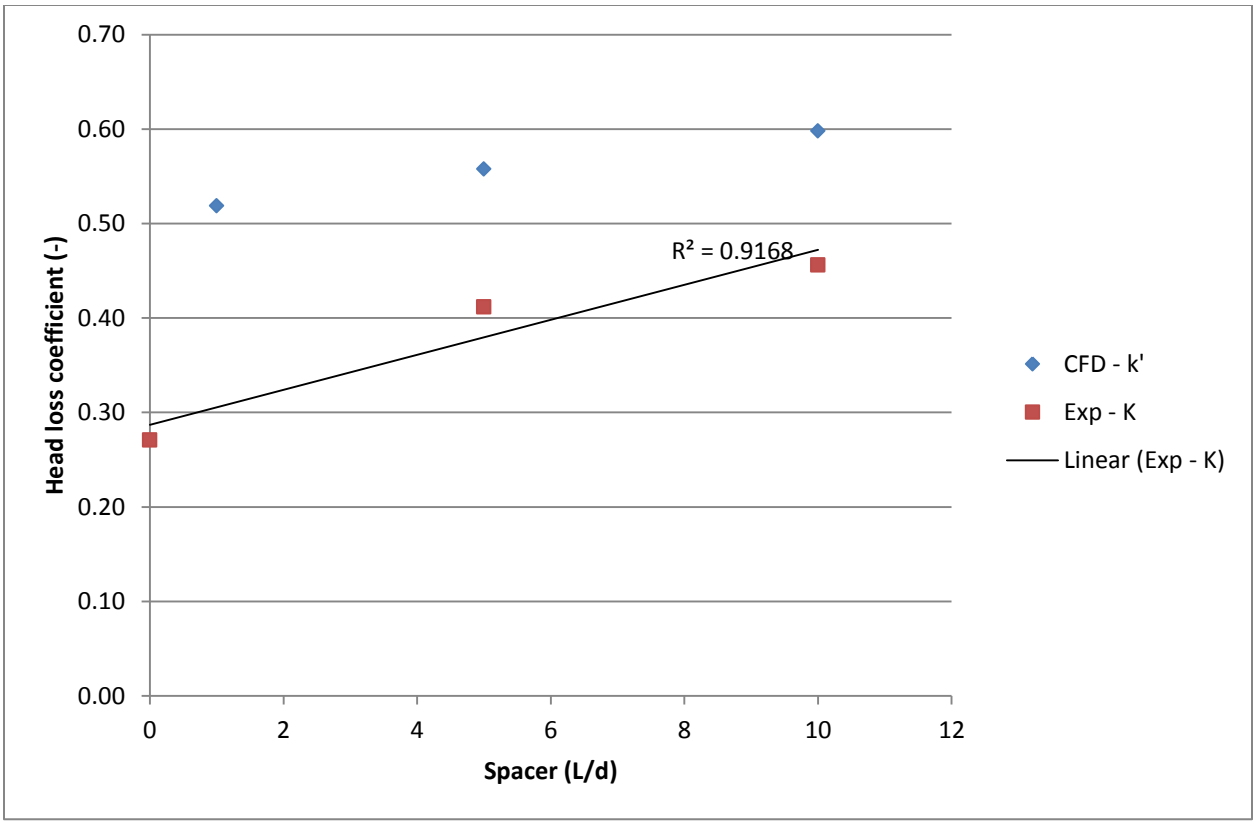

Figure 6.1: Comparison of the CFD results and experiments at Re = 9.09×10^4 and Re = 7.3×10^4 respectively

6.2 Recommendation for future work

This work indicates potential for useful additional analysis and experimentation:

- Numerical modelling of Newtonian fluids (in the laminar and turbulent regimes) for smooth bends at 0^0 and 90^0 mutual planes.
- Numerical modelling of closely spaced combinations of:
  - 90^0 bends and other pipe fittings, viz. ball valve, gate valve, diaphragm valve, tee, wye, etc.
- Developing sets of empirical correlations and tables for most fluid flow conditions and component (minor losses) combinations.

REFERENCES

Anagnson, J.T., Deleon, R. E. 2007. StataQuest 4. California: Duxbury Press: 238-240.

Anderson, J.D. 2005. Ludwig Prandtl's boundary layer. American Institute of Physics. 47, December,
http://wwww.physicstoday.org
[16 February 2009].

Anon. 2008. Best practice guide for marine: Applications of Computational Fluid Dynamics. WS Atkins Consultants. 9.

ANSYS, 2006. Innovative turbulence modelling: SST model in ANSYS® CFX® 11.
http://www.ansys.com/assets/tech-briefs/cfx-sst.pdf
[8 March 2010].

Arada, N., Pires, M. & Sequeira, A. 2006. Viscosity effects on flows of generalized Newtonian fluids through curved pipes. Computers and Mathematics with Applications. 53 (2007): 626, February, 27.

Brodkey, R.S. 1967. The phenomena of fluid motions. 1st ed. Massachusetts: Addison-Wesley, 138-139.

Cebeci, T., Shao, J.P. Kafyeke. F. & Laurendean, E. 2005. Computational Fluid Dynamics for engineers. 1st ed. California: Horizons Publishing. 55.

Chan, W.M., Gomez, R.S., Rogers, S.E. & Bunning, P.G. 2002. Best practices in overset grid generation. American Institute of Aeronautics and Astronautics. 99(0157): 2002-3191, January, 11.

Cherrye, E.M., Elkins, C.J. & Eaton, J.K. 2008. Geometric sensitivity of three-dimensional separated flows. Journal of Heat and Fluid flow. 2008.01.018. 1-9. January, 24.

Coffield, R.D.,McKeown, P.T. & Hammond, R.B. 1997. Irrecoverable pressure loss coefficients for two elbows in series with various orientation angles and separation distances. Betis Atomic Power Laboratory: 1-19, April, 24.

Coleman.H W. & Steele.W.G, 2009. Experimentation, validation and uncertainty analysis for engineers. 3rd ed. Hobeken: John Wiley & Sons, 4-5, 14.

Crowe, C.T., Elger, D.F. & Roberson, J.A. 2005. Engineering fluid mechanics. 8th ed. Hoboken: John Wiley & Sons Inc., 14-15, 391.

Daugherty, R. & Franzini, J. 1977. Fluid mechanics with engineering applications, Kogakusha: McGraw-Hill: 228.

Davidson, L. 2003. An introduction to turbulence models. Chalmers University of Technology, Department of Thermo and Fluid dynamics. 97(2):5. http://www.tfd.cahlmers.se/~lada, November 2003.

Dey, S. 2001. Secondary boundary layer and wall shear for fully developed flows in curved pipes. The Royal Society, 283, December 19.

Douglas, J.F., Gasiorek, J.M. & Swaffield J.A. 1995. Fluid mechanics. 2nd ed. New York: John Wiley & Sons Inc., 90, 312.

ESDU CFD-BMK 07009, CFD Benchmarks for predicting pressure loss and flow characteristics Incompressible flow in sudden contractions, IHS ESDU, London, 2006:7.

Flowmaster, 2010. Internal flow systems.
http://www.flowmaster.com/flowmaster-dismiller.html
[31 March 2010].

Gan, G. & Riffat, S. 1996. Measurement and Computational Fluid Dynamics predictions of diffuser pressure loss coefficient. Applied Energy: 54(2):181-195.

Ito, H. 1987. Flow in curved pipes. JSME International Journal. 262(30):548, December 26.

Iudicello, F. 2008. Introduction to computational fluid dynamics and application to internal flow problems. London :IHS-ESDU.

Jawarneh, A.M. & Vatistas, G.H. 2006. Reynolds stress model in the prediction of confined turbulent swirling flows. Journal of Fluids Engineering, 128(1), 1377-1382, March, 22.

Jianfu, Z. & Gabriel, K.S. 2004. Two-phase flow patterns in a 90^0 bend in microgravity. The Chinese Society of Theoretical and Applied Mechanics. 20(3): 207, June.

Kandlikar, S.G, 2005. Roughness effects at mircoscale-reassessing Nikuradse's experiments on liquid flow in rough tubes. Bulletin of the Polish academy of science, 53(4) 343.

Lasher, W.C. & Sonnenmeier, J.R. 2007. An analysis of practical RANS simulations for spinnaker aerodynamics. Journal of Wind Engineering and Industrial Aerodynamics. 96(2008): 149, March, 18.

Levchenya, A.M. & Smirnov, E.M. 2007. CFD-Analysis of 3D flow structure and end wall heat transfer in a transonic turbine blade cascade: Effects of grid refinement. Proceedings of the WEHSFF, West East High Speed Flow Field, Moscow, 19-22 November 2007, 1-2.

Liu, S. Afaican, A., Nasr-El-Din, H.A. & Masliyah, J. 1994. An experimental study of pressure drop in helical pipes. Mathematical and Physical Sciences, 444(1921): 307, February, 8.

Maharudrayya, S., Jayanti, S. & Deshpande, A.P. 2004. Pressure losses in laminar flow through serpentine channels in fuel cell stacks. Journal of Power Sources 138(2004): 1-13, July, 31.

Marn, J. & Primoz, T. 2006. Laminar flow of a shear-thickening fluid. Fluid Dynamics Research. 28(2006): 295-312, January, 25.

McMahon, N. 2003. Derivation of boundary layer equations two-dimensional flow. School of Computer Applications, Dublin City University. 1-4, January, 4.

Menter, F.R. 1994. Eddy viscosity transport equations and their relation to the k-ε model. NASA Technical Memorandum.2, November.

Merzkirich, W., von Lavante, E., Gersten, K. & Hans, V. 2005. Fluid mechanics of flow metering. 1st ed. Berlin: Springer., 14.

Miller, D. S. 1990. Internal flow systems, Bedford: BHRA fluid engineering, 80-228.

Modi, P.P. & Jayanti S., 2004. Pressure losses and flow distribution in ducts with sharp bends. Trans IChemE 82, 82(A3):321-331, March.

Moody. L.F. & Princeton N.J. 1944. Friction factors for pipe flow. Transaction for A.S.M.E, 66(1): 672, November

Mukhtar, A., Singh, S.N. & Seshadri, V. 1994. Pressure drop in long radius 90^0 horizontal bend for the flow of multisized heterogeneous slurries. International Journal of Multiphase Flow:21(2): 330.

Ouazzaane, A.K. & Benhadji, R. 2004. Flow conditioners design and their effects in reducing flow metering errors. Sensor Review: 22(3): 2244.

Papageorgakis, G.C. & Assanis, D. N. 1999. Comparison of linear and nonlinear RNG-based k-ε models for incompressible turbulent flows. Numerical Heat Transfer. Part B (35): 1.

Papworth, M. & Miller, D.S. 1974. Close coupled 90^0 bend and diffuser combinations for pipes. BHRA fluid engineering, 27, November, 27.

Pienaar, V.G., Alderman, N.J. & Heywood, N.I. 2001. Slurry Handling: A review of frictional pressure losses for flow of Non-Newtonian fluids through pipe fittings. SH: 2(6): 4, 22, September.

Ploychay, Y., Eiamsa, S. & Sripattanapipat, S. 2004. Numerical investigation of turbulent channel flow with inclined injection. Proceeding of the 18th National Mechanical Engineering Conference, KonKaen, 18-20 October, 6.

Raven, W.B., Lin, B., Falconer, R.A. & Teixeira, E.C. 2007. CFD and experimental model studies for water disinfection tanks with low Reynolds number flows, Chemical Engineering Journal, 558.

Rigas, F. & Sklavounos, S. 2007. Computer simulations in consequence analysis and loss preventions. National Technical University of Athens school of Chemical Engineering. 171.

Roache, P.T. 1998. Verification and validation in computational science and engineering. Socorro: Hermosa Publishers

Rumsey, C.L., Gatski, T.B. & Morrison, S.M. 1999. Turbulence model predictions of extra-strain rate effects in strongly-curved flows. American Institute of Aeronautics and Astronautics. 99(157): 2, January, 11.

Sayers, A.T. 1992. Fluid mechanics.1st ed. Cape Town: Oxford University press, 282-300.

Sekavčnik, M., Ogerevc, T. & Škerget, L. 2006. CFD analysis of the dynamic behaviour of a pipe system. Forsch Ingenieurwes. 70:139-144. May, 17

Siriboonluckul, N., Juntasaro, E. & Juntasaro, V. 2005. Application of k-SST turbulence model for separated particle-laden flows. Proceedings of the 19th Conference of Mechanical Engineering Network of Thailand, Phuket, 19-21 October 2005, 4-6.

Sodja, J. 2007. Turbulence models in CFD. University of Ljubjana, Faculty of mathematics nad physics, Department of physics, 5-11, March.

Suga, K. 1998. Recent development in Eddy Viscosity Modelling of turbulence. R&D Review of Toyota CRDL. 33 (1): 4.

Tilton, J.N. 1999. Fluid and particle dynamics. American Institute of Chemical Engineers, 5.

Tony, W., Shen, H. & Tsai, S.F. 2006. Vortical flow topology in a curved duct with 90^0 bend. Proceedings of the 4th WSEAS International Conference on Fluid Mechanics and Aerodynamics, Elounda, 21-23 August 2006.Taipei: National Taiwan University: 121-129 .

Tryggeson, H. 2007. Analytical vortex solution to the Navier-Stokes equation. Ph. D thesis. Växjö University. Göteborg. 1.

Turian, R.M, Ma, T.W, Hsus, L.G. & Sung, M.D.J. 1997. Flow of concentrated non-Newtonian slurries: 2. Friction losses in bends, fittings, valves and venture meters. Int. J. Multiphase Flow, 24(2):243-269, May 15.

Versteeg, H.K. & Malalasekera, W. 1995. An introduction to Computational Fluid dynamics: The Finite Volume Method, Essex: Longman Scientific & Technical, 70.

White, C.M. 1929. Streamline flow through curved pipes. Royal Society. 123(792): 661, April, 6.

White, F.M. 2008. Fluid mechanics. 6th ed. New York: McGraw-Hill, 46-47.

Wu, H.L., Peng, P., Ye., Y. & Gong, .E. 2006. Simulation of refrigerant flow boiling in serpentine tubes. Journal of Heat and Mass transfer 50(2007): 1192, December, 5.

Zamora, B., Kaiser, A. S. & Viedma, A. 2006. On the effects of Reyleigh number and inlet turbulence intensity upon the buoyancy-induced mass flow rate in sloping and convergent channels. International Journal of Heat and Mass Transfer. 9 (2008): 2-4, August, 21.

APPENDIX A

COMPUTATIONAL FLUID DYNAMICS RESULTS: CLOSELY SPACED PIPE BENDS

A1 Correlation for the loss coefficient of closely spaced pipe bends

The investigation of the head loss coefficient of closely spaced pipe bends required an investigation of factors that influence its existence. Hence, the intention for performing a dimensional analysis was to establish a mathematical model that will calculate the loss coefficient of closely spaced pipe bends. The Buckingham's pi-theorem was used in the dimensional analysis of the system. It produced dimensional groups that led to the formulation of an empirical correlation of this study.

$$k = fn(v, d, r, L, P, \mu, \rho)$$

Number of fundamental dimensions = 3

Number of variables = 7

Number of dimensionless groups = 7-3 = 4

Table A1: Variables affecting the loss coefficient

Variable (Independent)	Symbol	Dimensions (MLT)
Water velocity inside the pipe	*v*	LT^{-1}
Inside diameter of the pipe	*d*	L
Radius of curvature of the bend	*r*	L
Pipe length between bends (Spacer length)	*L*	L
Absolute pressure inside the pipe	*P*	$ML^{-1}T^{-2}$
Viscosity of the liquid	μ	$ML^{-1}T^{-1}$

Density of the liquid	ρ	ML^{-3}

$$k = fn\left[\left(\frac{v}{\{LT^{-1}\}}\right),\left(\frac{d}{\{L\}}\right),\left(\frac{r}{\{L\}}\right),\left(\frac{L}{\{L\}}\right)\left(\frac{P}{\{ML^{-1}T^{-2}\}}\right),\left(\frac{\mu}{\{ML^{-1}T^{-1}\}}\right),\left(\frac{\rho}{\{ML^{-3}\}}\right)\right]$$
$$= fn\left[\left(\frac{r}{d}\right);\left(\frac{p}{\rho v^2}\right);\left(\frac{\rho v d}{\mu}\right);\left(\frac{L}{d}\right)\right]$$

The found pi-groups represent the following:

- Curvature ratio, $\frac{r}{d}$
- Loss coefficient, $\frac{p}{\rho v^2}$
- Reynolds number, $\frac{\rho v d}{\mu}$
- Spacing ratio, $\frac{L}{d}$

A2 Statistical method for a formulation an empirical correlation for smooth pipe bends: MS Excel

The interpretation of the regression output in Table. A2 is explained as follows (Anagnoson *et al,* 1997:238-240):

- **Source**, total sum of squares (TSS) where it is the sum of the model (explained sum of squares, ESS) and the residual (residual sum of squares, RSS). The SS, df and MS denotes the sum of the squares, denotes degrees of freedom and mean sum of squares.
- **The number of observations** explains the amount of the data used.
- **F-statistic** at degrees of freedom is a quotient of the Model MS divided by the Residual MS. It is used to measure the null hypothesis that all slopes equal to zero.

- **Significance F** it means there is less than one chance in ten thousand that an F-statistic as large or larger.
- **R Square** as a ratio of ESS to TSS (called the coefficient of determination), it is used a measure of a measure the goodness-of-fit of the regression model.
- **Adjusted R Square** discounts small improvements on variance of new variables thenit decreases the R Square value as more variables are added.
- **Coefficients** are the constants in the regression equation.

A statistical analysis of the of the head loss coefficient after ninety observations is presented in Table A 2. The independent variables in consideration are as follows:

X Variable 1 = Spacer ratio (L/d)
X Variable 2 = Reynolds number (Re)
X Variable 3 = curvature ratio (r/d)

Table A2: The Multiple regression statistical representation

SUMMARY OUTPUT

Regression Statistics	
Multiple R	0.994164263
R Square	0.988362581
Adjusted R Square	0.987956625
Standard Error	0.00896921
Observations	90

ANOVA

	df	*SS*	*MS*	*F*	*Significance F*
Regression	3	0.587579231	0.195859744	2434.651646	5.03849E-83
Residual	86	0.006918418	8.04467E-05		
Total	89	0.594497649			

	Coefficients	*Standard Error*	*t Stat*	*P-value*	*Lower 95%*	*Upper 95%*	*Lower 95%*	*Upper 95%*
Intercept	0.684069177	0.014940645	45.78578617	3.56239E-62	0.654368158	0.713770196	0.654368158	0.713770196
X Variable 1	0.057934483	0.003130468	18.50665365	9.78488E-32	0.051711319	0.064157647	0.051711319	0.064157647
X Variable 2	-0.207527646	0.002495616	-83.15687733	5.98997E-84	-0.212488767	-0.202566525	-0.212488767	-0.202566525
X Variable 3	0.070912526	0.010411163	6.81120125	1.24661E-09	0.050215819	0.091609233	0.050215819	0.091609233

Table A3: CFD data of the loss coefficient

k'	k	L/d	Re	r/d	Error % (k' v.s k)
0.570	0.598	10	7.3E+04	3	-4.660
0.567	0.590	9	7.3E+04	3	-3.961
0.563	0.583	8	7.3E+04	3	-3.445
0.558	0.575	7	7.3E+04	3	-2.960
0.553	0.567	6	7.3E+04	3	-2.483
0.547	0.558	5	7.3E+04	3	-1.920
0.540	0.547	4	7.3E+04	3	-1.358
0.530	0.539	3	7.3E+04	3	-1.539
0.518	0.529	2	7.3E+04	3	-2.112
0.497	0.519	1	7.3E+04	3	-4.251
0.419	0.434	10	3.2E+05	3	-3.441
0.417	0.428	9	3.2E+05	3	-2.650
0.414	0.422	8	3.2E+05	3	-2.036
0.410	0.417	7	3.2E+05	3	-1.496
0.407	0.410	6	3.2E+05	3	-0.895
0.402	0.403	5	3.2E+05	3	-0.254
0.397	0.395	4	3.2E+05	3	0.479
0.390	0.389	3	3.2E+05	3	0.172
0.381	0.381	2	3.2E+05	3	-0.201
0.365	0.374	1	3.2E+05	3	-2.278
0.368	0.395	10	5.8E+05	3	-6.730
0.366	0.390	9	5.8E+05	3	-6.093
0.364	0.386	8	5.8E+05	3	-5.789
0.361	0.382	7	5.8E+05	3	-5.517
0.357	0.376	6	5.8E+05	3	-4.991
0.353	0.369	5	5.8E+05	3	-4.321
0.349	0.360	4	5.8E+05	3	-3.098
0.343	0.354	3	5.8E+05	3	-3.230
0.335	0.349	2	5.8E+05	3	-4.128
0.321	0.342	1	5.8E+05	3	-6.095
0.582	0.606	10	7.3E+04	4	-3.992
0.578	0.598	9	7.3E+04	4	-3.320
0.574	0.591	8	7.3E+04	4	-2.869
0.570	0.584	7	7.3E+04	4	-2.475
0.564	0.577	6	7.3E+04	4	-2.186
0.558	0.565	5	7.3E+04	4	-1.298
0.551	0.559	4	7.3E+04	4	-1.487
0.541	0.551	3	7.3E+04	4	-1.690
0.528	0.544	2	7.3E+04	4	-2.915
0.507	0.535	1	7.3E+04	4	-5.337
0.428	0.434	10	3.2E+05	4	-1.491
0.425	0.433	9	3.2E+05	4	-1.766
0.422	0.423	8	3.2E+05	4	-0.182

0.419	0.420	7	3.2E+05	4	-0.405
0.415	0.413	6	3.2E+05	4	0.558
0.410	0.404	5	3.2E+05	4	1.636
0.405	0.398	4	3.2E+05	4	1.591
0.398	0.392	3	3.2E+05	4	1.409
0.388	0.392	2	3.2E+05	4	-1.050
0.373	0.381	1	3.2E+05	4	-2.297
0.376	0.396	10	5.8E+05	4	-4.972
0.374	0.390	9	5.8E+05	4	-4.274
0.371	0.386	8	5.8E+05	4	-3.901
0.368	0.387	7	5.8E+05	4	-4.870
0.365	0.378	6	5.8E+05	4	-3.653
0.361	0.370	5	5.8E+05	4	-2.554
0.356	0.364	4	5.8E+05	4	-2.160
0.350	0.358	3	5.8E+05	4	-2.408
0.341	0.360	2	5.8E+05	4	-5.142
0.327	0.349	1	5.8E+05	4	-6.135
0.591	0.620	10	7.3E+04	5	-4.615
0.587	0.613	9	7.3E+04	5	-4.139
0.583	0.606	8	7.3E+04	5	-3.784
0.578	0.599	7	7.3E+04	5	-3.416
0.573	0.591	6	7.3E+04	5	-3.068
0.567	0.584	5	7.3E+04	5	-2.852
0.559	0.575	4	7.3E+04	5	-2.638
0.550	0.567	3	7.3E+04	5	-3.042
0.537	0.561	2	7.3E+04	5	-4.419
0.515	0.552	1	7.3E+04	5	-6.772
0.434	0.448	10	3.2E+05	5	-3.021
0.432	0.438	9	3.2E+05	5	-1.437
0.429	0.433	8	3.2E+05	5	-1.049
0.425	0.428	7	3.2E+05	5	-0.647
0.421	0.422	6	3.2E+05	5	-0.186
0.417	0.416	5	3.2E+05	5	0.145
0.411	0.409	4	3.2E+05	5	0.537
0.404	0.408	3	3.2E+05	5	-0.872
0.394	0.400	2	3.2E+05	5	-1.315
0.378	0.393	1	3.2E+05	5	-3.604
0.382	0.403	10	5.8E+05	5	-5.264
0.379	0.399	9	5.8E+05	5	-4.811
0.377	0.392	8	5.8E+05	5	-3.803
0.374	0.391	7	5.8E+05	5	-4.510
0.370	0.386	6	5.8E+05	5	-4.025
0.366	0.380	5	5.8E+05	5	-3.661
0.361	0.372	4	5.8E+05	5	-2.923
0.355	0.367	3	5.8E+05	5	-3.318
0.347	0.365	2	5.8E+05	5	-5.093
0.333	0.358	1	5.8E+05	5	-7.039

APPENDIX B

EXPERIMENTAL RESULTS: Friction factor

Table B1: experimental data of the friction factor

Parameters			v (10D)	Re (10D)	LHS	RHS	RHS/LHS	*f*	*f (10D)*	Blasius (smooth pipes)	*Error %*
					Goal Seek method				*worksheet Iteration*	Re (10D)	
Pipe roughness (m)	0.00002	*e*	1.8500	8.41E+04	7.045194	7.047365	1.000308	0.020147	0.02014	0.01856	8.496413438
Pipe Diameter (m)	0.0455	*D*	1.8600	8.45E+04	7.047937	7.050415	1.000352	0.020131	0.02012	0.01853	8.549499609
Viscosity (Pa s)	0.001	*mu*	1.8500	8.41E+04	7.044945	7.047386	1.000347	0.020149	0.02014	0.01856	8.49641729
Density (kg m^{-3})	998	*rho*	1.8700	8.50E+04	7.050909	7.053423	1.000357	0.020115	0.02010	0.01851	8.602485484
Relative roughness	0.000	*e/D*	1.8600	8.45E+04	7.047937	7.050415	1.000352	0.020131	0.02012	0.01853	8.549499609
			1.8700	8.50E+04	7.050909	7.053423	1.000357	0.020115	0.02010	0.01851	8.602485484
			1.8400	8.36E+04	7.041932	7.044337	1.000342	0.020166	0.02015	0.01858	8.443238119
			1.8600	8.45E+04	7.047937	7.050415	1.000352	0.020131	0.02012	0.01853	8.549499609
			1.8600	8.45E+04	7.047937	7.050415	1.000352	0.020131	0.02012	0.01853	8.549499609
			1.8500	8.41E+04	7.044945	7.047386	1.000347	0.020149	0.02014	0.01856	8.49641729
			1.8500	8.41E+04	7.044945	7.047386	1.000347	0.020149	0.02014	0.01856	8.49641729
			1.8500	8.41E+04	7.044945	7.047386	1.000347	0.020149	0.02014	0.01856	8.49641729
			1.8500	8.41E+04	7.044945	7.047386	1.000347	0.020149	0.02014	0.01856	8.49641729
			1.8500	8.41E+04	7.044945	7.047386	1.000347	0.020149	0.02014	0.01856	8.49641729
			1.8400	8.36E+04	7.041932	7.044337	1.000342	0.020166	0.02015	0.01858	8.443238119
			1.8400	8.36E+04	7.041932	7.044337	1.000342	0.020166	0.02015	0.01858	8.443238119
			1.8500	8.41E+04	7.044945	7.047386	1.000347	0.020149	0.02014	0.01856	8.49641729

1.8500	8.41E+04	7.044945	7.047386	1.000347	0.020149	0.02014	0.01856	8.49641729
1.8400	8.36E+04	7.041932	7.044337	1.000342	0.020166	0.02015	0.01858	8.443238119
1.8400	8.36E+04	7.041932	7.044337	1.000342	0.020166	0.02015	0.01858	8.443238119
1.8500	8.41E+04	7.044945	7.047386	1.000347	0.020149	0.02014	0.01856	8.49641729
1.8500	8.41E+04	7.044945	7.047386	1.000347	0.020149	0.02014	0.01856	8.49641729
1.8400	8.36E+04	7.041932	7.044337	1.000342	0.020166	0.02015	0.01858	8.443238119
1.8400	8.36E+04	7.041932	7.044337	1.000342	0.020166	0.02015	0.01858	8.443238119
1.8400	8.36E+04	7.041932	7.044337	1.000342	0.020166	0.02015	0.01858	8.443238119
1.8400	8.36E+04	7.041932	7.044337	1.000342	0.020166	0.02015	0.01858	8.443238119
1.8500	8.41E+04	7.044945	7.047386	1.000347	0.020149	0.02014	0.01856	8.49641729
1.8400	8.36E+04	7.041932	7.044337	1.000342	0.020166	0.02015	0.01858	8.443238119
1.8400	8.36E+04	7.041932	7.044337	1.000342	0.020166	0.02015	0.01858	8.443238119
1.8400	8.36E+04	7.041932	7.044337	1.000342	0.020166	0.02015	0.01858	8.443238119
1.8400	8.36E+04	7.041932	7.044337	1.000342	0.020166	0.02015	0.01858	8.443238119
1.8600	8.45E+04	7.047937	7.050415	1.000352	0.020131	0.02012	0.01853	8.549499609
1.8600	8.45E+04	7.047937	7.050415	1.000352	0.020131	0.02012	0.01853	8.549499609
1.8600	8.45E+04	7.047937	7.050415	1.000352	0.020131	0.02012	0.01853	8.549499609
1.8600	8.45E+04	7.047937	7.050415	1.000352	0.020131	0.02012	0.01853	8.549499609
1.8500	8.41E+04	7.044945	7.047386	1.000347	0.020149	0.02014	0.01856	8.49641729
1.8500	8.41E+04	7.044945	7.047386	1.000347	0.020149	0.02014	0.01856	8.49641729
1.8500	8.41E+04	7.044945	7.047386	1.000347	0.020149	0.02014	0.01856	8.49641729
1.8500	8.41E+04	7.044945	7.047386	1.000347	0.020149	0.02014	0.01856	8.49641729
1.8700	8.50E+04	7.050909	7.053423	1.000357	0.020115	0.02010	0.01851	8.602485484
1.8500	8.41E+04	7.044945	7.047386	1.000347	0.020149	0.02014	0.01856	8.49641729
1.8500	8.41E+04	7.044945	7.047386	1.000347	0.020149	0.02014	0.01856	8.49641729
1.8600	8.45E+04	7.047937	7.050415	1.000352	0.020131	0.02012	0.01853	8.549499609
1.8600	8.45E+04	7.047937	7.050415	1.000352	0.020131	0.02012	0.01853	8.549499609
1.8700	8.50E+04	7.050909	7.053423	1.000357	0.020115	0.02010	0.01851	8.602485484
1.8700	8.50E+04	7.050909	7.053423	1.000357	0.020115	0.02010	0.01851	8.602485484

1.8400	8.36E+04	7.041932	7.044337	1.000342	0.020166	0.02015	0.01858	8.443238119
1.8400	8.36E+04	7.041932	7.044337	1.000342	0.020166	0.02015	0.01858	8.443238119
1.8500	8.41E+04	7.044945	7.047386	1.000347	0.020149	0.02014	0.01856	8.49641729
1.8500	8.41E+04	7.044945	7.047386	1.000347	0.020149	0.02014	0.01856	8.49641729
1.8500	8.41E+04	7.044945	7.047386	1.000347	0.020149	0.02014	0.01856	8.49641729
1.8500	8.41E+04	7.044945	7.047386	1.000347	0.020149	0.02014	0.01856	8.49641729
1.8500	8.41E+04	7.044945	7.047386	1.000347	0.020149	0.02014	0.01856	8.49641729
1.8500	8.41E+04	7.044945	7.047386	1.000347	0.020149	0.02014	0.01856	8.49641729
1.8500	8.41E+04	7.044945	7.047386	1.000347	0.020149	0.02014	0.01856	8.49641729
1.8500	8.41E+04	7.044945	7.047386	1.000347	0.020149	0.02014	0.01856	8.49641729
1.8500	8.41E+04	7.044945	7.047386	1.000347	0.020149	0.02014	0.01856	8.49641729
1.8500	8.41E+04	7.044945	7.047386	1.000347	0.020149	0.02014	0.01856	8.49641729
1.8500	8.41E+04	7.044945	7.047386	1.000347	0.020149	0.02014	0.01856	8.49641729
1.8500	8.41E+04	7.044945	7.047386	1.000347	0.020149	0.02014	0.01856	8.49641729
1.8600	8.45E+04	7.047937	7.050415	1.000352	0.020131	0.02012	0.01853	8.549499609
1.8600	8.45E+04	7.047937	7.050415	1.000352	0.020131	0.02012	0.01853	8.549499609
1.8400	8.36E+04	7.041932	7.044337	1.000342	0.020166	0.02015	0.01858	8.443238119
1.8400	8.36E+04	7.041932	7.044337	1.000342	0.020166	0.02015	0.01858	8.443238119
1.8500	8.41E+04	7.044945	7.047386	1.000347	0.020149	0.02014	0.01856	8.49641729
1.8500	8.41E+04	7.044945	7.047386	1.000347	0.020149	0.02014	0.01856	8.49641729
1.8700	8.50E+04	7.050909	7.053423	1.000357	0.020115	0.02010	0.01851	8.602485484
1.8700	8.50E+04	7.050909	7.053423	1.000357	0.020115	0.02010	0.01851	8.602485484
1.8500	8.41E+04	7.044945	7.047386	1.000347	0.020149	0.02014	0.01856	8.49641729
1.8600	8.45E+04	7.047937	7.050415	1.000352	0.020131	0.02012	0.01853	8.549499609
1.8600	8.45E+04	7.047937	7.050415	1.000352	0.020131	0.02012	0.01853	8.549499609
1.8400	8.36E+04	7.041932	7.044337	1.000342	0.020166	0.02015	0.01858	8.443238119
1.8400	8.36E+04	7.041932	7.044337	1.000342	0.020166	0.02015	0.01858	8.443238119
1.8500	8.41E+04	7.044945	7.047386	1.000347	0.020149	0.02014	0.01856	8.49641729
1.8500	8.41E+04	7.044945	7.047386	1.000347	0.020149	0.02014	0.01856	8.49641729
1.8300	8.31E+04	7.038898	7.041268	1.000337	0.020183	0.02017	0.01861	8.389961688

1.8300	8.31E+04	7.038898	7.041268	1.000337	0.020183	0.02017	0.01861	8.389961688
1.8500	8.41E+04	7.044945	7.047386	1.000347	0.020149	0.02014	0.01856	8.49641729
1.8500	8.41E+04	7.044945	7.047386	1.000347	0.020149	0.02014	0.01856	8.49641729
1.8500	8.41E+04	7.044945	7.047386	1.000347	0.020149	0.02014	0.01856	8.49641729
1.8500	8.41E+04	7.044945	7.047386	1.000347	0.020149	0.02014	0.01856	8.49641729
1.8400	8.36E+04	7.041932	7.044337	1.000342	0.020166	0.02015	0.01858	8.443238119
1.8400	8.36E+04	7.041932	7.044337	1.000342	0.020166	0.02015	0.01858	8.443238119
1.8400	8.36E+04	7.041932	7.044337	1.000342	0.020166	0.02015	0.01858	8.443238119
1.8500	8.41E+04	7.044945	7.047386	1.000347	0.020149	0.02014	0.01856	8.49641729
1.8500	8.41E+04	7.044945	7.047386	1.000347	0.020149	0.02014	0.01856	8.49641729
1.8400	8.36E+04	7.041932	7.044337	1.000342	0.020166	0.02015	0.01858	8.443238119
1.8400	8.36E+04	7.041932	7.044337	1.000342	0.020166	0.02015	0.01858	8.443238119
1.8500	8.41E+04	7.044945	7.047386	1.000347	0.020149	0.02014	0.01856	8.49641729
1.8500	8.41E+04	7.044945	7.047386	1.000347	0.020149	0.02014	0.01856	8.49641729
1.8500	8.41E+04	7.044945	7.047386	1.000347	0.020149	0.02014	0.01856	8.49641729
1.8500	8.41E+04	7.044945	7.047386	1.000347	0.020149	0.02014	0.01856	8.49641729
1.8400	8.36E+04	7.041932	7.044337	1.000342	0.020166	0.02015	0.01858	8.443238119
1.8400	8.36E+04	7.041932	7.044337	1.000342	0.020166	0.02015	0.01858	8.443238119
1.8500	8.41E+04	7.044945	7.047386	1.000347	0.020149	0.02014	0.01856	8.49641729
1.8500	8.41E+04	7.044945	7.047386	1.000347	0.020149	0.02014	0.01856	8.49641729
1.8500	8.41E+04	7.044945	7.047386	1.000347	0.020149	0.02014	0.01856	8.49641729
1.8600	8.45E+04	7.047937	7.050415	1.000352	0.020131	0.02012	0.01853	8.549499609
1.8600	8.45E+04	7.047937	7.050415	1.000352	0.020131	0.02012	0.01853	8.549499609
1.8300	8.31E+04	7.038898	7.041268	1.000337	0.020183	0.02017	0.01861	8.389961688
1.8300	8.31E+04	7.038898	7.041268	1.000337	0.020183	0.02017	0.01861	8.389961688
1.8300	8.31E+04	7.038898	7.041268	1.000337	0.020183	0.02017	0.01861	8.389961688
1.8300	8.31E+04	7.038898	7.041268	1.000337	0.020183	0.02017	0.01861	8.389961688

APPENDIX C

EXPERIMENTAL RESULTS: CLOSELY SPACED PIPE BENDS

Table C1: Head loss coefficient of closely spaced pipe bends

d	ε	ρ	Lu	Lb	Lt	Ld
0.046 m	0.00002	998 m^3/kg	2.276 m	0.217 m	10.698 m	7.967 m

L/d = 10

Blasius	m^3/s	m/s	Re	P1 (bar)	P2 (bar)	P3 (bar)	*f* (Cole-Brooke)	D h1-3 (m)	D h2-3 (m)	*f* (Darcy)	L/d	K (head)	V^2/2g
0.0185	0.0153	1.8700	8.50E+04	15.8327	15.3448	15.2999	0.0180	0.5237	0.000458793	0.0141	10	0.451	0.1782
0.0182	0.0125	2.0000	9.09E+04	12.8834	12.5701	12.5379	0.0205	0.3396	0.000328543	0.0088	10	0.456	0.2039
0.0178	0.0090	2.1900	9.95E+04	9.5836	8.9959	8.9592	0.0205	0.6138	0.000374652	0.0084	10	0.493	0.2444
0.0175	0.0053	2.3300	1.06E+05	5.9888	5.3681	5.3111	0.0205	0.6662	0.000582436	0.0116	10	0.364	0.2767
0.0173	0.0034	2.4300	1.10E+05	4.0379	3.3299	3.3860	0.0205	0.6407	0.000573570	0.0105	10	0.380	0.3010

L/d = 5

Blasius	m^3/s	m/s	Re	P1 (bar)	P2 (bar)	P3 (bar)	*f* (Cole-Brooke)	D h1-3 (m)	D h2-3 (m)	*f* (Darcy)	L/d	K (head)	V^2/2g
0.019	0.015	1.870	8.50E+04	15.3540	14.866	14.821	0.0205	0.524	0.000458793	0.014	5	0.381	0.1782
0.018	0.013	2.000	9.09E+04	13.4715	13.158	13.126	0.0205	0.340	0.000328543	0.009	5	0.412	0.2039
0.018	0.009	2.190	9.95E+04	10.0155	9.428	9.391	0.0205	0.614	0.000374652	0.008	5	0.535	0.2444
0.018	0.006	2.330	1.06E+05	6.9810	6.360	6.303	0.0205	0.666	0.000582436	0.012	5	0.306	0.2767
0.017	0.004	2.430	1.10E+05	4.2400	3.644	3.588	0.0205	0.641	0.000573570	0.010	5	0.328	0.3010

L/d = 0

Blasius	m^3/s	m/s	Re	P1 (bar)	P2 (bar)	P3 (bar)	*f* (Cole-Brooke)	D h1-3 (m)	D h2-3 (m)	*f* (Darcy)	L/d	K (head)	V^2/2g
0.018	0.0135	2.000	9.09E+04	14.0790	13.501	13.546	0.0205	0.5237	0.000458793	0.0124	0	0.271	0.2039
0.018	0.0115	2.190	9.95E+04	11.8690	11.491	11.523	0.0205	0.3396	0.000328543	0.0074	0	0.307	0.2444
0.018	0.0073	2.330	1.06E+05	7.9460	7.285	7.322	0.0205	0.6138	0.000374652	0.0074	0	0.510	0.2767
0.017	0.0033	2.430	1.10E+05	3.9765	3.242	3.299	0.0205	0.6662	0.000582436	0.0106	0	0.228	0.3010

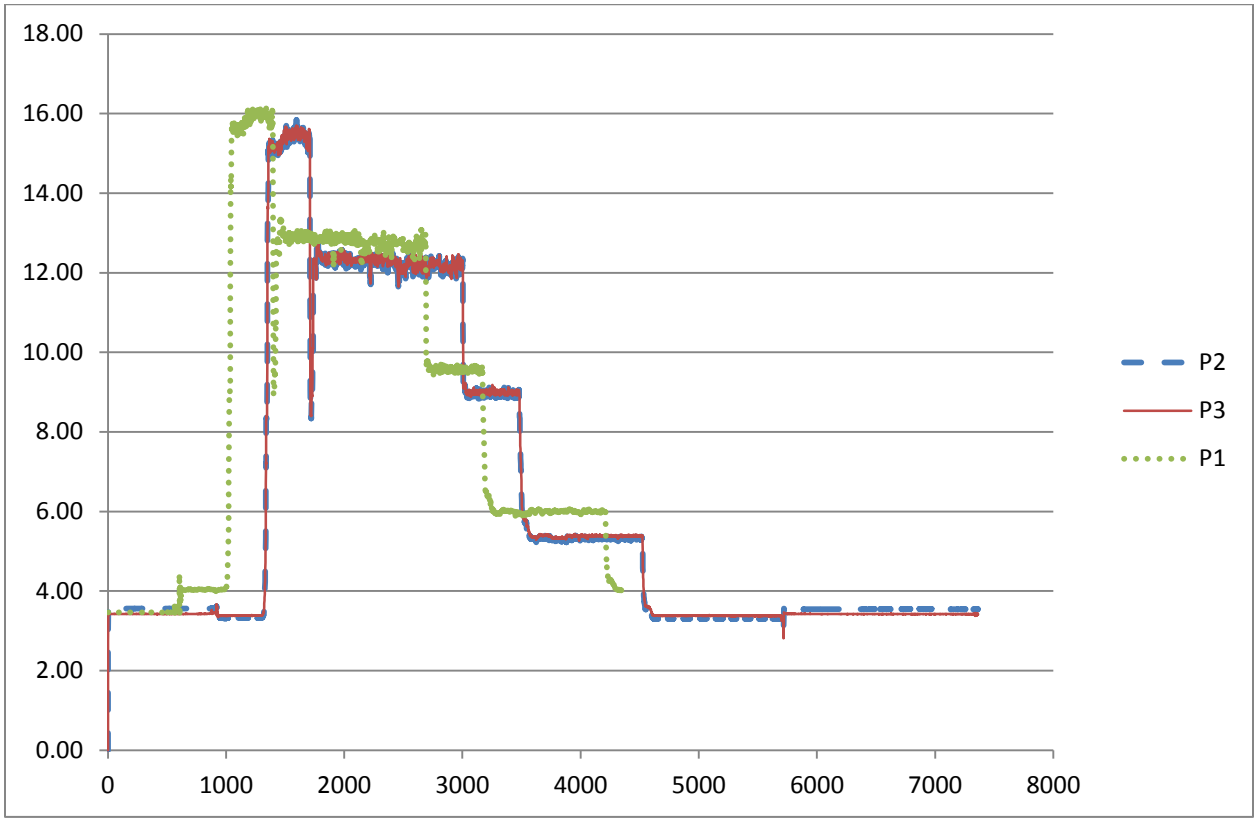

Figure C1: Pressure readings for the L/d = 10

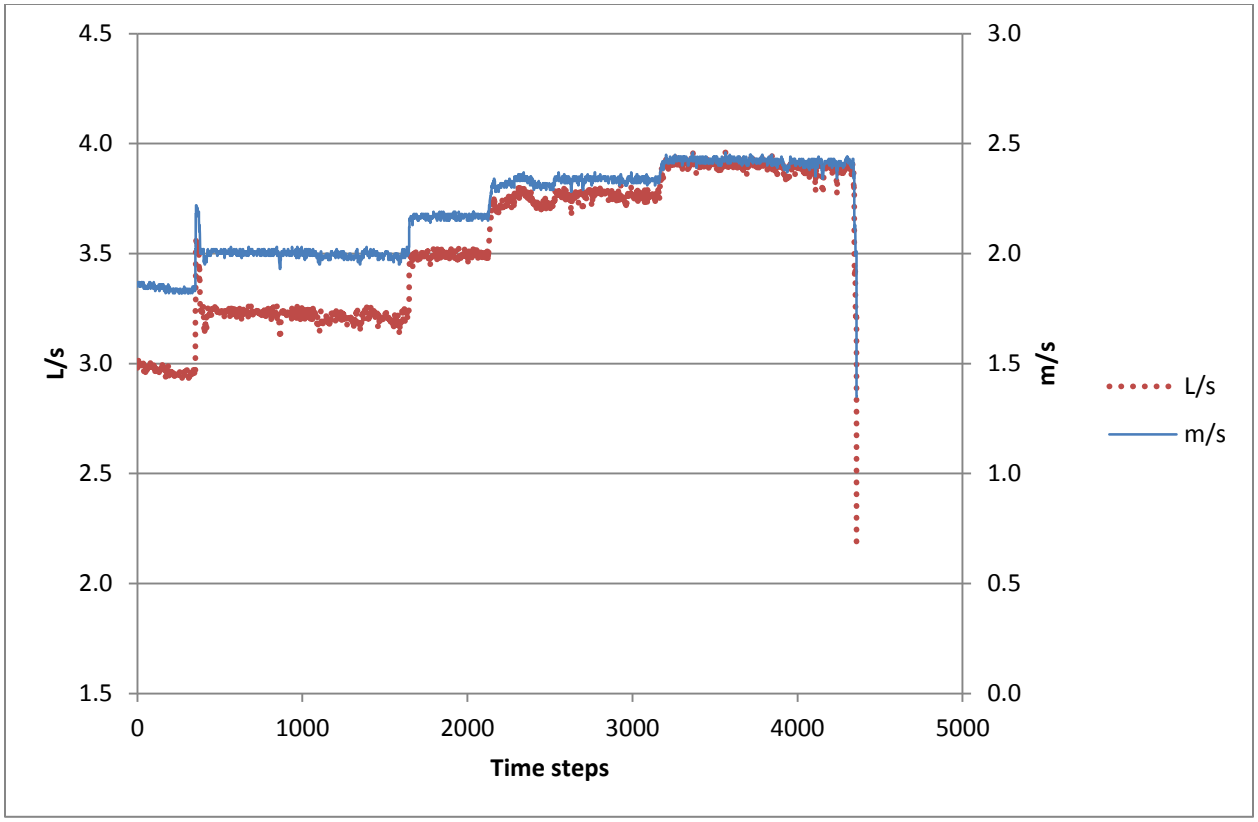

Figure C2: Fluid flow for L/d = 10

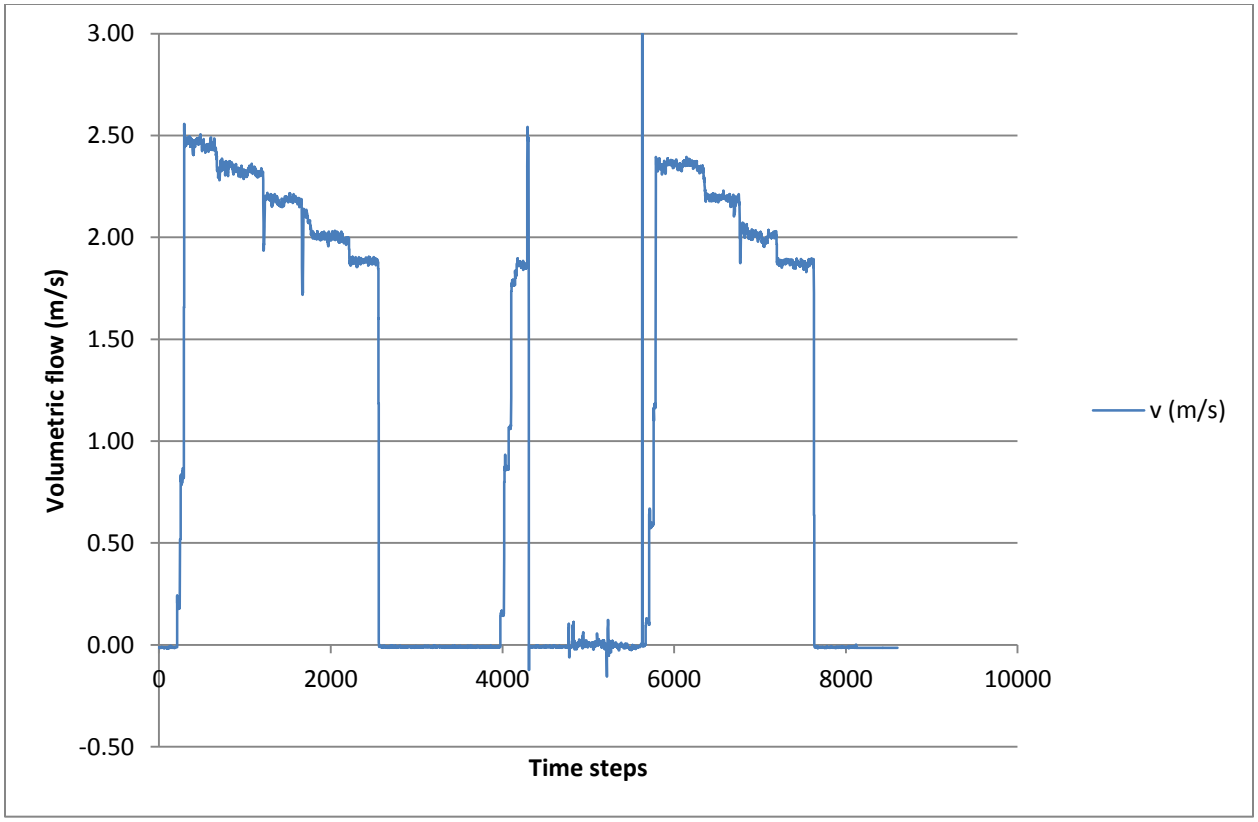

Figure C3: Fluid flow for L/d 5 and L/d 0

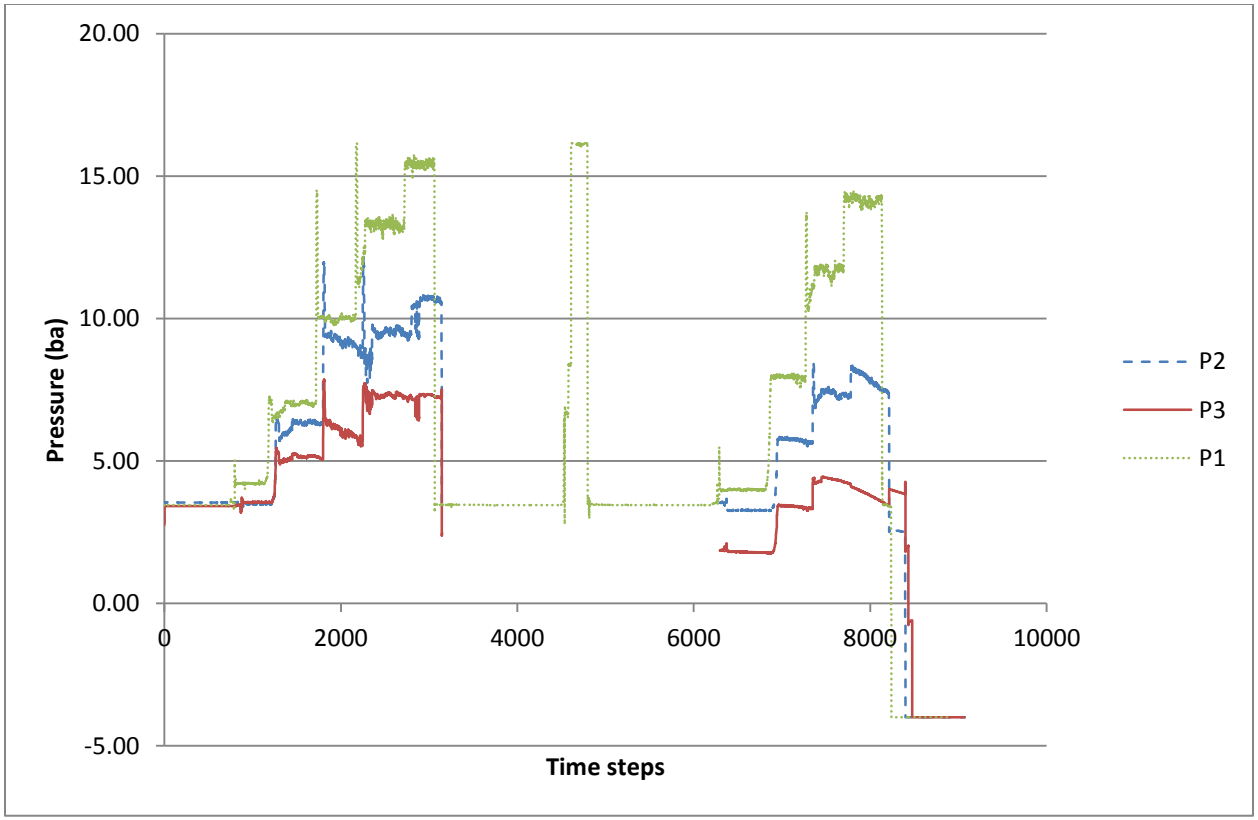

Figure C4: Pressure readings for L/d = 5 and L/d = 0

Figure C5: Connection to the municipal mains

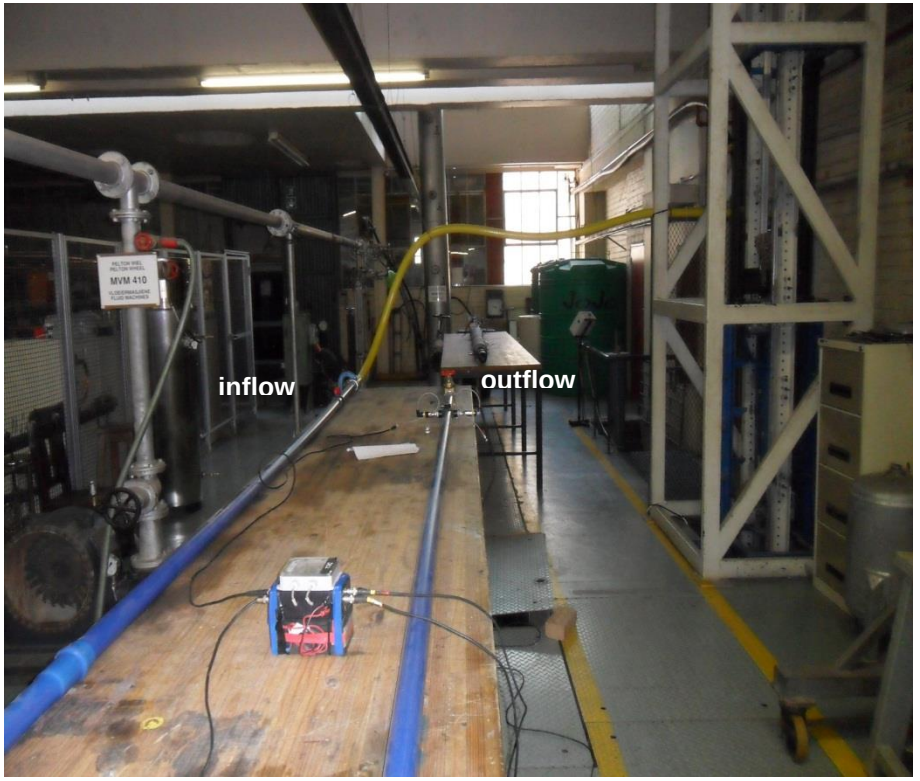

Figure C6: Overview of the rig indicating inlet and outlet

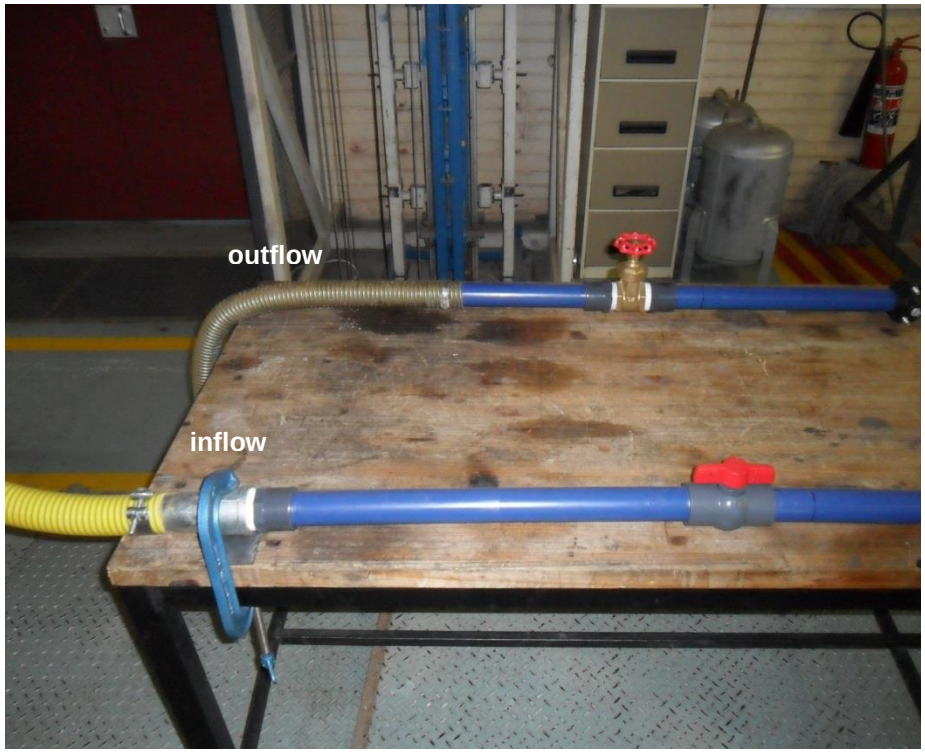

Figure C7: Ball valve upstream the bends and a gate (flow throttling) valve downstream

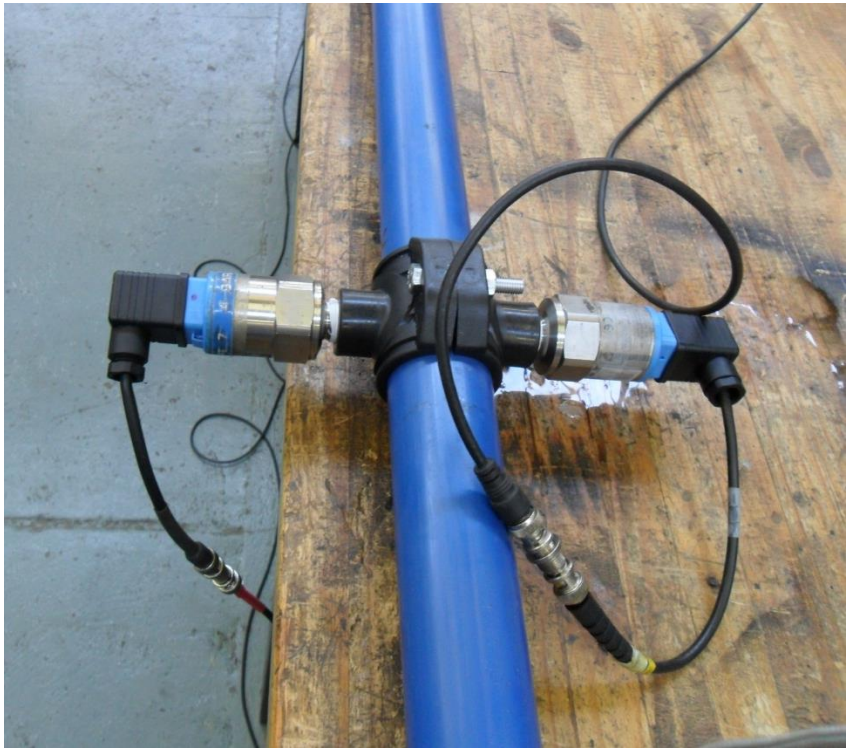

Figure C8: Two pressure transducers on a pressure point

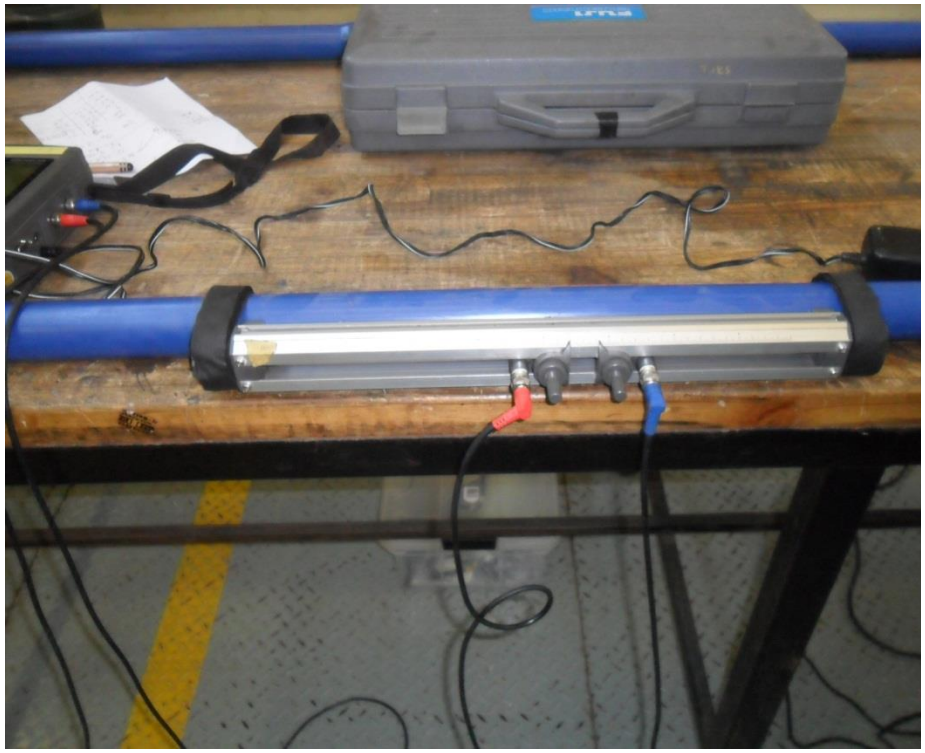

Figure C9: Ultrasonic flowmeter

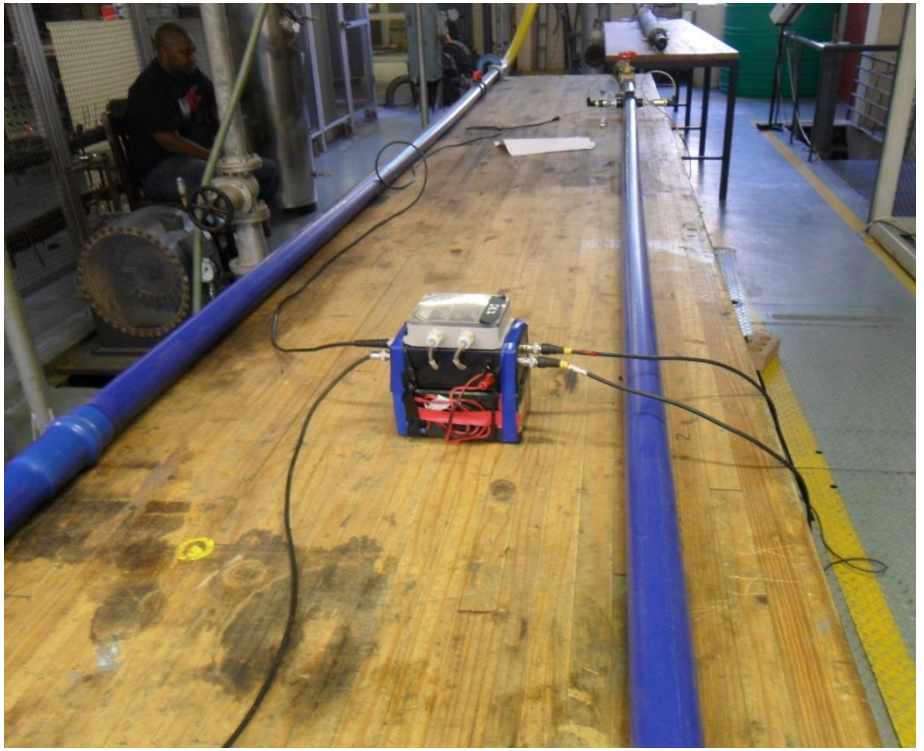

Figure C10: HOBO data logger